CHARACTERIZATION OF PVA-BORAX-FRUCTOSE GEL FOR THE CAPTURE OF RADIOACTIVE WASTES GENERATED DURING NUCLEAR DECOMMISSIONING ACTIVITIES

By:

Vajran Timothy Sarvendran

A thesis submitted to the

School of Graduate and Postdoctoral Studies in partial

fulfillment of the requirements for the degree of

Master of Applied Science in Nuclear Engineering

The Faculty of Energy Systems and Nuclear Science

University of Ontario Institute of Technology (Ontario Tech University)

Oshawa, Ontario, Canada

May 2021

THESIS EXAMINATION INFORMATION
Submitted by: Vajran Timothy Sarvendran

Master of Applied Science in Nuclear Engineering

Thesis title: CHARACTERIZATION OF PVA-BORAX-FRUCTOSE GEL FOR THE CAPTURE OF RADIOACTIVE WASTES GENERATED DURING NUCLEAR DECOMMISSIONING ACTIVITIES

An oral defense of this thesis took place on May 4th, 2021 in front of the following examining committee:

Examining Committee:

Chair of Examining Committee	Dr. Jennifer McKellar
Research Supervisor	Dr. Glenn Harvel
Examining Committee Member	Dr. Brian Ikeda
Examining Committee Member	Dr. Matthew Kaye
Thesis Examiner	Dr. Filippo Genco, Ontario Tech University

The above committee determined that the thesis is acceptable in form and content and that a satisfactory knowledge of the field covered by the thesis was demonstrated by the candidate during an oral examination. A signed copy of the Certificate of Approval is available from the School of Graduate and Postdoctoral Studies.

Abstract

With the long-term objective of using polymer gels for the capture of solid, liquid and gaseous waste generated from decommissioning works, characterization of gel properties as well as the properties of the individual constituents of polymer gels has been completed. Characteristics of constituents were investigated over varied concentrations and environments. Preliminary thermal degradation characterization found no adverse hysteresis behaviour regarding the polymer constituent. Constituent chemistry as well as chemistry that enables crosslinking between constituents was examined, and the theory that most accurately describes the crosslinking of constituents was established. Understanding of chemistry and characterization results were employed to successfully manufacture varied gels, with varied applications. Variation of gels were achieved via adjustments, primarily to polymer concentrations.

Keywords: Nuclear Decommissioning; Polymer gels; Crosslinking; Polyvinyl-Alcohol; Borax

Author's Declaration

I, Vajran Timothy Sarvendran, declare that this thesis titled, "Characterization of PVA-Borax-fructose Gel for the Capture of Radioactive Wastes Released During Nuclear Decontamination and Decommissioning Activities" and the work presented in it are my own. I confirm that:

- I hereby declare that this thesis consists of original work of which I have authored. This is a true copy of the thesis, including any required final revisions, as accepted by my examiners.
- I authorize the University of Ontario Institute of Technology (Ontario Tech University) to lend this thesis to other institutions or individuals for the purpose of scholarly research. I further authorize University of Ontario Institute of Technology (Ontario Tech University) to reproduce this thesis by photocopying or by other means, in total or in part, at the request of other institutions or individuals for the purpose of scholarly research. I understand that my thesis will be made electronically available to the public.

Signed:

_____

Vajran Timothy Sarvendran

Statement of Contributions

I hereby certify that I am the sole author of this thesis and that no part of this thesis has been published or submitted for publication. I have used standard referencing practices to acknowledge ideas, research techniques, or other materials that belong to others. Furthermore, I hereby certify that I am the sole source of the creative works and/or inventive knowledge described in this thesis.

Acknowledgements

I would like to take this opportunity to express my gratitude to a few, amongst many, who have enabled the successful completion of this thesis.

Thanks to my supervisor, Dr. Glenn Harvel, firstly, for this opportunity, and the several other academic opportunities throughout this continued student-mentor relationship, allowing me to get here; as well as his support, mentorship, infinite patience, and academic teachings. His repository of knowledge and dedication to being a model engineer is beyond inspirational.

Special thanks to Dr. Takeyoshi Sunagawa and Dr. Brian Ikeda. Dr. Sunagawa, for his mentorship, inspiration regarding experimental methods and assistance in the formulation of gels; Dr. Brian Ikeda, for his academic teachings, advice pertaining to chemistry, and his ability to somehow make the topic of inorganic chemistry a strange fascination. Many thanks to my colleagues, Nicholas Somer, and Raj Khurmi for their academic support, scholarly banter, and our shared love for Oreo cookies. Thank you to my supervisory committee, Dr. Glenn Harvel, Dr. Brian Ikeda and Dr. Matthew Kaye for the time they took to assess this work.

Thanks to Dr. Markus Piro and Dr. Bernie Fitzpatrick for access to the Thermogravimetric Analyzer in the Nuclear Fuels and Materials laboratory, as well as assistance provided for the operation of the TGA system. Thanks to the support from OPG/UNENE/NSERC through grants on Nuclear Decommissioning.

Finally, I would like to thank my family, my fiancée, Marian Mamiza and her family. Marian's family for welcoming me with open arms, and Marian, for her support, encouragement and always standing by my side. Her academic and career accomplishments, as well as her many artistic talents serves as a continuous motivation. Thanks to my siblings, for life will be bland without the two of you; the arguments, the fun, memories that will always be cherished. Most of all, thanks to my parents, Deva and Sarva for, disciplining me when necessary, their never-ending love, and the immeasurable sacrifices they have made at their expense, for the benefit of their children; we will forever be indebted to you both.

இந்த ஆய்வறிக்கையை எனது ஆலோசகர், எனது பெற்றோர், நண்பர்கள், மற்றும் எல்லாவற்றிற்கும் மேலாக என் இறைவன் இரட்சகராகிய மீட்பர் இயேசு கிறிஸ்துவுக்கு அர்ப்பணிக்கிறேன்.

Table of Contents

List of Figures

List of Tables

1 Introduction

The term "decommissioning" when applied to a nuclear power plant, refers to the management and technical actions associated with the termination of operations and withdrawal from service. Prior to the shutdown of a facility, the decommissioning process includes planning and execution of three major phases of activity:

i) Storage, and surveillance, including complete site characterization.

ii) Dismantlement and facility demolition.

iii) Site restoration, which may include a return to green site.

Decommissioning is not just demolition, but rather the systematic deconstruction of contaminated and complex nuclear facilities which includes very large components [1]. Decommissioning actions include all activities associated with the dismantling, decontamination and disposal of a facility and its associated structures, systems, components and equipment (including and not limited to the reactor vessel, steam generators, pumps, tanks, and support systems made up of metres of multiple tube networks [2]) and all associated waste products, as well as the remediation of contaminated grounds [1].

In addition to pre-existing waste products, of both traditional and radioactive types, generated during the life cycle of the nuclear facility, all forms of decontamination, dismantlement, and volume reduction processes also generate additional streams of radioactive waste, which must also be addressed via capturing for further processing and disposal. These wastes exist in various physical states, including:

- Solids, including surface level types, which can be addressed via surface decontamination.
- Liquids, such as tritium oxide generated in heavy water when being used as a moderator or coolant during the lifetime of the plant.
- Gases, such as those generated from various dismantling cutting techniques as well as from volume reduction incineration or smelting techniques.

Gels are a method for capturing these wastes. Gels have been used by the nuclear industry for many years, for example: waste capture via the use of gel based strippable coatings for surface decontamination [3]. These polymer gels are formed via polymer chains undergoing a process called crosslinking, wherein, polymer chains become bound to one another, either permanently in the form of chemical bonds or physically, in the form of hydrogen bonds. Surface decontamination gels target solid type wastes on the surface or the immediate sub layers of the contaminated material [4]. Another type of surface decontamination gel technique is a foam that is sprayed onto surfaces. As with the strippable coating method, the decontamination foam acts as a carrier for chemical decontamination agents that dissolve surface level contaminants [4]. Foam type PVA-Borax gels can be used to capture liquid type wastes temporarily. The liquid waste is captured inside the foam where it is maintained by a balance between the capillary effects drawing the liquid into the foam and the gravity effects attempting to drain the liquid out of the form. Specifically, the capillary rise of fluids into PVA-Borax foams occur at a rate that is significantly greater than the ability of fluids to drain out of the foam [5]. Therefore, the foam is temporarily able to retain wastes. In current experience, the foam remains stable only for a couple of weeks, to at most, over a month [5]. As such, foams only have limited applications pertaining to interim capture and storage of liquid wastes.

Outside of waste capture, applications of gels within the nuclear industry exist in the form of Fricke and other types of dosimeters [6, 7]. With regards to Fricke dosimeter type gels, the gel itself acts as a carrier for ferrous sulphate [4], wherein Fe^{2+} transforms into Fe^{3+} due to radiation induced oxidation [6]. Fricke chemicals are often combined with constituents such as acrylic monomers [6] and glutaraldehyde [7] that polymerize rapidly due to radiation sensitivity to create three dimensional dosimeters, which are not just useful within the nuclear and radiotherapy industries but has applications such as sun burn detection due to UVA sensitivity [6, 7].

Besides the nuclear industry, gels have various multi-disciplinary applications. Gels are used in the medical industry for purposes of drug delivery, either trans dermally in the form of skin patches or orally in the form of hydrogel pills. The drug release rate of hydrogel pills can be controlled by the molecular interaction between the polymer gel and the drug. Other applications within the field of medicine include using gels for the purpose of lubrication, for example for contact lenses, catheters, and medical guidewires [8]. An additional application of PVA gels within the field of medicine arises due to the ability to manufacture PVA in such a way that it has anisotropic mechanical properties, similar to tissue, hence PVA hydrogels can be used to

manufacture replacement aorta and cardiovascular tissue [9]. Within the field of electricity and energy storage, PVA-Borax gel due to its electrolytic characteristics, and its ability to be a carrier for anions (such as F^-,Cl^-, and SiO_4^{-4}) and cations (such as Na^+, Mg^{2+}, and K^+), is used to manufacture gel electrolytes for supercapacitors [10]. Specific to the shipping industry, PVA-Polyacrylamide gel coatings are applied to the hulls of boats to prevent marine fouling caused by algae and barnacles, which would result in corrosion due to microbiological attack of the hull and in slowing down of vessels due to biological material buildup [8].

Finally hydrogels such as those of the PVA-Borax type are used for purposes of cleaning artwork because of the gel's ability to remove surface buildup without affecting the original artwork [11]. Furthermore, the hydrogels act as carrier fluids for solvents that are used to remove aged varnish and coatings previously applied during the art restoration process. Traditionally these solvents are applied freely using cotton swabs or small brushes, however, this does not allow for control of capillary flow of the solvent through the surface of the artwork., resulting in the accidental removal of original art material. Using hydrogels as the carrier fluid allows for controlled application of the solvent onto art surfaces, preventing unintended applications onto the original artwork [12].

Applications of gels is not new to the nuclear decommissioning industry, however, the concept of permanently capturing radioactive waste liquids and gases using gels is novel. Gels offer the advantages associated with wet filtration systems such as minimizing clogging, while at the same time eliminating disadvantages of wet filtration systems. Particularly, the mobile state of liquid waste post capture, when captured using gels is in a semi solid state that has a viscosity dependent rigidity. Additional advantages exist in the form of minimal infrastructure required for volume reduction post capture of waste, as well as a simplified that converts the gel into a more rigid state for *in-situ* storage and disposal. The almost negligent additional waste stream produced during this conversion process is yet another advantage.

To permanently capture wastes using gels, issues pertaining to the repetitive homogenous manufacturing of gels need to be addressed. These include:

- Being able to repetitively manufacture homogeneous gels [13]; incorrect constituent concentrations as well as an inadequate understanding of how gel constituents chemically interact with one another can lead to an inhomogeneous demixed gel state; wherein, a portion of the gel content is a solid gel like substance and the remainder of the content is a liquid like substance [14].
- Depending on the methodology used to manufacture gels, disintegration has been shown to occur over large time scales (weeks to months) [5].
- Disintegration of gels due to environmental factors such as high temperatures [15, 16] or extreme alkaline or acidic environments [15, 17].
- Disintegration due to excess concentration of certain constituents [18].

To address these issues an understanding of the chemical interaction between gel constituents as well as characterization of gels and gel constituents is required.

1.1 Problem Statement

Currently there exists no chemical or physical methods by which polymer gels can be used to permanently capture liquid wastes once the gel has been crosslinked. Furthermore, pertaining to gaseous wastes, although polymer gels may be used to capture gaseous wastes, this can only be achieved by gels of very specific rheological characteristics.

It must also be noted that the applications of gels for solid, liquid, and gas waste capture vary as a function of gel characteristics. Gels cannot be employed to capture these various forms of wastes unless the application specific characteristics are determined first, and methods to generate gels repeatedly with application optimal characteristics are developed. Inadequate understanding of chemistry-based constituent interactions leads to further issues such as unintended viscosity or alternatively demixed gels, wherein a portion of the overall substance is a more solid like gel substance and the remainder of the substance is a water like liquid substance.

1.2 Objective

A novel method of capturing wastes of liquid and gaseous nature is by first entrapping these wastes using the individual constituents of PVA borax-fructose gel and then crosslinking the constituents into a gel state to ensure the wastes remain *in-situ*. This work is focused on characterizing PVA borax-fructose gels and their individual constituents, such that the feasibility for capture of liquid and gaseous wastes, using gels, can then be evaluated. To that end, the results of characterization allows for the constituent or even certain forms of gels, with optimal characteristic and concentration to be selected for the capture of liquid and gaseous wastes. The understanding of characterization results is also important for processing after capturing waste, such as the conversion of constituents into gel, and the conversion of gels from a lower to a higher viscosity to ensure waste remains captured.

Characterization includes the understanding of the constituent chemistry, as well as the chemistry of interaction between the three constituents that results in gelation, which is required to be able to successfully manufacture gels using the gel constituents or alternatively for purposes of successfully modifying the characteristics of gels; for example, for purposes obtaining optimal characteristics suitable for disposal while ensuring wastes remain permanently *in-situ* within gels. It must be noted that the objective of this thesis will solely focus on the characterization of gel as a medium to capture waste products. Specific to this thesis, the definition of characterization does not in any manner extend to characterization of the waste products that are being captured. The objective of this thesis will be achieved via the two sub-objectives outlined:

1) Investigation of the role of individual constituents of the gel, including the chemistry that allows for gelation to occur and factors that effect this chemistry.
2) Investigate the change in gel properties as a function of varied constituent concentrations.

1.2.1 Application of Objectives to Problem Statement

The first and second sub-objectives address the understanding of constituents such that the optimal substances can be selected and manufactured for the various applications of radioactive waste capture, as well as post capture processing. Furthermore, the second sub-objective also addresses ability to successfully manufacture gels or modify the characteristics of already manufactured gels.

1.3 Thesis Structure

Chapter 2 provides some background on sources of radioactive wastes, generated from decommissioning processes, and why wastes must be adequately addressed. Chapter 2 also provides a literature review of various forms gels that currently exist, including their capabilities and weaknesses. Chapter 3 provides the methodology for achieving the objectives of this work. This includes the methods for manufacturing of gels, the experiments formed to characterize the gels, and the equipment use to conduct the experiments. Chapter 4 provides quantitative results of experiments as well as any qualitative observations made during experiments. Chapter 5 discusses the results as well as the relationship of results to characterization and the overall objective of this work. Chapter 6 summarizes the work and suggests future work required to attain the overall objective pertaining to PVA-borax-fructose gels and capture of waste products.

2 Literature Review

The following literature review discusses sources of secondary and additional waste streams which are inevitably generated during decommissioning activities, especially during dismantling, volume reduction, and decontamination. Also discussed is why specific attention must be paid to these additional waste streams. Traditional methods of capturing these waste streams is discussed. Lastly, gels are introduced and defined. Various types of gels are discussed, including their various applications and issues. Alternative methods of capturing wastes using gels, including characteristics of types of gels that are desired for purposes of waste capture are discussed.

2.1 Dismantlement and Decontamination

2.1.1 Dismantlement

After the removal of fuel and dewatering of nuclear power plants, dismantlement, decontamination, and further volume reduction of infrastructure must occur so that the site can be returned to an unconditional release state [19]. These processes account for a large portion of decommissioning related radioactive contamination [2] and generate significant volumes of scrap and waste. The scrap and waste are a combination of radioactive and non-radioactive materials, comprised mostly of concrete and steel [20]. For example, 13,000 tonnes of scrap metal was dismantled from the Stade nuclear power plant in Germany, by 2014, 30% of which was melted [21].

Scrap metals and concrete have an inherent value, and when reused or recycled, reduces the environmental impact associated with the production of new resources. Furthermore, there are costs associated with the disposal of scrap materials [20]. These reasons have led nuclear sectors of certain countries like Japan [22] to develop methodologies that meet radioactive clearance levels or for the reclassification of materials such as stainless and carbon steel, which can be recycled or reused both inside and outside the industry [20]. Such methodologies include volume reduction processes.

Volume reduction and decontamination processes can reduce overall costs, simplify logistics and handling, and minimize space required for disposal and burial [23, 24]. CSA N292.6-18, section

5.3.1 [23] states that as part of the long term storage or disposal process, volume reduction processes including, dismantling, compaction, and incineration shall be considered[23]. Most nuclear facilities including the Pickering NPP already have dedicated methods of waste volume reduction, which includes buildings that are specifically dedicated and equipped for the purpose of addressing waste that is generated during regular operations. During the decommissioning stage, any waste volume reduction infrastructure may remain commissioned, to assist with the reduction of wastes generated during the decontamination and decommissioning process [23].

Dismantlement and volume reduction can be achieved via a variety of techniques including cutting [2], smelting, compaction, shredding, incineration and vitrification [20]. The employment of these various forms of dismantlement and volume reduction techniques results in the generation of secondary wastes [25]. Secondary waste streams generated include, sedimented dross, (dross is the by-product of laser cutting, generated when high temperature metal comes into contact with air resulting in oxidized impurities), wall deposits, aerosols [26], off-gases and contaminated slag (via volume reduction methods such as smelting) [25].

These secondary waste streams, especially the ones in the form of liquids or gases, are most problematic since they are harder to capture and do not remain in-situ due to their mobile nature [27, 28]. Decommissioning processes that result in vaporization leads to the production of aerosols of varied sizes [29]. Due to the relatively small particulate sizes, aerosols are of concern, especially given the potential of the particulates to be inhaled by humans and other organisms. Inhalation may result in adverse health effects due to the size of the particulates as well as the potential of these particulates to be radioactive [29, 30]. It's not just the physical state of these secondary wastes that are of concern, the radionuclide species within these wastes such as H^{3}, C^{14}, [31] Cl^{36}, Tc^{99} and I^{129} [32] are also concerning due to their chemical nature of being highly mobile while also having long half-lives [32].

Furthermore, traditional methods of capturing these wastes by filtration can lead to bypassing, clogging, filter rupture, [33] and the generation of additional waste streams [34]. Additionally, once wastes are captured within traditional solid or liquid mediums, they can become mobile again if not promptly taken care of. Using gels rather than traditional methods may allow for the minimization of additional waste streams while ensuring these problematic waste forms remains *in-situ* once captured.

2.1.2 Decontamination and the Unconditional Clearance Level

The purpose of decontamination is to allow for the diversion of radioactive material from the radioactive waste management pathway such that these materials can be recycled or traditionally disposed rather than being disposed of using special handling techniques reserved for radioactive wastes. This is achieved via conditional or unconditional clearance [35]. The unconditional clearance level for Canada, as defined by the Nuclear Substances and Radiation Devices Regulations SOR/2000-207 [36], are detailed in the Appendix, under section 11.1.1.

Decontamination (including unconditional clearance or reclassification) can be achieved by a variety of techniques, including chemical based such as acids, bases and organic solvents,[28] mechanical such as scrubbing [28], and thermal such as laser or plasma scabbling [37]. As with dismantling and volume reduction techniques, all forms of decontamination techniques produce secondary waste streams [2, 26]. Chemical based techniques such as using acids, or organic solvents, directly translate into liquid type, radioactive waste streams. Secondary waste streams in the form of liquids may require additional volume reduction via methods such as dewatering [28] and evaporation [38]. Volume reduction of liquid waste streams in turn produce additional tertiary waste streams, typically in the form of highly mobile [27, 28] gases and aerosols.

To minimize risk to the environment and the public, all forms of additional waste streams must be captured and disposed of adequately. These waste streams are typically in the form of liquids, gases, or aerosols, which contain radioactive contaminants including volatile cesium, iodine, and tritium [25]. Cesium, tritium, and iodine are of special concern because of their volatility and biocompatibility, which can result in these radionuclides being transferred to plants via root uptake, or gas exchange [39]. Tritium for example, can be transferred directly to plants and animals and can become organically bound, which when consumed by humans can result in higher dose coefficients [39].

2.2 Gaseous and Aerosol Waste

Waste in gaseous or aerosol form is, by nature in its most mobile form[40]; gaseous waste is by definition waste in its gaseous physical state of matter, whereas aerosol waste is defined as fine particulate solid or liquid waste suspended in air [41]. The storage and disposal of waste in its aerosol state is both economically unviable [40] and due to its volatility, unsafe. Hence, gaseous or aerosol type wastes must be captured and processed at the source of emission prior to venting to atmosphere.

Venting of radioactive emissions and waste to atmosphere is subject to permissible release limits, established in licences provided by the CNSC [39, 42]. Regdoc-2.9.1 [42] specifies how these limits are calculated, from which Equation 1 has been taken. Equation 1 calculates the derived release limit (DRL), for any source, radionuclide and representative person [39]:

$$DRL = \frac{annual\ dose\ limit}{[\frac{X_9}{X_{0(a)}}]} \qquad \text{Equation 1}$$

wherein, annual dose limit has units of: Sv * a^{-1}, and $\frac{X_9}{X_0}$, known as the dose per unit release has units of: Sv * a^{-1} * Bq^{-1} * s. Calculation of $\frac{X_9}{X_0}$ (where x_0 is the source and x_9 is the human dose) is dependent on various variables including concentration, pathway and transfer parameter (such as via surface soil, atmosphere, well water, etc.). Various pathways, transfer parameters as well as the methodology to calculate dose per unit release based on these variables, are detailed in the "CSA – Guidelines for calculating derived release limits" [39] standard. Based on Equation 1, and assuming a uniform source emission rate and long term average atmospheric conditions derived release limits of radionuclides for nuclear facilities can be calculated [39].

Due to local atmospheric conditions [39], DRLs' are site specific. For example, OPG's Pickering Nuclear Generating Station has an airborne iodine-131 DRL of $2.82 * 10^{12}$ [43]. In comparison OPG's nuclear waste management operations located in Bruce County has an airborne iodine-131 DRL of $1.90 * 10^{12}$ [44]. It must be noted that the OPG environmental data reports

specifically identifies DRLs' of radionuclides such as tritium, carbon-14, and iodine-131, because of the mobile nature of these radionuclides [39, 43, 44].

The purpose of a DRL is to restrict the maximum quantity of nuclear substances being emitted, and are regulatory requirements once written in the license of nuclear facilities [45]. These release permits often also restrict the discharge of conventionally hazardous substances [45]. The required compliance by the CNSC of DRLs' is to prevent negative human, biological and environmental effects via minimizing risk as a function of release [46]. Radiological emissions must be maintained below the DRLs' to meet the terms of operating licences provided by the CNSC [44].

Understanding DRLs' and the mobile nature of certain forms of radionuclides provide the background of why nuclear facilities employ various methods to capture and dispose of radionuclide waste. Methods of capture include traditional wet and dry filtration techniques or potentially novel methods such as gels, as discussed in sections 2.3 and 2.4. Furthermore, to maintain releases below DRL thresholds, it is important for nuclear facilities to ensure radionuclides of mobile nature remain in-situ once captured and in storage. One potential method of ensuring radionuclides remain in-situ once captured is by using gels.

2.3 Methods of Filtration and Capture

Wastes of gaseous or aerosol types are considered to be wastes in its most mobile and difficult to store form [40]; hence it is typically processed as it is generated, at the source. Gaseous and/or aerosol processing systems must also be designed in such a way that generation of additional waste streams are minimized. Typical processing systems are comprised of various types of air purifying components that are sized specific to the range of particle diameters of concern [40]. Filtration systems are important, not just for the capture of aerosolized radionuclide wastes but also traditional wastes that can potentially become aerosolized such as polychlorinated biphenyls (PCBs), and asbestos [47].

With regards to typical dry filtration techniques, particles in the 10^{-3} μm – 0.8 μm range are traditionally filtered via electric precipitation filtration, 0.8 μm – 10 μm via air filtration, and 10 μm – 50 μm particulates, via dust arrester type filtration. Centrifugal type filtration is typically employed

for particles larger than 50 μm. Filtration systems capable of filtering particulates of varied sizes are necessary to ensure regulatory release criteria are met [48]. The final stage of most traditional methods of aerosol filtration systems consist of HEPA filters [48]. HEPA filters are capable of filtering particulates ≤ 1 μm [48]. Alternatively, in the case of certain gaseous and aerosol wastes such as C-14 oxides, iodine and radioactive noble gases, wet filtration, in the form of scrubbers and absorbers that contain acids, hydroxides or other aqueous solutions, are used for filtration [40].

2.4 Gel Based Capture Alternative

The International Union of Pure and Applied Chemistry (IUPAC) defines substances of the gel state as a "non-fluid colloidal network or polymer network that is expanded throughout its whole volume by a fluid" [49]. In other words, gels are defined as a two phase system, [50] consisting of a liquid phase encapsulated within a solid network where both phases are continuous [51]. A description of the continuity of both phases has been described by Brinker and Scherer [51] as "a phase traversable from one side of its sample to the other without entrance into the other phase" [51]. The physical characteristics of substances of this nature can be best described qualitatively as behaving like a liquid in the sense that they take the shape of their container, but at the same time having semi solid characteristics because of its non free flowing behaviour, with a viscosity dependent rigidity. A distinguishable characteristic of gel is the resistance to shear stress and elastic deformation while at the same time having an elastic response [52]. In terms of qualitatively determining gelation, one method is to observe the meniscus of a sample while the sample container is tilted and the meniscus is non horizontal, indicative of gelation [53].

Definitions that are used to describe the various states of transitions from individual constituents to a homogeneous gel state are important to understand. With regards to the definitions "sol" and "solution", it must be noted that these terms are not interchangeable. The term "solution" refers to a phase of solvent and solute that is uniform throughout and homogeneous [52]. The term "sol" is, "a fluid colloidal system of two or more components", where a colloid consists of "molecule or polymolecule type particulates with a dimension between 1 nm to 1 μm in at least one direction that is dispersed within a medium" [52]. For purposes of this thesis, a "sol" will refer to a

state wherein two phases exist: a colloidal phase of dispersed fine particles, suspended within a continuous liquid medium phase.

As defined by IUPAC, the "sol-gel process" (also referred to as "gelation"), describes the process by which a network formation is induced through a progressive transformation from solution to sol and finally gel. The gel point is defined as the initial point at which the number concentration of cross links is adequate for network formation throughout the sample, i.e, a continuous solid and liquid phase exist. This means, a critical concentration of constituents is required to first reach the gel point [54, 55]. After the gel point has been reached, the time scale for sol to gel transition is dependent on the concentration of constituents, with less time required for higher concentrations [53]. The "sol-gel transition" on the other hand, describes the sudden divergence of rheological properties that occurs when the gel point is achieved [52]. Figure 1 provides an illustration of the viscosities of the constituents as well as the dramatic increase in viscosity during the sol-gel process that leads to gelation.

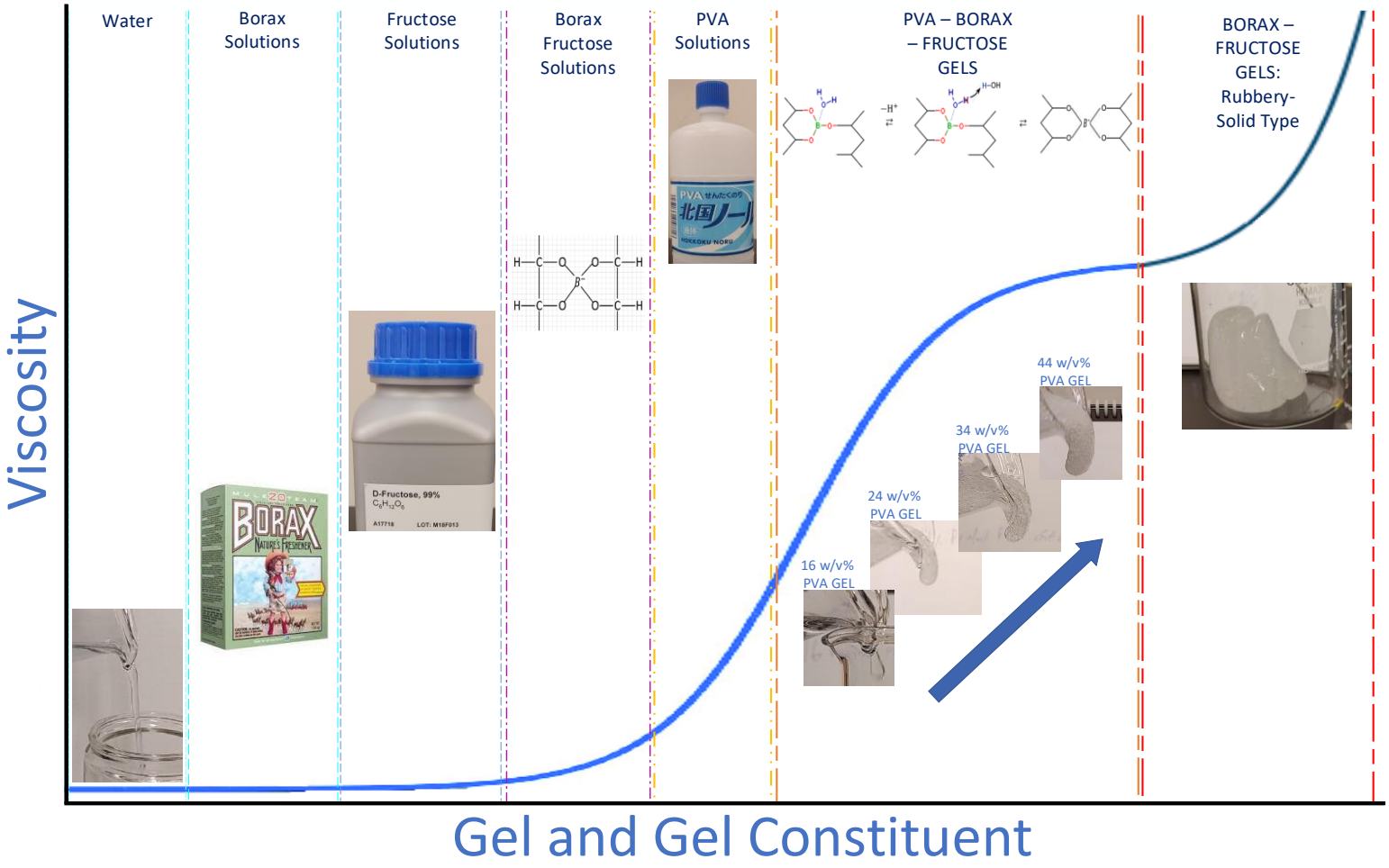

Figure 1: Illustration depicting the viscosities of the constituents relative to one another, as well as the dramatic increase in viscosity during the sol-gel process that leads to gelation

Observable changes to rheology that occur at the sol-gel transition include changes to surface tension [56], storage modulus (G'), loss modulus (G''), damping coefficient, and viscosity. When observing G' and G'' as a function of time, at the point of gelation a dramatic increase in G' and G'' occurs, which is indicative of the sol-gel transition. Equation 2 expresses the storage and loss modulus in one term as a function of damping coefficient (or loss tangent) [53]:

$$\tan\delta = \frac{G'}{G''} \qquad \text{Equation 2}$$

The behaviour expressed by Equation 2 translates into a maximum that is reached at the sol-gel transition [53]. A more accurate method of determining the point of gelation is when the experimentally determined values of G' and G'' reach a point of equal value [53] and then cross over, [57] resulting in G' having a higher value relative to G'' [58].

From the point of G' and G''crossover onwards, $\tan\delta$, when observed as a function of changing rheometer frequency over a period of time, becomes independent [59] At crossover onwards, $\tan\delta$ as a function of frequency is expressed in Equation 3 [57]:

$$\tan\delta = \frac{G'}{G''} = \tan\left(\frac{n\pi}{2}\right) \qquad \text{Equation 3}$$

This frequency independent sol-gel transition in dynamic behaviour is another accurate method of determining the gel point. Alternatively, the sol-gel transition can also be determined by Searle type concentric cylinder viscometers. In this case, the sol-gel transition characteristic that can be measured is viscosity [53, 60]. Specifically, the arresting of G', G'' and $\tan\delta$ characteristics are eventually reflected by viscosity. Due to the above reasons, understanding the viscosity and viscosity variation of gel constituents and the gel as a function of environmental changes are important characterizations, such that:

i) in the event of unintended environmental changes, the characteristics of the constituents or the gel are already understood.
ii) depending on the application of the constituent / gel, the optimal characteristics can be achieved either by constituent concentration adjustments or through temporary modifications to the environment.

Types of gels, depending on the primary constituents used for its formation, can be divided into polysaccharide and non-polysaccharide-based gels. Gels formed from polysaccharides include those that are of the Galactomannan type, which are plant based polysaccharides consisting of at least D-mannose and D-galactose units [61]. Some examples of galactomannan type gels include those made from: xanthan gum [62], fenugreek gum, sesbania gum, cassia gum and guar gum [63].

Polysaccharide based gels have various applications within the cosmetics, oil recovery, [64] food, pharmaceutical and manufacturing industries, particularly for purposes of rheology modification, thickening and suspending agents [63]. A specific example of the use of polysaccharide gel within the field of biomedicine is for the purpose of acting as a carrier agent that delivers cells and bioactive molecules [65] for cartilage or heart valve tissue bioengineering [66]. Outside of biomedicine, an example of galactomannan gel application is within the oil and gas industry. Specifically, for the stimulation or improvement of hydrocarbon extraction from underground formations. In such cases, guar [67] or xanthan gum [64] gels act as a proppant that prevents fractures from closing, such that pathways remain open [67].

It must be noted however that polysaccharide-based gels, due to the nature of the plant derived primary constituent, is prone to biological degradation, particularly via fungal decay [68]. This can be seen in the figures within section 11.1.2 of the Appendix. In order to prevent such decay, antimicrobial additives, such as chitosan may be required [69]. Even with the addition of chitosan, fungal based biological degradation was still prevalent [70]. As part of this study, a xanthan/guar gum gel of 1/1 (w/w) [64] constituent ratio and concentrations of 3% and 5% w/v_{H_2O} were manufactured, sealed with a "Press N' Seal" wrap, and observed over a period of 1 month at room temperature. The result was fungal growth in both concentrations manufactured, as depicted throughout Figure 70-Figure 73 in the Appendix [70].

Other types of gel are those that are based on polyelectrolyte constituents. Such constituents are typically composed of carboxylic acid and depend on the electrostatic interaction of fixed charges on the backbone of the polymer structure for their gel like characteristics [71]. Specifically, in the presence of ionic solutions, deprotonation of the carboxylic acid results in the formation of carboxylate anions and sodium cations [72]. After deprotonation, the negative charge of the carboxylate anion on the monomer causes the repulsion of carboxylate anions attached to other

monomers [73]. This results in the unravelling or uncoiling of the polymer, and is the cause of the gel like behaviour of polyelectrolyte type gels [73]. Sodium polyacrylate, as with other polyelectrolyte polymers is ionic strength dependent for gelation, with the more ionic the solution being, the more gel like the entirety of the substance becomes [71]. As such, the presence of an ionic solution is required for the uncoiling, swelling and retention of gel like behaviour [73].

Conversely, the removal of ionic solution, such as through evaporation, results in polyelectrolyte polymers such as sodium polyacrylate to recoil and loose its gel like consistency. This was shown in a study [70] where $5*10^{-4}$ kg of sodium polyacrylate was used to absorb $6.923*10^{-2}$ kg of water and then left open to the environment at room temperature. After 4 days of evaporation, the mass decreased to $1.493*10^{-4}$ kg and the substance overall, lost its gel like consistency as depicted in Figure 74 and Figure 75 in the Appendix [70].

Yet another type of gel are polymer gels that use boric acid. Specifically, boric acid acts as a crosslinking agent when combined with certain constituents, resulting in sol-gel transition leading to gelation. Such gels are responsive to glucose, are temperature reversible, and can self-heal or restructure post experiencing mechanical disruption. The glucose responsiveness of boric acid gels allows for biomedical applications, such as the self-regulated delivery of insulin [74]. Specifically, the presence of excess glucose results in competitive binding with borates, and the disintegration of polymeric complexes, resulting in the gel returning to a liquid consistency [18]. Boric acid gels can be made by combining with polymers such as polyvinyl alcohol (PVA) which has nontoxic, biocompatibility, and biodegradable properties [75].

Within the field of nuclear decommissioning, one type of gel used is in the form of strippable coatings for surface decontamination. This gel type is manufactured by reacting polyacrylamide-alginate with Ca^{2+} [76]. The gel is used as a carrier agent of magnetic particulates, such as Fe_3O_4, coated with Prussian Blue, a metal ferro-cyanide complex that binds with cesium, allowing for the surface decontamination of ^{137}Cs [76, 77]. After decontamination of surfaces with the gel, the cesium bound particles can then be extracted due to their magnetic characteristics via the assistance of additives, allowing for the gel to be reused [76, 77]. Similarly, PVA-Borate gels containing cesium adsorbing magnetic particles have also been used for surface decontamination. However, unlike polyacrylamide-alginate based gels, additional additives are not required for the extraction of cesium bound particles for the recovery and reusing of the gel [3]. Other applications of gels within the field of nuclear decommissioning include:

1) Bathing small items for decontamination purposes using carrageenan-silicate based gels [78].
2) Removal of ethylenediaminetetraacetic acid from ion exchange resins using anion exchange gels [79].
3) Radio chromic dosimetry using PVA- glutaraldehyde (GTA) based gels combined with potassium iodide [80].

Polyelectrolyte gels lose their gel like characteristics as the ionic solution evaporates[73]. Additionally, stresses that act upon these gels results in deswelling [81]. This was evident in a study where application of local pressure on the sodium polyacrylate gel that was used to absorb water resulted in the local release of water at the pressure point [70].

Of interest to this study are PVA-borax gels, which exhibit temperature reversibility and self-healing characteristics due to the borax constituent [74]. These gels are also non-toxic and biodegradable [75]. PVA is a water-soluble polymer. Various techniques can be used to make PVA undergo sol-gel transition resulting in gelation. One such technique is irradiation based, [82] and another is through repeated freeze-thaw cycles [83]. It must also be noted that the physical or chemical crosslinking that occurs in PVA – borax systems is dependent on the formation of bonds (hydrogen based or otherwise) between these two constituents [84].

PVA-borax type gels may be used for the capture and disposal of various forms of wastes generated during decommissioning works, including dismantlement, volume reduction as well as decontamination.

2.5 Summary

Dismantlement and decontamination of radioactive infrastructure can be achieved by a number of techniques, all of which produce secondary and tertiary wastes. These wastes exist in several physical forms (solids, liquids, gases, aerosols), and sizes. Depending on the form and the size of the waste, various traditional techniques can be employed for the capture, storage and disposal.

Gels provide an alternative methods of waste capture and disposal, without the disadvantages of dry filtration techniques, which are prone to clogging, or the disadvantages of wet systems, which requires additional steps such as dewatering or evaporation. Specific to gels, PVA-borax types with biodegradable, reversible, and self-healing properties as well as multiple methods of achieving gelation may be used for the capture and disposal of wastes generated from the various decommissioning processes.

Characterization of the gel and gel constituents, specifically the change in behaviour as a function of varied constituent concentrations, will allow for the manufacturing of gels with the most optimal application specific characteristics. Application specific characteristics are all dependent on viscosity [85, 86], and variation of gel can be achieved through the variation in viscosity dependent characteristics. These characteristics include storage modulus, loss modulus, and $\tan\delta$ [85, 86]. Storage modulus describes the stiffness of polymeric materials [87], and the ability of materials to store energy [88]. Loss modulus describes the viscous properties of a polymer [89], the ability of materials to loose energy [88]. Damping coefficient, $\tan\delta$, describes the ratio of storage to loss modulus and the efficiency of the material to dissipate energy [88]. Application specific optimization of characteristics include:

i) a relatively low viscosity gel with a relatively high loss modulus, and $\tan\delta < 1$ which is ideal for fluid flow processes such as aerosol capture via bubbler column methods.
ii) a putty like viscosity type gel with a damping coefficient $\tan\delta = 1$, which is optimal for surface contamination capture.
iii) A relatively high viscous and storage modulus gel, which is optimal for long term *in-situ* storage.

3 Materials

The gel is comprised of 4 constituents: Polyvinyl alcohol (PVA), di-sodium tetraborate decahydrate (borax), Fructose and water. Background and details pertaining to each of these constituents (omitting water), including the manufacturer of the constituents used for producing the gel are further detailed within this section.

3.1 Polyvinyl Alcohol

Polyvinyl alcohol is a non-toxic polymer and is considered to be a polyhydroxy (defined as consisting of multiple OH) groups). Due to the hydrophilic and biocompatible properties of PVA, it is considered a biodegradable, non-toxic polymer [90]. Furthermore, PVA is considered to be a polymer with a relatively high dielectric strength, and has high transparency [90].

Polyvinyl alcohol can be obtained through the hydrolysis of polyvinyl acetate [90], which results in the replacement of the acetate groups with hydroxyl groups, resulting in a polymer chain with a variation in the number of acetate and hydroxyl groups, depending on the hydrolysis process. One methods of manufacturing PVA is through the hydrolysis of polyvinyl acetate using an alkaline catalyst, such as Sodium Hydroxide [91], in the presence of methanol (a Bronsted-Lowry type fluid), the solvent [91].

The degree of polymerization (DP) is defined as the total number of monomer units in the polymer [92]. The degree of polymerization is calculated according to the following equation:

$$DP = n + m \qquad \text{Equation 4}$$

A single repeat of a hydroxyl group (n from Equation 4) and an acetate group (m from Equation 4) is defined as the monomer unit [92, 93]. Figure 2 provides a depiction of the hydroxyl and acetate groups of a PVA chain.

The degree of saponification (SD), also referred to as the degree of hydrolysis is the ratio of the number of hydroxyl groups to the total number of monomer units in the polymer, [93] and is calculated according to the following equation [93]:

$$SD = \frac{n}{n+m} \bullet 100 \qquad \text{Equation 5}$$

The acetate groups of the PVA chain are hydrophobic [94]. The hydroxyl groups of the chain are hydrophilic since it provides sites for forming hydrogen bonds with hydroxyl groups of other molecules [95]. As such, the degree of saponification from Equation 5 is an indication of the ratio of hydrophilic groups of the polymer. Varied conditions of the saponification process of PVA can result in varied degree of hydrolyzation (fully or partially hydrolyzed).

Figure 3, compares fully hydrolyzed to partially hydrolyzed PVA [96]. Fully hydrolyzed (degree of hydrolysis is 98% - 99.8%) PVA, as depicted in Figure 3, is relatively insoluble in water and requires relatively high temperatures (> 353.15 ^{o}K) for dissolution. The solubility of partially hydrolyzed PVA depends on the molecular weight. Partially hydrolyzed PVA, as depicted in Figure 3, with a relatively high polymer average molecular weight (or reduced # of repeating OH groups) are less soluble in water and require elevated temperatures [96].

A higher percentage of hydroxyl groups (OH), or higher the degree of saponification, means a more orderly array along the backbone chain uninterrupted [97] by the acetate group; this is ideal for gelation as acetate groups do not participate in the gelation process; rather the higher the degree of hydrolysis the higher the number of OH groups available for crosslinking with borax (PVA – borax crosslinking theory is discussed in section 3.2), resulting in a higher degree of gelation. The PVA used for constituent characterization and production of gels was obtained from Japan, specifically, from Hokokukoryo Inc, under the product name of Hokoku-nol, in a 10 w/w% aqueous solution form, with a polymerization degree of 2000, and a saponification degree of 87.6%.

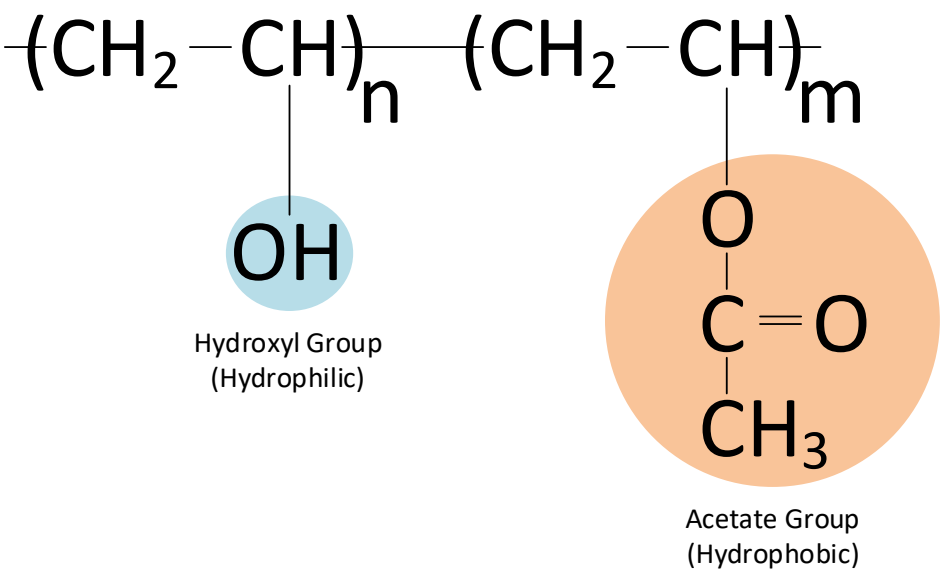

Figure 2: Hydroxyl and Acetate Groups of the PVA repeat chain identified

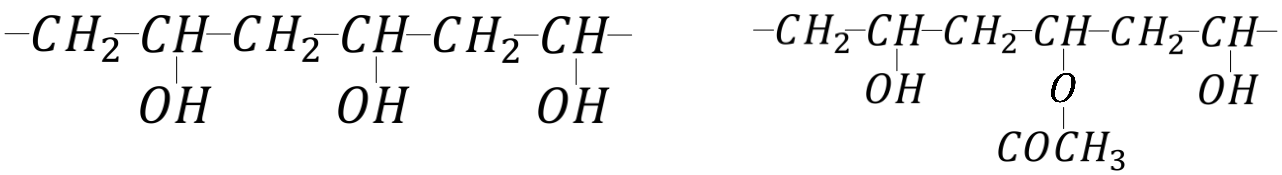

(a) Fully Hydrolyzed (b) Partially Hydrolyzed

Figure 3: Comparison of PVA - Fully Vs Partially Hydrolyzed PVA polymer chains

3.2 Di-Sodium Tetraborate Decahydrate

Borax (also referred to as sodium borate/ sodium tetraborate / disodium tetraborate or di-sodium tetraborate decahydrate) is the most common mineral form of boron and is the precursor for the manufacturing of boric acid. It is commonly used as a preservative, antiseptic, fungicide and for flame retardation. Anhydrous borax has a reported melting point of 1016.15 °K and a boiling point of 1848.15 °K. Borax is known to have a relatively low solubility limit of 5 wt% [98]. Borax has various states of hydration, (ranging from anhydrous to decahydrate) some of which are: [99]

anhydrous borax : $Na_2B_4O_7$

borax pentahydrate : $Na_2B_4O_7 \cdot 5H_2O$

borax decahydrate : $Na_2B_4O_7 \cdot 10H_2O$

The borax used for the manufacturing of the gels are obtained off the shelf, from convenience stores such as Walmart, specifically, the borax used in this work was manufactured by "20 Mule Team", with a CAS# 1303-96-4 [98]. The hydration state of this borax depending on the environmental conditions of storage and transportation can vary widely.

Although the constituent concentration of borax is specified, the hydration state of borax isn't, and as such, this can affect the total concentration of water used in the gel as a function of the varied state of borax hydration. Although the gel may be manufactured according to constituent concentration specifications, repeatability and verification through literature tabulated density and viscosity can only be achieved when identical constituents (such as borax of identical state of hydration) are used. With regards to borax used in this work, the manufacturer specifications states that the borax is of decahydrate form [98]. It is important to verify this state of hydration, such that all future gels manufactured are of the same form ensure repeatability of characteristics.

To verify the hydration state of borax, the temperature setpoints and time required to transform states of hydration must be first identified. Sahin et al [100], and Kocakusak et al [101] have reported temperatures and times required to achieve various stages of hydration. The various hydration stages of borax, including temperatures and time required to achieve the hydration stages are specified in Figure 4. It can be observed that for the borax dihydrate stage, authors reported different temperature ranges to achieve the same stage of hydration [100, 101]. Similarly, authors

reported slightly varied temperatures for the different stages of hydration levels. As stated by Ruhl et al [102], this is because of the varied heating rates used by the different authors. Ruhl et al reported achieving BPH at 391 °K and anhydrous borax at 434 °K [102]. Based on the known hydration levels from literature, and through thermogravimetric analysis (which provides mass and temperature readings as the borax is being evaporated), the hydration state of borax can be calculated. Specifically, the hydration state can be driven to a specified known setpoint (by evaporating the water content of the borax) under continuous measurement of mass and temperature, after which the plots generated from the Coats and Redfern method [103] can be used to calculate the initial state of hydration.

When in aqueous solution, borax dissociates into the $B_4O_5(OH)_4^{2-}$ ion, which is known to be a weak base. The $B_4O_5(OH)_4^{2-}$ ion, reacts with water and further dissociates into hydroxide ions (strong base) and boric acid (weak acid) [104-106], which due to being a weak acid accepts OH- and exists in the form of $[B(OH)_4]^-$ and H_3O^+[107]. The multi-equilibria dissolution of borax in water, that results in the formation of sodium as well as boric acid and borate ions is detailed in the Appendix, under section 11.2.1. The multi-equilibria reactions can be combined into one reaction, according to the following expression:

$$Na_2B_4O_7 \bullet 10H_2O \rightarrow 2Na^+ + 4B(OH)_4^- + 2H^+ + H_2O \qquad \text{Equation 6}$$

According to the two major PVA-borax gelation theories from literature, it is either the boric acid or the tetrahydroxyborate ion species from the equilibria reaction in Equation 6 that is responsible for crosslinking with PVA. Based on Equation 6 and its respective solubility constant (K_{sp}; The $\log K_{sp}$ of this equilibrium reaction at 295.65 °K was reported to be -24.8 by Xiong *et al.* [108]), the concentration of tetrahydroxyborate Ion ($B(OH)_4^-$), as well as H^+ can be calculated at equilibrium, prior to the addition of any other constituent. The determination of ($B(OH)_4^-$), as well as H^+ is important as it then allows for the determination of the concentration of H_3BO_3 at equilibrium. The concentration of $B(OH)_4^-$ and boric acid at equilibrium can then be used to approximate the concentration of the crosslinked species responsible for gelation.

It must be noted that when the concentration of boric acid exceeds a concentration of 0.025 M [109], the equilibria no longer adheres to the weak acid behaviour; rather boron also associates with three or four oxygen atoms to form poly-borate species, the most prevalent of which are $B_3O_3(OH)_4^-$ [109, 110] and $B_5O_6(OH)_4^{2-}$ [110]. These poly-borate species must be accounted for when determining the equilibrium concentrations of ($B(OH)_4^-$), as well as H^+, when Boric acid molarity is greater than 0.025 M.

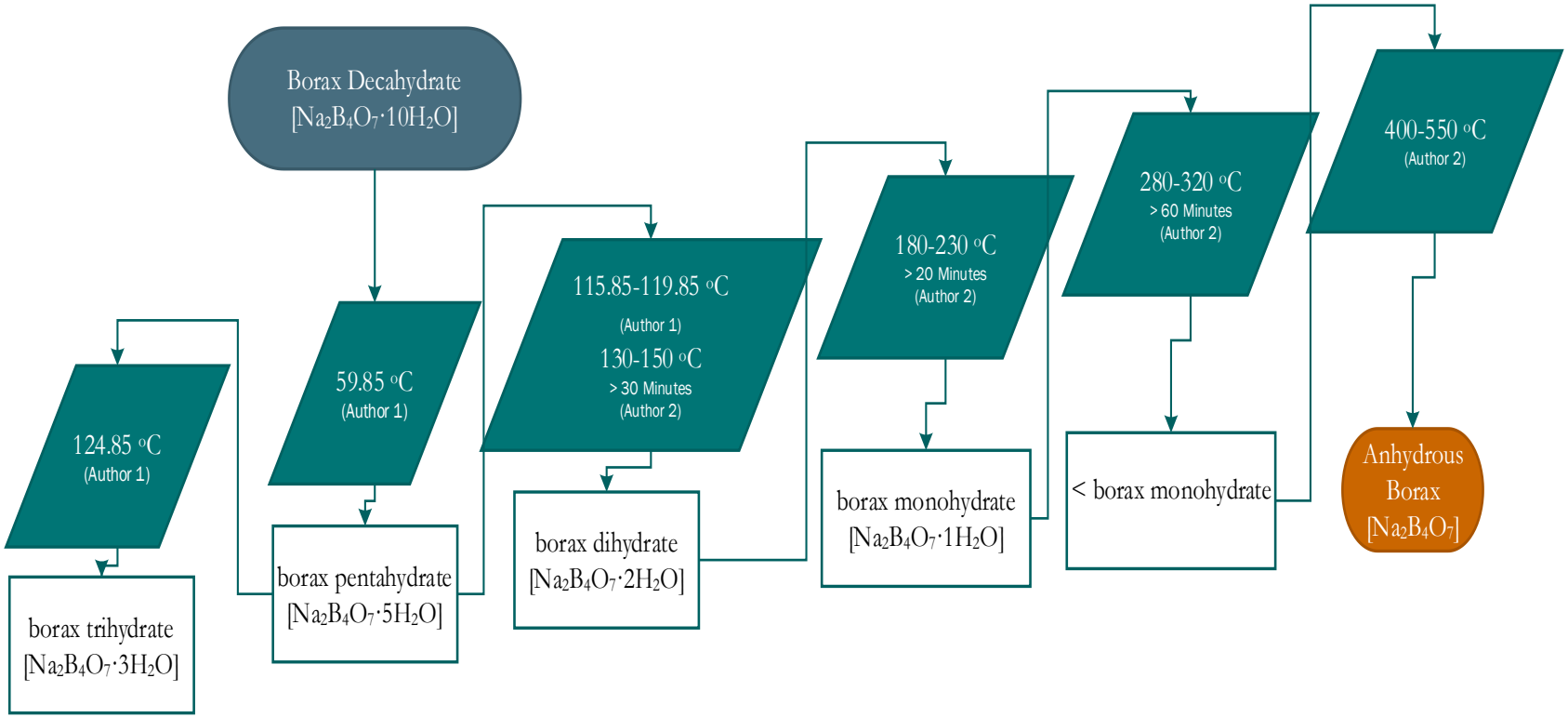

Figure 4: Various stages of borax hydration – Decahydrate to Anhydrous; Author 1 = [100], Author 2 = [101]

3.3 Fructose

Fructose is a secondary constituent required for aiding in the manufacturing of gels and exists as the $\beta - D$ fructopyranose tautomer [111]. In aqueous solution, fructose does not dissociate but rather exists in various other cyclic tautomer forms: 68.2% of the $\beta - D$ fructopyranose form, 22.4% of the $\beta - D$ fructofuranose form, 6.2% of the $\alpha - D$ fructofuranose form, 2.7% of the $\alpha - D$ fructopyranose form and 0.5% of the linear keto form [112]. These tautomer forms are depicted in Figure 5 [113].Of the various tautomers depicted in Figure 5, the ones of interest to this work, due to their capability to form complexes with boronic species, are $\beta - D$ fructofuranose, $\alpha - D$ fructofuranose and $\beta - D$ fructopyranose [114].

Fructose is typically used in the chemical industry for the purpose of aiding in the solubility of hydrophobic ingredients [112], as is the case with the assistance in the dissolution of borax. A 10 w/v% fructose solution has a viscosity of 1.18 cP at 293.15 °K and 1.02 cP at 298.15 °K, according to literature [115]. D-Fructose used for constituent characterization and production of gels were manufactured by Alfa Aesar (product # A17718, CAS#57-48-7), with a pH of 5-7 at 298.15 °K, and a melting point of 376.15 °K – 378.15 °K, according to the manufacturer MSDS [116].

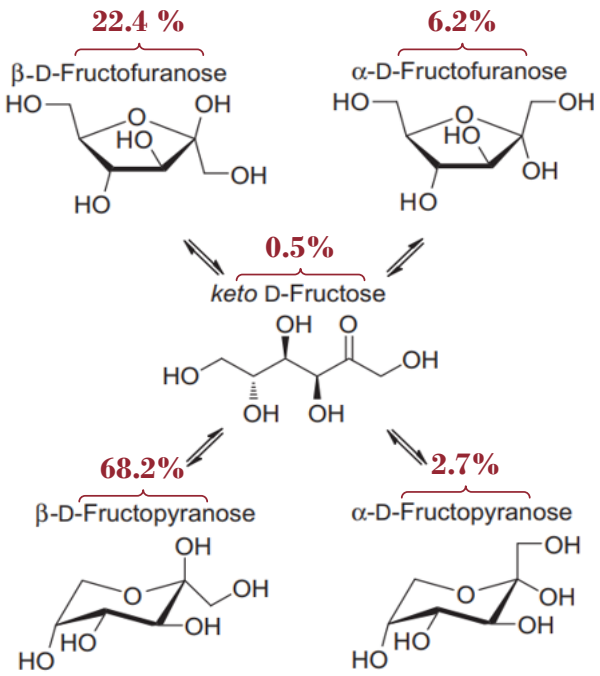

Figure 5: D Fructose in aqueous tautomeric forms [113], including relative abundance in aqueous solution [112]

4 Theories of Gelation Chemistry

This section will discuss the theory of gel formulation and the main issues pertaining therein. Furthermore, the chemistry of interaction between constituents is also detailed here. This provides an understanding of how the sol to gel transition, which leads to gelation, is enabled. The chemistry of interaction is also important to understand phenomenon such as demixed gels, which occur when procedures for mixing are performed incorrectly.

4.1.1 Borax-PVA Crosslinking Theories

Understanding the interaction chemistry of borax constituent with PVA is important to be able to understand sol to gel transition and gelation. The two major PVA – borax gelation theories found in literature, as well mechanism believed to be responsible for gelation have been detailed in the following sub-sections.

4.1.1.1 Borax-PVA Crosslinking: Theory 1

One theory suggests that borax – PVA crosslinking occurs through the tetrahydroxyborate ion, which is expressed as $\mathrm{B(OH)_4^-}$; produced through the ionization of boric acid, as expressed in Equation 7:

$$H_3BO_3 + 2H_2O \underset{\rightleftarrows}{K_a} [B(OH)_4]^- + H_3O^+ \qquad \text{Equation 7}$$

Tetrahydroxyborate ions crosslinks with PVA, as described in Figure 7 part (a) Mono-diol complexion, resulting in sol-gel transition, leading to gelation. According to this theory, sol-gel transition occurs through $B(OH)_4^-$ mono-diol [117]/di-diol complexion with 1,2 PVA diols. A diol is defined as a compound containing two hydroxyl groups, and a mono diol describes a singular pair, whereas a di-diol describes 2 pairs.

In the case of 1,2 PVA diols, OH repeat units are incident or besides each other; rather than 1,3 diols where OH repeat units are alternating, as depicted in Figure 6 [14]. The mono-diol/di-diol complexation depicted in Figure 6 results in a reversible condensation reaction, [106] forming the gel. Alternatively, some literature states that gel formation occurs due to crosslinking via hydrogen bonding as depicted in Figure 8 [117]:

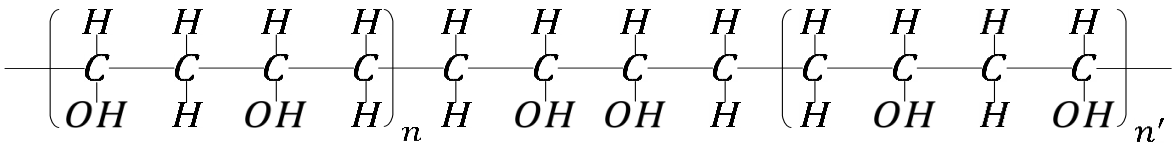

Normal sequence 1,3-diol | 1,2-diol | Normal sequence 1,3-diol

Figure 6: 1,2 and 1,3 PVA Diols (Fully Hydrolyzed) [14]

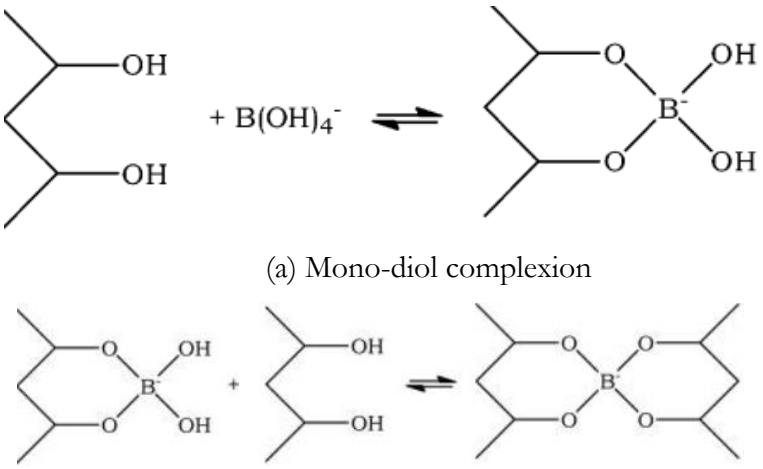

(a) Mono-diol complexion

(b) Di-diol complexion

Figure 7: Mono-diol and Di-diol complexion of tetrahydroxyborate ion with PVA according to Borax-PVA crosslinking theory 1 [117]

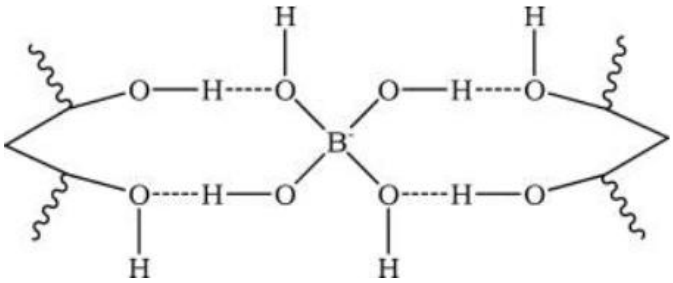

Figure 8: Borax PVA Crosslinking Via Hydrogen Bonding (Indicated Via Dashed Lines)

4.1.1.2 Borax-PVA Crosslinking: Theory 2

An alternative theory of borax – PVA crosslinking is enabled through Boric acid (expressed H_3BO_3), which is produced through the dissociation of the tetraborate ion, as expressed in Equation 4 on page 24, crosslinking, instead of the tetrahydroxyborate ion, as suggested by theory 1. This theory proposes crosslinking through mono-diol [117]/di-diol complexion with 1,2 - 1,2 and 1,2 - 1,3- PVA diols, which results in a reversible condensation reaction, [106] forming the gel. Angelova *et al.* [118] reported that borax PVA complexion based gelation is only stable at a higher than neutral pH with optimal complexion occurring between $8 \leq pH \leq 11$.

Several authors [17, 119, 120] have postulated crosslinking is enabled via Boric acid. Bishop *et al.[17]* shows this via driving the pH of the crosslinked environment greater than 12, where only the $B(OH)_4$ species exist and observed a drop in crosslinking concentration. From this the author concluded that if tetrahydroxyborate ion was the method of crosslinking then an increase in crosslinking concentration rather than a decrease should have occurred in environments of highly basic pH levels of >12 [17]. The experiment of increasing the pH of the environment greater than 12 performed by Bishop *et al.* is one of the reasons why the postulation of crosslinking through boric acid, rather than tetrahydroxyborate ion is validated.

Boric acid – PVA crosslinking occurs firstly via a mono-diol complexion wherein 1,2 – 1,2 diols are bound by oxygens of the boric acid on the left side and a 1,3 diol is bound by one oxygen of on the right side, stabilized by a water molecule [118], as depicted in Figure 9 [118, 121]. At increased basicity, boric acid converts to tetrahydroxyborate ion, via a hydroxide attack or a deprotonation of the coordinated water depicted in Figure 9, to form a tetrahydroxyborate ion – PVA di diol cross link depicted in Figure 10 [118].

Intuitively, in cases wherein the pH falls below 7, as per Le Chatelier's principle, boric acid should increase relative to tetrahydroxyborate ion, and as a result, the number of complexions should increase; however, it must be noted that mono-chelate complex is relatively unstable compared to when boric acid is converted to tetrahydroxyborate Ion when the pH is higher than 7.

Furthermore, when the pH falls below 7, the hydroxyl groups of the polymer chain become protonated, occupying the diols and preventing the PVA diols (which favor chelation) from forming chelates with the Boric acid. [118].

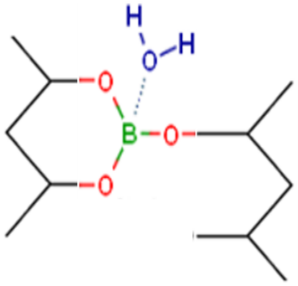

Figure 9: PVA mono-diol crosslinking; Stabilized by water molecule.

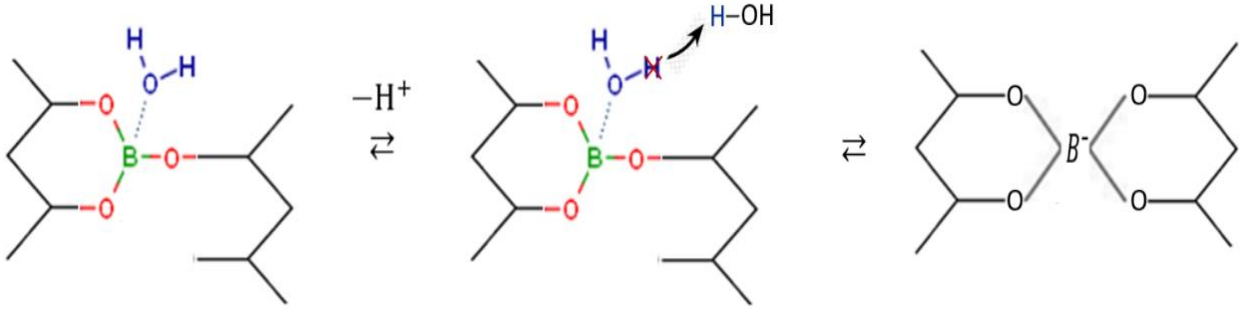

Figure 10: Di-Diol crosslinking of Boric Acid and PVA via deprotonation

4.1.1.3 Borax-PVA Crosslinking: Comparison of Theories

Reactions between an alcohol group and tetrahydroxyborate ions are similar to ether formation reactions which are enabled by dehydration, and requires time, measurable via NMR time scales. Similarly, for the alcohol-borate reactions, time is required to overcome activation energy. Contrary to this however, as observed by Rietjens [120], the equilibrium between boric acid and borate is faster than nuclear magnetic resonance (NMR) time scales; hence the reaction is fast, reflected by its low activation energy (20.5 kJ/mol). Compared to $B(OH)_4^-$, the trivalent boron in boric acid, with an empty p orbital is very electrophilic and rapidly reacts to form complexes. Based on this, the author concluded that it is boric acid that is much more likely to be the agent of complexations [120].

To summarize the findings in literature:

i) there is not enough time for PVA complexation with tetrahydroxyborate ions [120]
ii) boric acid is relatively electrophilic compared to $B(OH)_4^-$ [120]
iii) a drop in crosslinking concentration, rather than an increase was observed by authors at a pH greater than 12, wherein only $B(OH)_4^-$ ions exist [17]

The theory found to be most accurate has been depicted visually in Figure 11. Based on the above findings in literature, Boric acid was ascribed to be the Borate dissolution species that is responsible for crosslinking with PVA. Borax species complexation with Fructose, discussed in the below sections, further compounds the theory of Boric acid being the species responsible for crosslinking.

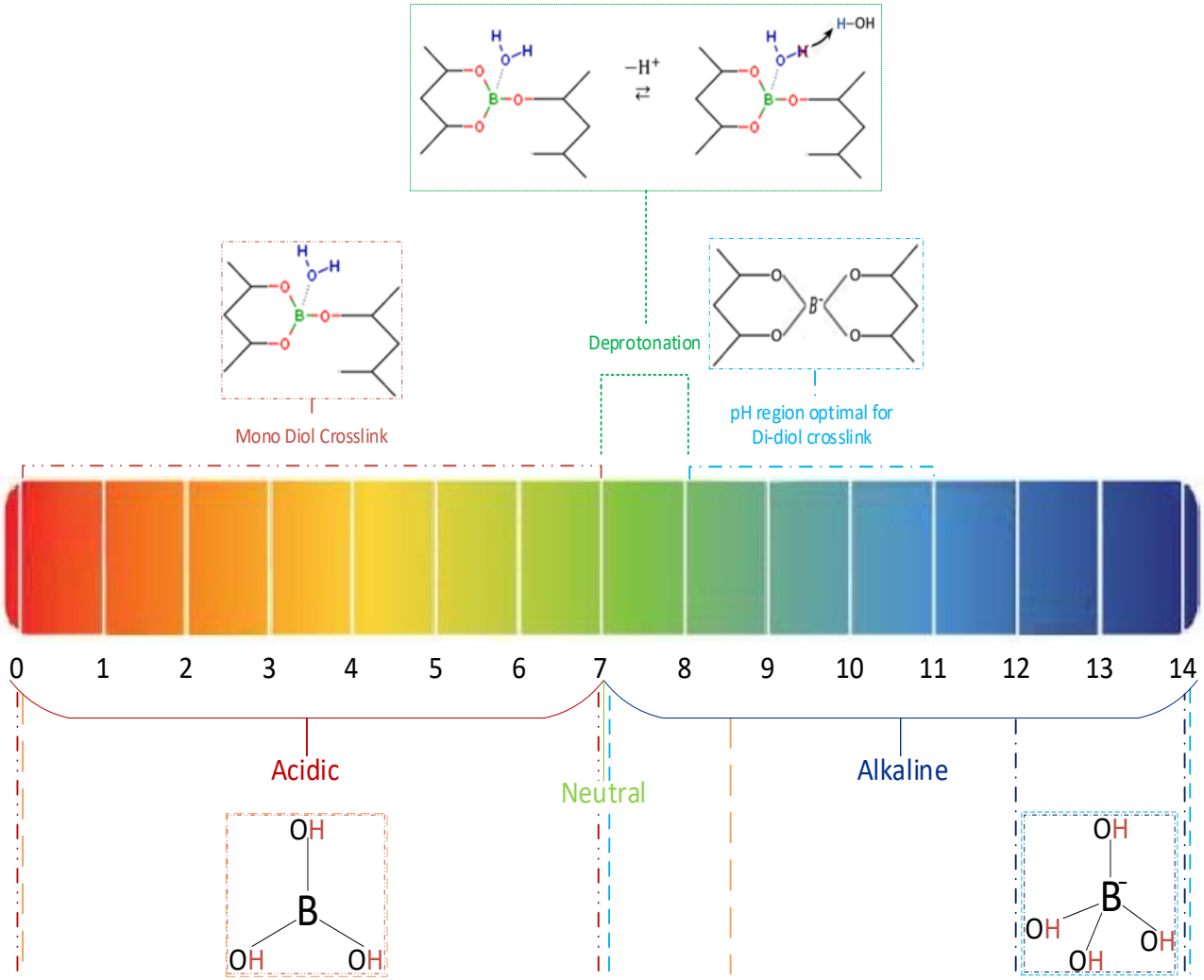

Figure 11: Visual Depiction of Mono-Diol and Di-Diol Crosslinking of Borax and PVA according to the Borax-PVA Crosslinking theory found to be most accurate, relative to the pH scale.

4.1.2 Borax-fructose Complexion

Fructose plays two key roles in the PVA-borax gel making process by increasing the solubility limit of borax as well as by creating a more acidic environment; the resulting acidic environment aids in the prevention of localized high concentrations of crosslinking (which causes the solvent to become immobilized resulting in a demixed, semi-solid state [14]). Details pertaining to how Fructose enables an increase in the solubility limit of borax and causes acidification of the environment have been elaborated on in the following paragraphs.

Fructose is known to aid in the dissolution of hydrophobic constituents [112] by forming complexes with other constituents; this results in an increase in the solubility limit according to Le Chatelier's principle. Specifically, the addition of fructose into a borax solution results in the formation of fructo-borate complexes through the various D-fructose cyclic tautomers, as detailed by Xia et al., and shown in Figure 12 [114].

The borax-fructose complexation, according to Le Chatelier's principle, results in the multi-equilibria reaction to be driven to the right, which results in the borax dissolution products from Equation 7 being consumed, in turn allowing for further addition of borax on the left. The specifics pertaining to the borax – Fructose complexation are provided in the following sub-sections.

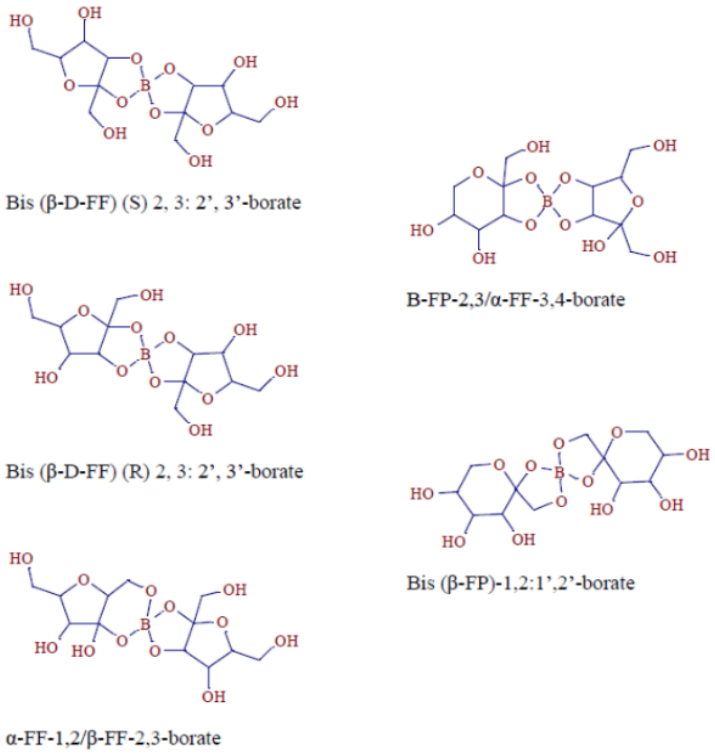

Figure 12: Various Fructose Tautomer Complexions with Tetrahydroxyborate Ion [114]

4.1.2.1 Borax-fructose Complexion: Theory 1

One theory of borax-fructose complexion that results in environmental acidification through fructose is by the complexion with boric acid, as depicted in Figure 13 [122-124]. Based on this complexation, the following expression describing the reaction can be written:

$$H_3BO_3 + C_6H_{12}O_6 \rightleftarrows HBO_3 \cdot C_6H_{10}O_4 + 2(OH) + 2H^+ \qquad \text{Equation 8}$$

The complex (in Figure 13) then dissociates to release H+. Similar to fructose, other polyhydroxy compounds such as glycerol or mannitol have the same effect when added to the gel, resulting in environmental acidification and a weaker gel [14]. The saccharide-boric acid complex dissociation and the production of H^+ is depicted in Figure 14 [125]. Based on this complexation, the following expression describing the reaction can be written:

$$HBO_3 \cdot C_6H_{10}O_4 + 2(OH) + 2H^+ \rightleftarrows BO_3 \cdot C_6H_{10}O_4 + H^+ \quad \text{Equation 9}$$

Rather than the dissociation above, an alternative possibility is that the saccharide-boric acid complex could result in the doubly coordinated borate-hexose complex [107] reaction [125], as depicted in Figure 15. This doubly coordinated fructo-borate complex can be described in the expression below:

$$HBO_3 * C_6H_{10}O_4 + \mathrm{C_6H_{12}O_6} \rightleftarrows \mathrm{BO_4^-} \cdot 2(C_6H_{10}O_4) + H_2O + H^+ \quad \text{Equation 10}$$

Regardless of which of the two reactions depicted in Figure 14 or Figure 15 occurs, an overall release of protons is evident. It should also be noted that the resulting acidification of the environment [107] causes a shift towards the left, specifically for the last step of the borax multi-equilibria dissolution. The tetrahydroxyborate ions ($B(OH)^-_4$) protonate and reverts to boric acid, during which H+ detaches from H_2O, and proceeds to attach with an OH- leg from the $B(OH)^-_4$, resulting in two H_2O molecules.

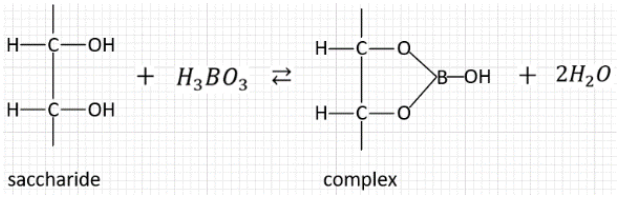

Figure 13: Saccharide-boric acid complexation

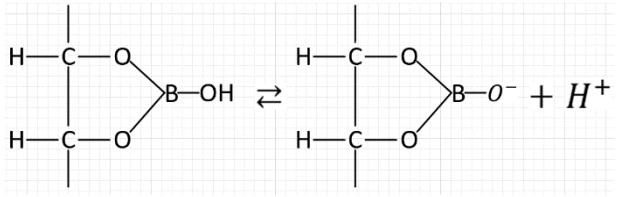

Figure 14: Saccharide borate complexation, Scheme A

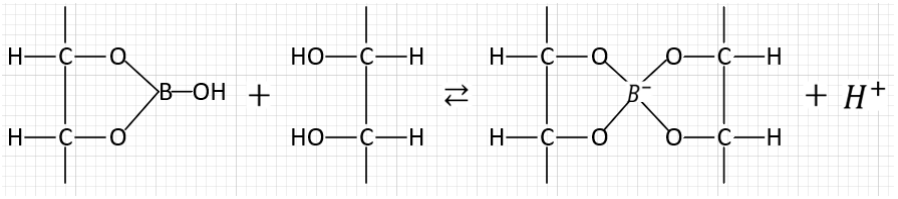

Figure 15: saccharide borate complexion Scheme B

4.1.2.2 Borax-fructose Complexion: Theory 2

An alternative theory for environmental acidification by fructose was proposed by J. Boeseken [124]. borax dissociation produced boric acid which transforms into a tetrahydroxyborate ions. Boeseken [122] proposed that the tetrahydroxyborate ion produced from boric acid ionization complexes with fructose rather than the boric acid itself resulting in a fructo-borate complex and the production of two water molecules, as shown in Figure 16 [122]. This fructo-borate complexation reaction is expressed in Equation 11:

$$B(OH)_4^- + C_6H_{12}O_6 \rightleftarrows [H_2BO_4 \cdot C_6H_{10}O_4]^- + 2H_2O \qquad \text{Equation 11}$$

The fructo-borate complexion described in Figure 16, complexes further, in the presence of additional fructose molecules, to produce a di-fructo-tetraborate complex, and two water molecules, as shown in Figure 17 [122]. This doubly coordinated fructo-borate complex is expressed in Equation 12:

$$[H_2BO_4 \cdot C_6H_{10}O_4]^- + \mathrm{C_6H_{12}O_6} \rightleftarrows \mathrm{BO_4^-} \cdot 2(C_6H_{10}O_4) + 2H_2O \qquad \text{Equation 12}$$

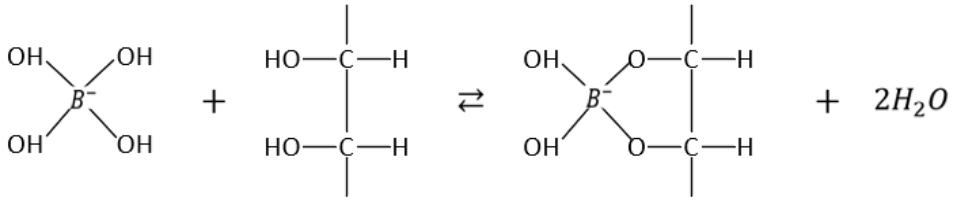

Figure 16: Tetrahydroxyborate based saccharide borate complexion, Scheme A

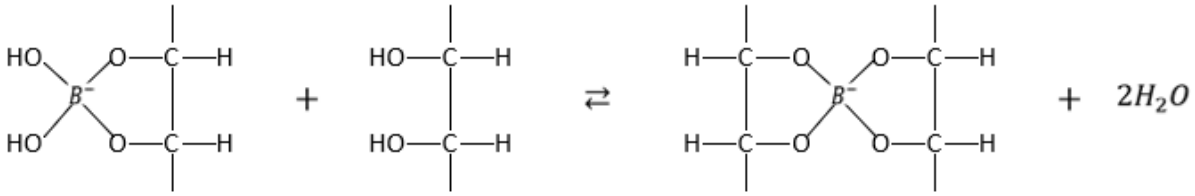

Figure 17: Tetrahydroxyborate saccharide borate complexion, Scheme B

4.1.2.3 Borax-fructose Complexion: Theoretical Correlations

The Grunberg-Nissan and the Tamura-Kurata theoretical correlations, can be used to validate the interaction between Fructose and borax. The Grunberg-Nissan correlation is expressed in Equation 13 [126]:

$$\log_{10}\eta_m = x_1 \log_{10}\eta_1 + x_2 \log_{10}\eta_2 + x_1 x_2 d \qquad \text{Equation 13}$$

From Equation 13, the x variables represent mole fractions of the individual constituents, and the d variable represents the interaction coefficient, which is solely temperature dependent but is independent of the solution composition. This equation is employed under the hypothesis that no interaction/complexion between any two constituents occurs. The Tamura-Kurata equation is expressed as per Equation 14 [126]:

$$\log_{10}\eta_m = x_1 \eta_1 \boldsymbol{\varphi_1} + x_2 \eta_2 \boldsymbol{\varphi_2} + 2\eta_{12}(x_1 x_2 \varphi_1 \varphi_2) \qquad \text{Equation 14}$$

From Equation 14, notations identical to Equation 13 are used. Furthermore, $\boldsymbol{\varphi}$ is the volume fraction and η_{12} is the interaction coefficient that is both dependent on the viscosity of the combined fluid and temperature. η_{12} was determined by using least square regression analysis, an output of which is the interaction coefficient between the viscosity of borax and the viscosity of fructose. It is used under the hypothesis of interaction between any two constituents. [126]

Taking the simplest model of viscosity for binary mixtures, the Graham model [127], the viscosity of the mixture is approximated by the summation of the of the product of viscosity and mole fraction of the individual components, as expressed in Equation 15:

$$\mu_{Mixture} = \sum_i (x_i * \mu_i) \qquad \text{Equation 15}$$

5 Methodology

5.1 Description of Approach

Reiterating the objective of this work: the investigation of the feasibility and advantages of using a PVA-borax based gel as an alternative to traditional methods of capturing and storing wastes generated from decommissioning works. To that end, it is critical to characterize the gel and its individual constituents such that the behaviour of the gel and its respective constituents are well understood. The understanding gained through characterization will then allow for the determination of application specific optimized gel characteristics, as well as determination of methods for repeatable manufacturing capabilities. This chapter provides details pertaining to the various methods used to characterize the individual constituents of the gel, as well as the gel itself. A flowchart, depicted in Figure 18 provides a description of the approach used to meet the objectives of this work.

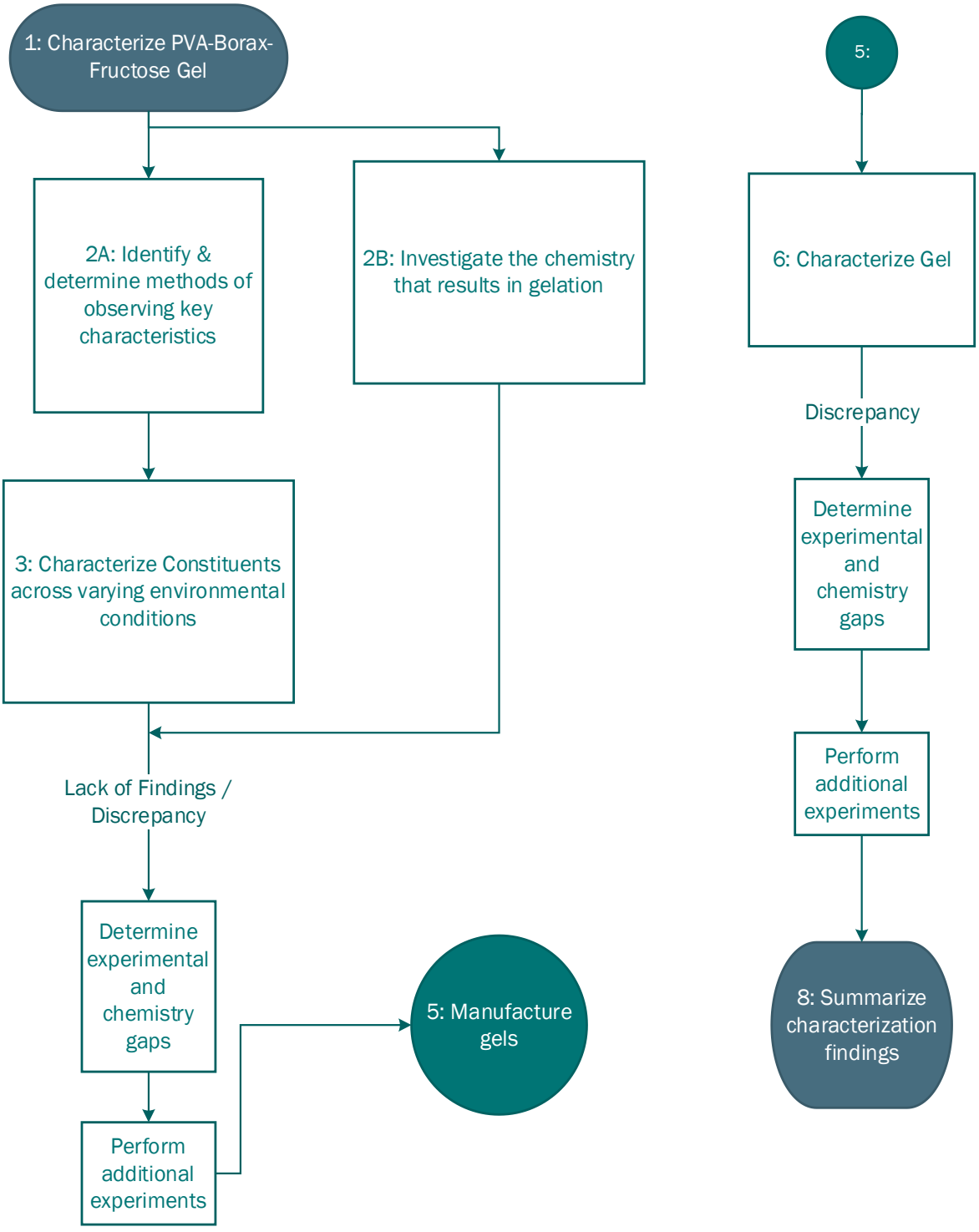

Figure 18: Flowchart detailing characterization.

From Figure 18, the first step was to identify key characteristics. The first characteristic identified for observations was density. Density is important for identity verification purposes, especially, when discussing concentrations, including w/w% and w/v%. When discussing varied concentrations of constituents, mass and volume measurements can be relatively easily obtained to verify the constituent at a particular concentration by comparing to results found in literature. Applications of the gel are varied, primarily as a function of viscosity and as such, the viscosity of the gel and gel constituents is the next identified key characteristic for observations.

In parallel to the identification of key characteristics, it was also important to determine how the individual constituents interact with one another, resulting in gelation (item #2B, depicted in Figure 18). The next step was to determine methods to observe key characteristics. These methods were then employed to make observations over a wide range of environmental conditions typically expected for the various applications of gels and gel constituents.

Given that one theory of borax-fructose crosslinking results in an increase of pH, compared to the other theory where this is not the result, the pH measurements of combined constituent solutions can be used to validate chemistry. Once the results of the characterization of gel constituents have been validated with chemistry and literature, gels of varied viscosities were then manufactured, as per flowchart element #5, indicated in Figure 18.

The gels were then characterized as per element #6 of the flowchart and the general results were validated with chemistry and literature. After characterization and validation of gels, the findings were summarized, meeting the objectives of the problem statement. Section 3, details the various materials used to manufacture the gel and gel constituents. Section 5.2 describes the various methodologies employed to manufacture individual gel constituents and gels. Sub-sections within Section 5.2 also detail the methods and equipment used to characterize gel constituents and gels such as density, pH, viscosity, and non-Newtonian characterizations.

5.2 Methods

To adequately characterize PVA-Borax-fructose gels and its constituents, methods of manufacturing the individual constituents, gels, and methods of characterizing the gel and gel constituents were determined. Table 1 details the various methods identified for manufacturing and characterizing the gel and its constituents:

Table 1: Various Methods Identified for the characterization of gels and gel constituents.

Method #:	Method Identified:	Shorthand Name:	Process Addressed from Flowchart in Figure 18:
0	Manufacturing of Constituent Solutions	MANE: CONST SOL	2A
1	Manufacturing of Fructose Solutions	MANE: FCTSE	2A
2	Manufacturing of Borax Solutions	MANE: BRX	2A
3	Manufacturing of Borax-fructose Solutions	MANE: FCTSE-BRX	2A
4	Manufacturing of PVA Solutions	MANE PVA	2A
5	Manufacturing of Gels	MANE: GEL	5
6	Characterization: Density	CHAR: DENS	2A, 3
7	Characterization: Rheology	CHAR: VISC	2A, 3
8	Characterization: Evaporation Rate	CHAR: EVAP	2A, 3
9	Characterization: Hydration State	CHAR: HYDRTE	2A, 3
10	Characterization: Rheology of Gels	CHAR: GEL	6

Methods detailing characterization of the individual constituents, and the gels, to obtain a fundamental understanding of behaviours, under a range of expected environments, is discussed within this section. Specific to Method #8 in Table 1, evaporation rate characterization is required to determine the viscosity as a function of solution evaporated. Method #9 in Table 1, is necessary to determine the hydration state of borax.

5.2.1 Method 0 - Manufacturing: Constituent Solutions

Constituent solutions were prepared by obtaining a beaker and placing it on a Delta Range PB3002-S weighing scale. The weighing scale was then tared, after which the mass equivalent of the concentration of the solution being manufactured is added into the beaker. The required mass equivalent of concentration is determined via the following equation:

$$Mass_{Constituent} = Volume_{Net\ Solution} * \frac{w}{v}\%_{Constituent} \quad \text{Equation 16}$$

Once the mass equivalent is added to the beaker, the required volume of reverse osmosis (RO) water is added to obtain the final mass of solution and constituent concentration needed. To manufacture gels and gel constituent solutions, a source of water, with minimal contaminants is required. The university reverse osmosis (RO) water purification system, accessed via a laboratory tap located from a 4th floor chemistry laboratory in the ERC (Energy Research Centre), belonging to Dr. Ikeda, was this source of water used. Water obtained from this tap was stored in batches of 500 mL plastic containers and was refilled periodically, once all the containers were depleted.

The beaker is then placed on a hot plate, equipped with a built-in magnetic stirrer. The magnetic stirrer is used either alone or in combination with heating from the hot plate. Temperatures of the hot plate is not allowed to exceed 333.15 ^{o}K to ensure adequate margin to prevent boiling or evaporation. After visually determining that complete dissolution has been achieved, the beaker is removed from the hot plate and allowed to cool to room temperature.

The mass of the solution is measured again to ensure RO water was not lost to evaporation; If mass is lost, the equivalent lost RO water mass is readded to the solution. Finally, a portion of the solution is obtained for characterization, and the rest is transferred into storage containers for further characterization or gel manufacturing purposes.

5.2.2 Method 1 – Manufacturing of Fructose Solutions

Varied concentrations of fructose solutions, including the concentration equivalent to the gel manufacturing, were prepared for characterization purposes. The mass of fructose required were determined via Equation 16. The concentrations of fructose solutions manufactured, as well as the mass equivalents, are detailed within Table 2:

Table 2: Concentration and Mass Equivalents of Fructose

Concentration (w/v %)	Mass Equivalent (g); Assuming 500 mL Sample Size
3.6	18
6.6	33
10.6	53
13.6	68
16.6	83

After determining the concentration mass equivalents, 500 mL solutions were prepared according to the method described in section 5.2.1.

5.2.3 Method 2 – Manufacturing of Borax Solutions

Varied concentrations of borax solutions were prepared for characterization purposes. The gel manufacturing procedure calls for 10 w/v% borax, however borax requires additional constituents to increase solubility (5 w/v%) [98]. From Table 3, solutions were prepared up to the solubility limit, as well as slightly over the solubility limit at a concentration of 7 w/v% to demonstrate precipitation effects. The mass of borax required were determined by Equation 16, in section 5.2.1. The concentrations of Borax solutions manufactured, as well as the mass equivalents, are specified in Table 3:

Table 3: Concentration and Mass Equivalents of Borax

Concentration (w/v %)	Mass Equivalent (g); Assuming 500 mL Sample Size
1	5
3	15
4	20
5	25
7	35

After determining the concentration mass equivalents, 500 mL solutions were prepared according to the method in section 5.2.1.

Heating (up to 3 on the dial or equivalent to 333.15 ºK) was required to accelerate the dissolution process. Once the solution was cooled to ambient room temperatures, it was confirmed that there is no precipitation prior to performing characterization studies.

5.2.4 Method 3 – Manufacturing of Borax-fructose Solutions

Varied concentrations of borax combined with fructose of concentration 13.6 w/v%, into borax-fructose solutions for characterization purposes. The mass equivalents of borax and fructose required for the varied solution concentrations (by w/v%) were determined using Equation 16, in section 5.2.1. It must be noted that the concentration of fructose was maintained at 13.6 w/v% throughout the manufacturing of all borax-fructose solutions. The concentrations of borax-fructose solutions manufactured, as well as the mass equivalents, are detailed within Table 4:

Table 4: Concentration and Mass Equivalents of Borax-fructose; Masses are added to the beaker before being filling up to 500 mL with water.

Concentration (w/v %)		Mass Equivalent (g)	
Fructose	Borax	Fructose	Borax
13.6	2	68	10
13.6	4	68	20
13.6	7	68	35
13.6	10	68	50
13.6	12	68	60

After determining the concentration mass equivalents, 500 mL solutions were prepared. In addition to the method described in section 5.2.1, one additional step was used. Specifically, once the borax and fructose in powdered forms are added to the beaker, the powders should be thoroughly mixed before the addition of any water to prevent caking of the borax constituent.

5.2.5 Method 4 – Manufacturing of PVA Solutions

Varied concentrations of PVA solutions were prepared for characterization purposes. The concentration of PVA solutions are specified in w/w%. The mass of PVA solutions required for the varied concentrations are determined according to Equation 17:

$$Mass_{PVA\ Solute} = Mass_{Net\ PVA\ Solution} * \frac{w}{w}\%_{PVA\ Constituent} \quad \text{Equation 17}$$

Based on Equation 17, the mass of PVA required are detailed in Table 5:

Table 5: Theoretical Concentration Mass Equivalents of PVA

Concentration (w/w %); PVA	Mass Equivalent (g)	Absolute Concentration of PVA; Assuming 500mL or 494.72g Net Sample Size (w/v % or g/dL & w/w%)	
16	079.16	$1.58\frac{w}{v} = 1.58\frac{g}{dL}$;	$1.6\frac{w}{w}\%$;
24	118.73	$2.37\frac{w}{v} = 2.37\frac{g}{dL}$;	$2.4\frac{w}{w}\%$;
28	138.52	$2.77\frac{w}{v} = 2.77\frac{g}{dL}$;	$2.8\frac{w}{w}\%$;
34	168.20	$3.36\frac{w}{v} = 3.36\frac{g}{dL}$;	$3.4\frac{w}{w}\%$;
44	217.68	$4.35\frac{w}{v} = 4.35\frac{g}{dL}$;	$4.4\frac{w}{w}\%$;

The PVA obtained from the manufacturer is a 10 w/w% aqueous solution. The manufacturer and the specifications of the PVA are detailed in section 3.1. The third column of Table 5 is a calculation of the absolute concentration of PVA after further dilution. This was calculated according to Equation 18 and Equation 19:

$$Absolute\ PVA\ Concentration_{\frac{g}{dL}} = \frac{Mass_{PVA\ Solute} * 10\%}{Mass_{Sample\ Size}}\frac{g}{dL} \quad \text{Equation 18}$$

$$Absolute\ PVA\ Concentration_{\frac{w}{w}\%} = \frac{Mass_{PVA\ Solute} * 10\%}{Mass_{Sample\ Size}}\frac{w}{w}\% \quad \text{Equation 19}$$

Regarding PVA solution preparation, rather than filling the beaker up to the 500 mL mark after the constituent mass equivalent is added, as described within the method in section 5.2.1, the scale is instead tared and the mass equivalent of RO water required to manufacture the intended specified constituent concentration in w/w% was added.

5.2.6 Method 5 – Manufacturing of PVA-Borax-fructose Gels

Once the borax-fructose solution was manufactured, a portion of the solution was obtained for the sol-gel process via constituent combination. First, the beaker is tared on a weighing scale. The required quantity of pre-manufactured PVA solution of specified concentration is added to the beaker. Another beaker is also tared on a separate weighing scale for the addition of the specified concentration of borax-fructose solution.

The original procedure called for 15 g of pre-manufactured borax-fructose solution of 13.6 w/v% fructose and 10 w/v% borax to be mixed with PVA solution. 22.5 g of PVA is then added to a separate beaker and mixed with 7.5 g of RO H_2O using a magnetic stirrer on a hot plate set to 45 ^oC. The PVA solution is then added to the 15 g of borax-fructose solution while thoroughly mixing.

The new procedure requires pre-manufactured borax-fructose solution of 13.6 w/v% Fructose and 10 w/v% borax to be added in a dropwise fashion into the PVA solution while thoroughly mixing to produce the gel. It is important that the PVA solution is added to the beaker first and then borax-fructose solution is added in a dropwise fashion afterwards. Inversion of this process as with the original procedure results in demixed gels. The concentration equivalents of constituents used to manufacture a 0.052 kg gel sample, including the quantity of borax-fructose solution added dropwise, are specified in Table 36 within the Appendix under section 11.3.1.

The table specifies concentrations and quantities to manufacture two types of gels. The relative concentration of PVA solution and borax-fructose solution for type I gels were 96.15 w/w% and 3.85 w/w% respectively. The relative concentration of PVA solution and borax-fructose solution for type II gels were 88.46 w/w% and 11.54 w/w% respectively. Five variations of type I and type II gels can be manufactured based on the absolute concentration of PVA solution from Table 5.

5.2.7 Method 6 – Characterization: Density

After gel constituents or gels have been manufactured, density is one of the first characterizations that is performed. Density characterization also serve as a relatively simple method for verifying the constituents and gels, are as expected; for example, simple changes, such as evaporation are reflected as changes in density.

To obtain density, a graduated cylinder is cleaned rinsed and thoroughly dried. After which, the mass of the graduated cylinder is obtained using a laboratory scale. The scale is tared while the empty graduated cylinder remains on the scale. A sample of the solution being characterized is obtained and poured into the graduated cylinder up to a known volumetric marking. The volumetric measurement indicated by the meniscus is then obtained. Next, the graduated cylinder is placed on the laboratory scale, and the mass is determined. After determining the mass, the density, ρ, is calculated according to the expression in Equation 20:

$$\rho = \frac{m}{v} \pm \omega_\rho \qquad \text{Equation 20}$$

The uncertainty associated with the density expression is described in sub section 5.2.7.1.

5.2.7.1 Uncertainty: Density Characterization

Density related uncertainty, ω_ρ, is calculated as per the expression in Equation 21:

$$\omega_\rho = \sqrt{(\frac{\partial \rho}{\partial m} * \omega_m)^2 + (\frac{\partial \rho}{\partial v} * \omega_v)^2} \qquad \text{Equation 21}$$

Wherein: $\frac{\partial \rho}{\partial m} = \frac{1}{v}$; $\frac{\partial \rho}{\partial v} = -\frac{m}{v^2}$; ω_m = ± 0.01g [128]; ω_v = ± 0.5 ml, given a 50 mL graduated cylinder was used for measurements. Therefore, density related uncertainty, ω_ρ, including equipment associated uncertainty can be expressed as per Equation 22:

$$\omega_\rho = \sqrt{\left(\frac{1}{v} * 0.01\right)^2 + \left(\frac{-m}{v^2} * 0.5\right)^2}$$ Equation 22

Given that the laboratory balance has an inherent uncertainty of ± 0.01g, and the graduated cylinder has an inherent uncertainty of ± 0.5 ml, this translates into an uncertainty on the order of ± 0.05 for density, as can be observed in Figure 36. An uncertainty of ± 0.05 for density is acceptable since variations as a function of constituent concentrations can be adequately observed with this level of uncertainty, as observable from Figure 36, Figure 42, Figure 45, and Figure 48.

5.2.8 Method 7 – Characterization: pH Measurement

The pH of the various solutions manufactured were obtained using an EXTECH Instruments-ExStik PH100 meter. The pH meter was calibrated using a pH 7 buffer solution. The pH meter requires calibration whenever it is retrieved from storage for pH measurements. To calibrate, the pH meter is turned on and the "CAL" button on the instrument is held while the probe of the pH meter is submerged within the buffer solution.

Once the pH meter has been turned on, the digital screen of the pH meter will indicate the pH of the buffer solution. The pH value will stop blinking and become a solid value once it has achieved calibration. The manual of the pH meter states that either, a two-point calibration (with a buffer of 7 and 10 or 7 and 4, whichever is closer to the pH of the sample), or a one-point calibration (with buffer solution closest to the pH of the sample solution) is valid. A one-point calibration was used for pH measurements for this work.

Once the pH meter has been calibrated, rinsed in RO water, and wiped it is ready for measurement of pH. To measure pH, dip the electrode bulb into the sample solution. While the bulb of the pH meter is immersed in the sample solution, the user must wait until the pH value has stabilized, indicated when the blinking digital interface becomes solid. The inherent uncertainty of the instrument, according to the user manual was reported to be ± 0.01 pH, with a pH measuring range from a pH of 0 to 14. The pH meter also provides temperature readings for the pH measurement. The temperature readings were reported to have an uncertainty of 1 °C according to the user manual.

5.2.9 Method 8 – Characterization: Evaporation

Constituent/gel solution evaporation observations allows for the determination of various phenomenon; including the rate of evaporation as a function of viscosity (or PVA concentration, which is directly related to viscosity), especially that of PVA solutions and gels as the viscosities of these substances vary dramatically as a function of evaporation.

Equipment requirements for evaporation observations are a 50 mL graduated cylinder, laboratory scale, Buchner flask, a pump, a rotameter as well as a variac for pump control. A schematic of the setup is depicted in Figure 19. The graduated cylinder and the laboratory scale allow for density observations before and after evaporation. A sample less than 50 mL of constituent or gel is obtained and poured into the graduated cylinder up to a known volumetric marking and then weighed for density and viscosity observation. The contents of graduated cylinder is then poured into a 125 mL Buchner flask. The Buchner flask is then attached to the rest of the system via plastic tubing.

Once the Buchner flask is attached to the system, the pump depicted in Figure 19 is then used to suction air, firstly through the rotameter. The air is then directed from the outlet of the rotameter via plastic tubing to glass tubing at the entrance of the Buchner flask, where the air interacts with the sample fluid over a pre-determined time, allowing for bubbling to occur. The bubbling causes solution molecules to temporarily be at the solution surface where intermolecular attractive forces that hold the solution together are reduced allowing for molecules to enter the vapor phase [129]. Air flow then continues to be suctioned from the outlet of the Buchner flask through the pump and is finally vented to atmosphere. The remaining solution after bubbling for a pre-determined amount of time, is then characterized for density and viscosity.

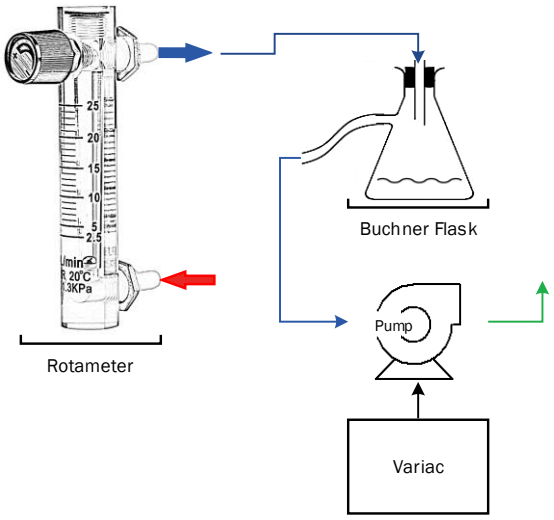

Figure 19: Schematic - Evaporation Rate Characterization; Red Arrow Indicates air flow entrance, green arrow indicates airflow exit, blue arrows indicate direction of air flow between components of system.

5.2.10 Method 9 – Characterization: Hydration State

The hydration state of borax can vary depending on the environmental conditions of storage and transportation; hence, the verification of the hydration is important to ensure materials being used for the manufacturing of the gels are as expected to ensure repeatability.

The hydrated state of borax can be determined through thermogravimetric analysis. This was achieved by using a STA 449 F1 Jupiter TGA with a silicone carbide furnace, which will provide mass and temperature readings at each time step through integrated thermocouples and a weighing balance. The mass and temperature readings are used as part of the calculation of the state of hydration. A schematic of the system is depicted in Figure 20.

The thermogravimetric analyzer (TGA) has a heating range between 25 – 1500 °C, with a manufacturer suggested heating rate range between 10-20 $\frac{K}{min}$. Prior to inserting samples into the TGA, a number of preparatory steps have to be performed first:

1. Ensure Argon gas is available for use as a purge/cover gas.
2. Switch on the thermostat 3 hours, and the computer system 1 hour, before performing the analysis. (TGA is usually left turned on constantly).
3. Wear latex gloves, dust mask and goggles before handling the TGA and the borax.
4. Select the appropriate crucible (Alumina Type has been selected for use with borax as no interaction with borax should occur).
5. Clean the crucible and lid with ethanol or acetone, and wash with deionized water. Dry the crucible and heat it to the final working temperature.
6. Perform baselining using empty crucibles as per the TGA manual.

A small sample of borax, of 772.25 ± 0.01 mg was then transferred into the TGA crucible, as pictured in Figure 21. The Alumina type crucible was then placed onto the thermocouple stand of the TGA, as depicted in Figure 22. After which, the oven was closed, and the software was used to combine the sample measurement with the correction measurement (obtained from the baselining). The heating rate of 15 $\frac{^oK}{min}$, maximum temperature of 573.15 °K and temperature hold time of 1.5 hours are input into the software. Before starting the analysis, it must be ensured that the instrument is setup for dynamic purging. The thermogravimetric analyzer is then turned on and ramps up to the temperature setpoint input by the user. After completion of the experiment, the data was remotely accessed for analysis.

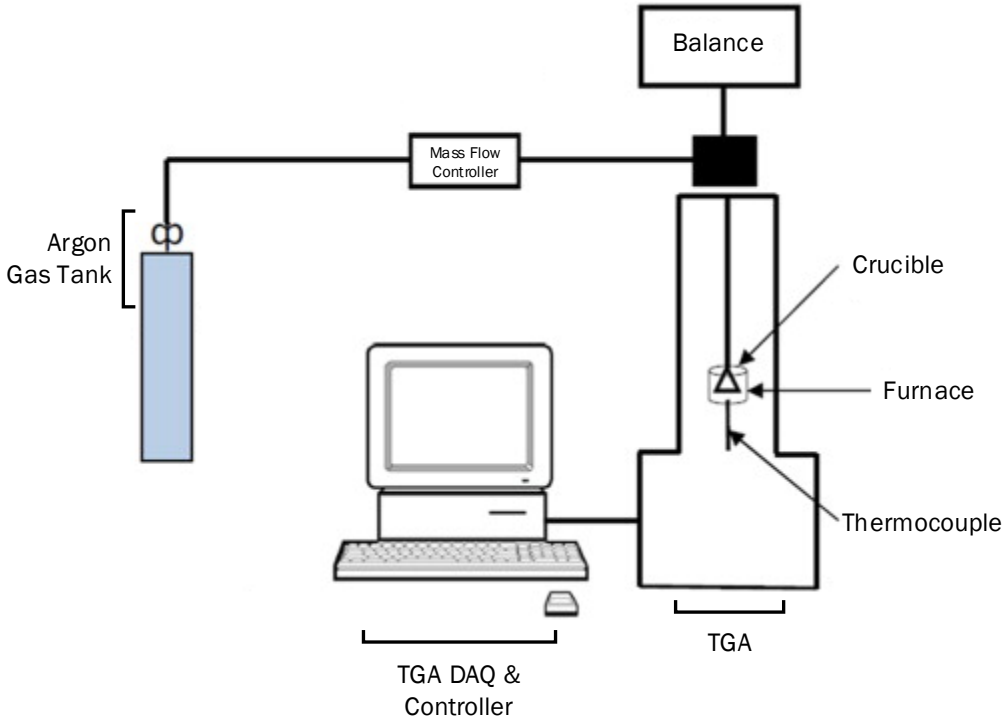

Figure 20: Schematic - Thermogravimetric Analyzer

Figure 21: Sample for the TGA experiment that was transferred into the crucible

Figure 22: Crucible Placement onto the thermocouple stand of the TGA

The borax constituent of the hydrated borax should not be effected by the sample temperatures it is exposed to by the TGA [130]; given such a case, the time rate dependent parameters [130] such as activation energy and frequency factor can be calculated using the Coats and Redfern method [103] of interpreting the Arrhenius equation.

The rate of the fraction of A (of the physical reaction of the form $aA \rightarrow bB_{(s)} + cC_{(g)}$) of the borax sample that has disappeared over a period of time, is expressed as follows [103]:

$$\frac{d\alpha}{dt} = k(1-\alpha)^n \qquad \text{Equation 23}$$

Where α is the fraction of A decomposed at time, t. k and n are the rate constant and the order of the reaction, respectively. The linear heating rate of β is described by Equation 24 [103]:

$$\beta = dT/dt \qquad \text{Equation 24}$$

Where T is the temperature in Kelvins. The rate constant k is described by Equation 25, which is of an Arrhenius type [103]:

$$k = k_0 e^{-\frac{E_a}{RT}} \qquad \text{Equation 25}$$

Where k_0 is the frequency factor E_a and R are the activation energy and gas constant, respectively. Coats and Redfern combined expressions in Equation 23, Equation 24 and Equation 25, and integrated, to obtain the following expression for Y, the initial state of hydration [103, 131]:

$$Y = \ln\left[\frac{1-(1-x)^{1-n}}{T^2(1-n)}\right] = \ln\frac{k_0 R}{\beta E_a} - \frac{E_a}{RT};\ For\ n\ \neq 1: \qquad \text{Equation 26}$$

Where, x is the amount of water evaporated. Units for the variables of the expressions in Equation 23, Equation 24 and Equation 25, are detailed in the Appendi, under section 11.4.2.

Plotting the left-hand side (LHS) of Equation 26, against 1/T, distinct lines that are indicative of different phases of transitions can be obtained. The transitions and the lack thereof, of the various slopes and intercepts of the lines are indicative of the various states of hydrations, and can then be used to solve for activation energies and frequency factors as per the following [131]:

Activation Energy: (m is the slope)

$$m = \frac{E_a}{R}; E_a = m * R \qquad \text{Equation 27}$$

Frequency Factor: b is the y intercept of the linear line of best fit)

$$\ln(\frac{k_0 R}{\beta E}) = b; k_0 = \frac{e^b * \beta E}{R} \qquad \text{Equation 28}$$

5.2.11 Method 10 – Characterization: Rheology of Gels

The viscosity of polymers such as PVA are dependent on properties/characteristics such as loss modulus, elastic modulus, [86] damping coefficient [132] and glass transition temperatures [133]. Although these characteristics must be determined experimentally through dynamic mechanical analysis, the characteristic change due to modification to the environment (such as temperature or even shear stress variation) are reflected as changes in viscosity. Storage and loss modulus are directly related to complex viscosity according to the following expression [85, 86]:

$$\eta(\dot{\gamma}) = |\eta^*(\omega_f)| = |\frac{G^*}{\omega_f}| = \left|\frac{(G' + G'')}{\omega_f}\right| \qquad \text{Equation 29}$$

where, $G^*$is the dynamic modulus, the sum of storage (G') and loss modulus (G''). ω_f is the angular frequency at which the measurements are obtained. Dynamic modulus describes the loosening or tightening of the polymer structure [134] which allows for an increased or reduced degree of movement of the smaller polymer chain segments. It must be noted however that the magnitude of the complex viscosity is equivalent to viscosity under continuous shear stress, only given that the

continuous shear rate is equivalent to sinusoidal frequency (or in other words, the complex viscosity observed over one cycle per second) [135].

Kinematic and dynamic viscosity can be determined experimentally. The viscosity measurements for purposes of this thesis, are obtained using a concentric Searle type viscometer, specifically, a "Fungilab Smart Series One" [136]. Concentric Searle type viscometers use the relationship between shear stress, shear rate to determine dynamic viscosity. Shear stress and shear rate are measurements provided by the instrument. The Fungilab viscometer rotates a spindle at a constant speed resulting in a viscosity determined under a continuous shear rate along its axis while submerged in the sample fluid of interest. The cylinder containing the sample fluid remains stationary. The torque applied by the viscometer motor is related to shear stress (τ), according to Equation 30 [137]:

$$\tau = \frac{T}{2\pi R_s^2 L} \qquad \text{Equation 30}$$

The shear rate (γ), experienced by the viscometer spring, and the relationship between shear rate and the rotational speed of the viscometer (ω), is expressed according to Equation 31 [137]:

$$\gamma(x) = \frac{2\omega R_c^2 R_s^2}{x^2(R_c^2 - R_s^2)} \qquad \text{Equation 31}$$

Nomenclature section 11.4.3 provides the units of the variables torque (T), spindle length (L), cylinder radius (R_c), spindle radius (R_b) and x, the distance between the rotational axis and the layer of liquid at which the measurement is taken. Shear stress and shear rate are in turn related to dynamic viscosity (μ), by [137]:

$$\mu = \frac{\tau}{\gamma} \qquad \text{Equation 32}$$

Prior to operating the viscometer, certain factors that effect measurements obtained using the viscometer must be considered. According to the manual, viscosity measurements are only valid when the % EOS is in the range 15-95%. If the % EOS is outside of this range then different settings for rotational speed and spindle type are required to bring it within optimal range. The

viscometer is capable of varied spindle speed up to 100 rotations per min (RPM) for a viscosity range between 9 – 60 mPa·s using the L1 spindle; and up to 100 RPM for a viscosity range between 1 – 6 mPa·s using the LCP spindle [136].

Other factors to keep in mind include the combination of high rotational speeds and low viscosity fluids ands spindle to fluid container radii ratios. High rotational speeds combined with low viscosity fluids could result in turbulent flow Taylor vortices conditions [137]. Furthermore, it must also be noted that when the container radius to spindle radius ratio is greater than $\frac{R_e}{R_i} = 1.0847$ (as per the narrow gap concentric cylinder definition, according to ISO 3219 [137, 138]), this could result in secondary flow effects and inhomogeneous deformation [137]. Contrary to the phenomenon of large gaps resulting in secondary flow effects, the viscometer manual specifies that containers used to hold samples must be larger than or equivalent to 83 mm [136] otherwise resulting in artificially higher viscosity values, due to wall effects. The manual also specifies that the uncertainty associated with any rheological measurement has a maximum error of 1%, however this is only valid under conditions where the container is at least 83 mm in diameter or greater [136].

Instructions pertaining to the operation of the viscometer itself are found in the viscometer procedure within section 11.3.4 of the Appendix and includes instructions on the operation of additional plug-in equipment such as the low sample container and the thermostatic bath; both of which are required for temperature-controlled observations of viscosity. For viscosity observations with large sample sizes, the viscometer setup is depicted in the schematic in Figure 23. A beaker with an inner radius of 83 mm or greater (typically 500 mL beakers are of this size), as per the viscometer manual [136] is used. It must be noted that large sample sizes must be in the 475 mL – 485 mL range, such that the LCP spindle is fully submerged, (as required per the viscometer manual [136]). Furthermore, when observing the viscosity of large samples, it must be noted that the use of a centering gauge is required. The centering gauge is placed onto the laboratory scissor jack (depicted in the schematic in Figure 23) prior to placing the beaker. The centering gauge (with 5 mm increments) is used to centre the beaker relative to the spindle, as depicted in Figure 24:

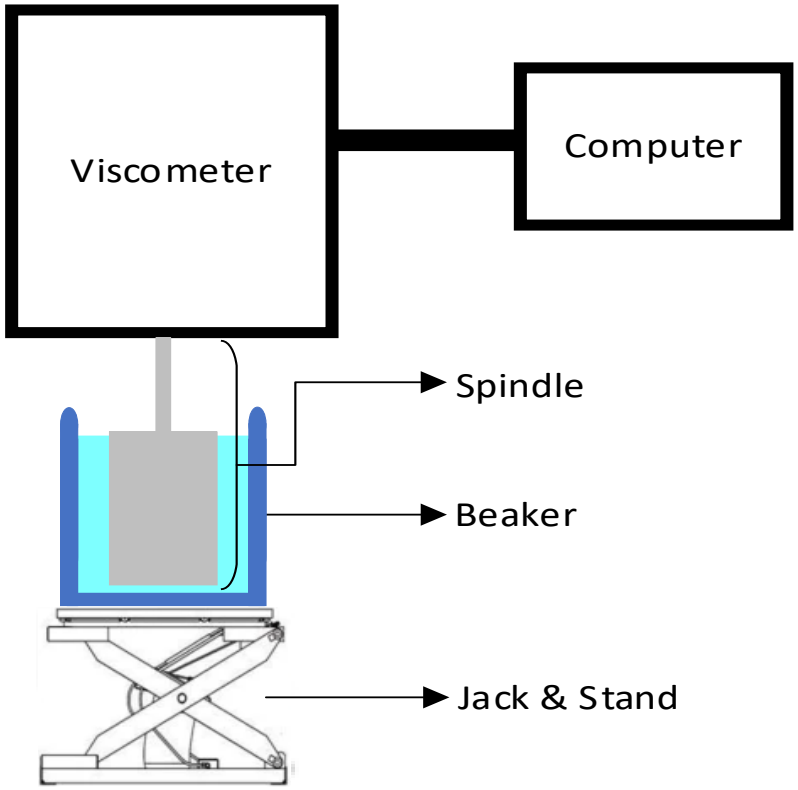

Figure 23: Schematic - Viscometer Setup for Large Sample Observations.

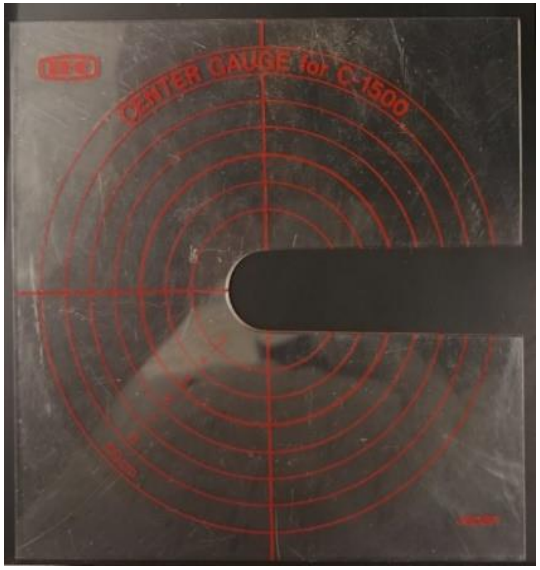

(A): Centering Gauge used to centre the beaker holding the liquid sample relative to the spindle

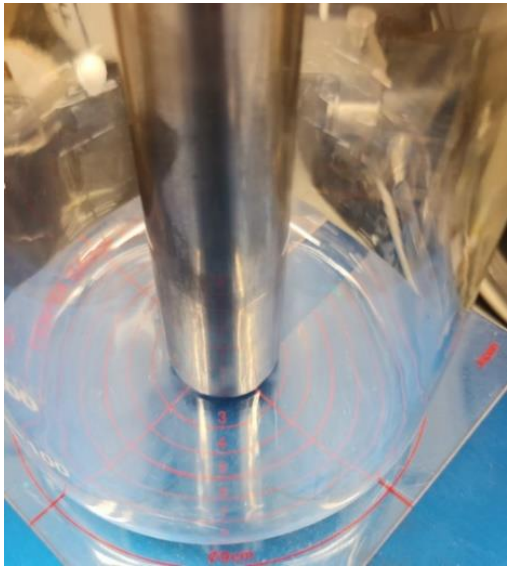

(B): Spindle and Beaker, centred relative to one another using the centering gauge, placed between the beaker and the scissor jack; View 1

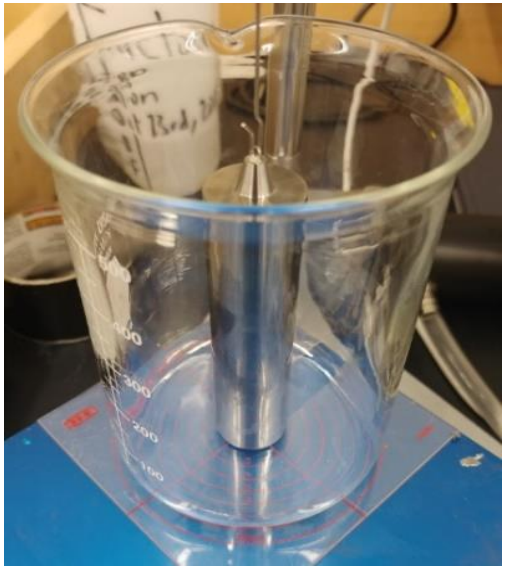

(C): Spindle and Beaker Centred relative to one another using the centering gauge, placed between the beaker and the scissor jack; View 2

Figure 24: Centering of spindle relative to beaker using a centering gauge

For thermal hysteresis or small sample rheological observations (sample size ≤ 16 mL), the viscometer must be used in conjunction with the thermal jacket, small sample container, and the thermostatic bath, as per the schematic depicted in Figure 25. The small sample container depicted in Figure 25 is 14 mm wide. Tap water can be used as the reservoir fluid for temperatures up to 353.15 °K. Higher temperature setpoints would require the use of fluids with higher boiling points.

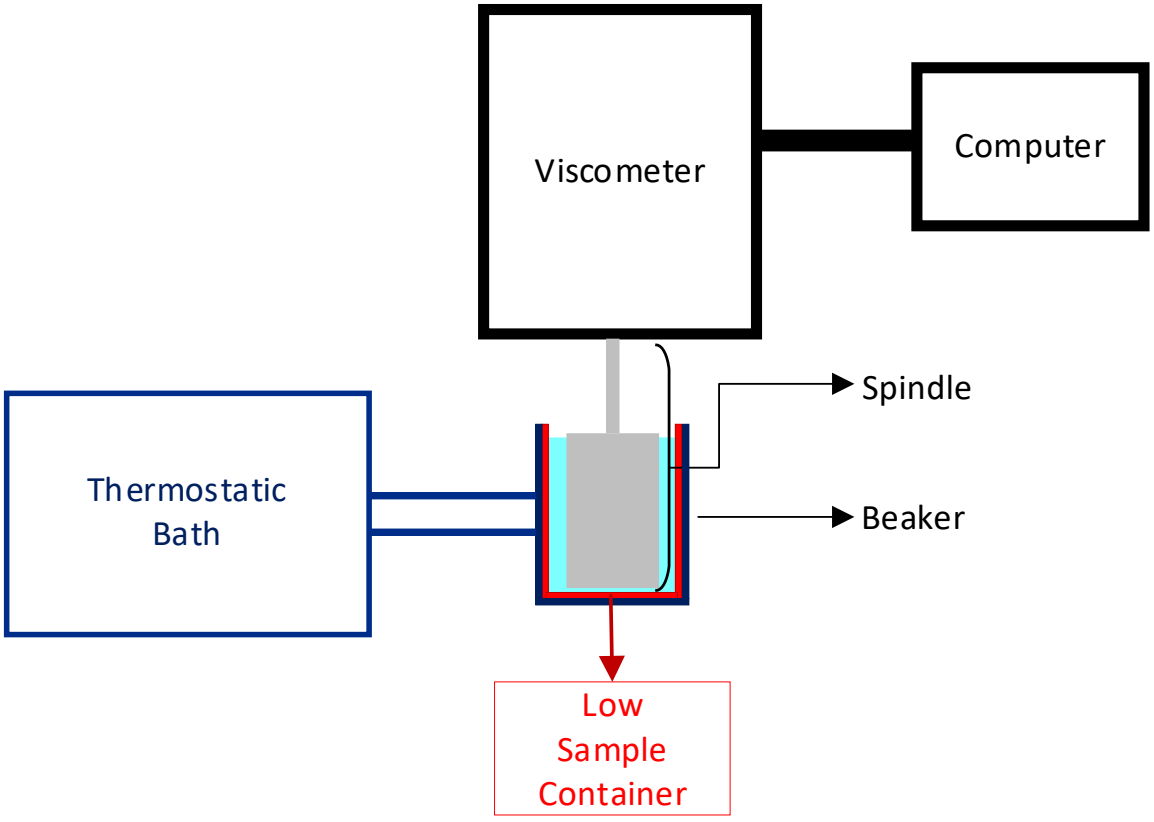

Figure 25: Schematic - Viscometer Setup for small samples or thermal hysteresis observations

It must be noted that once measurements are obtained from the viscometer, the first 100-200 seconds are omitted. This is because the viscometer requires some time to self calibrate, as can be seen from the large variation in viscosity in Figure 26. The time required is dependant on the viscosity of the fluid, with more viscous fluids requiring more time.

Figure 26 shows the viscosity measurement obtained for 3.36 $\frac{g}{dL}$ PVA solution at an RPM of 12 and a shear rate of 14.676 $\frac{1}{s}$. Once the calibration data has been omitted, the remainder of the dataset is averaged to obtain a steady state viscosity, at a constant temperature and shear rate.

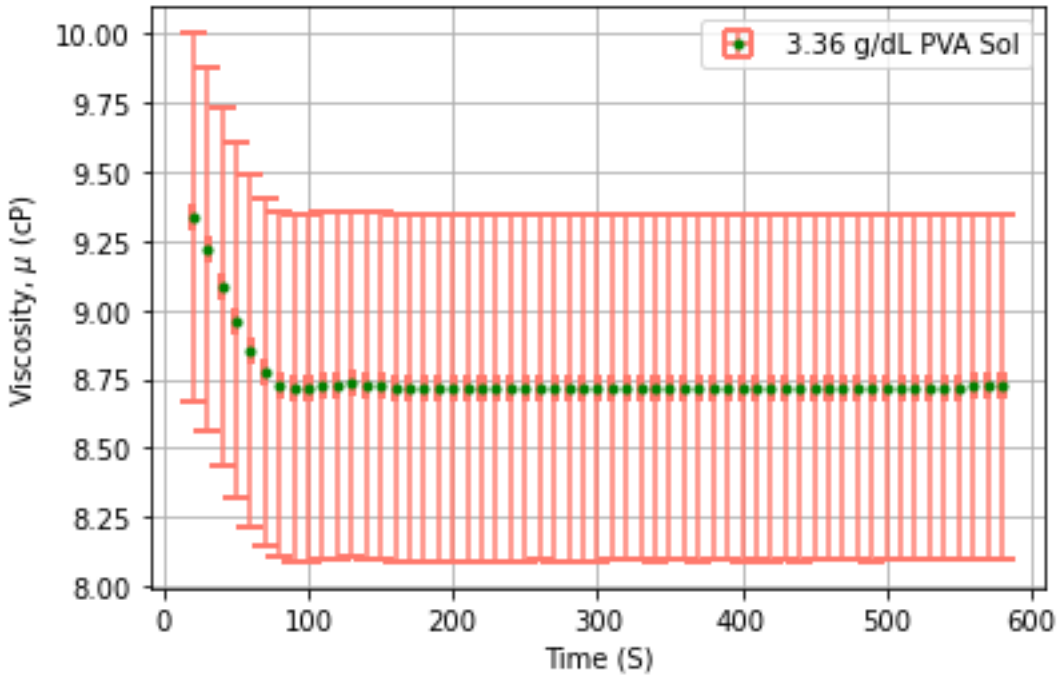

Figure 26: Sample dataset of raw viscosity data including measurements obtained during the viscometer self calibration phase.

5.2.11.1 Characterization: Rheology – Wall Effects

With regards to viscosity measurements of large quantity samples, inadequate centering of the container holding the sample can result in abnormally high viscosity readings. An experiment was conducted to confirm that wall effects were not biasing viscosity results. In this experiment readings were obtained closer to the edge of the beaker, as depicted in Figure 27.

Wall effects were eliminated by centering the beaker relative to the spindle using the centering gauge with 5 mm increments and an uncertainty of 2.5 mm allows for the 41.5 mm radius from the centre of the spindle to the inner wall of the beaker, (or a minimum container diameter of 83 mm [136]) which is required to avoid wall effects, to be ensured. Given the inner diameter of the beaker is 86 mm, even with a centering uncertainty of ± 2.5mm, the minimum 83 mm can still be maintained [136].

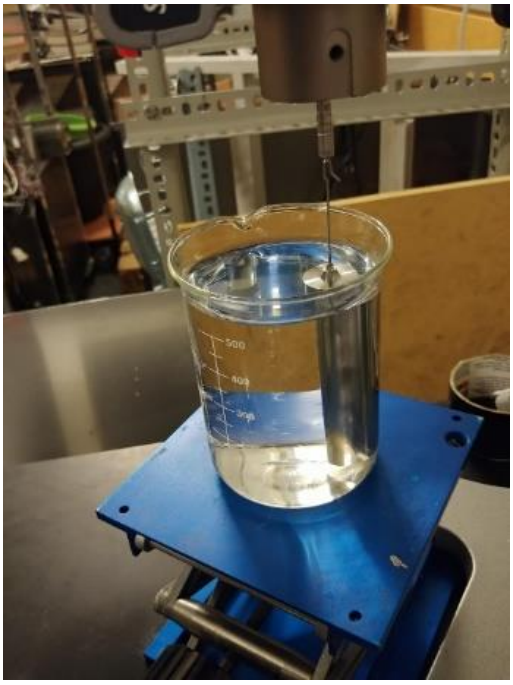

Figure 27: Wall effects on Viscosity Reading; At Edge

5.2.11.2 Characterization: Rheology – Low Sample Container

The viscometer requires that a container of 83 mm or greater be used to hold samples during measurements. The viscometer does not self calibrate to account for wall effects when the low sample container (LSC) is used. As such, a correction factor correlation needed to be developed for the LSC. This correlation is used to convert the viscosities that are obtained when the LSC is used, into viscosities equivalent to when a container that is 83 mm is used to hold samples. Further details pertaining to the correction factor correlation are provided within the Appendix under section 11.3.2.

This correlation must be used whenever the LSC is used to hold the sample during viscometer measurements. Specific instances in this work include thermal hysteresis experiments, non-Newtonian experiments, as well as any experiments that require steady state temperature observations besides room temperature. The LSC is required for any temperature related measurements because it is coupled to a thermal jacket and was designed by the manufacturer to be compatible with the thermostatic bath system.

5.2.11.3 Uncertainty: Viscosity

Since uncertainty associated with the low sample container based viscosity cannot be assumed to be 1% due to the wall effects induced high viscosity values [136], the uncertainty after converting these values into beaker equivalent values using the correlation, compounded with the uncertainty of the correlation (uncertainties associated with the coefficients of the equation used for curve fitting) needs to be calculated. The methodology used to calculate the uncertainty of the viscosity using a beaker, as well as the uncertainty obtained using the LSC are discussed within this section.

5.2.11.3.1 Beaker for Large Sample

The viscometer spindle is rotated at a constant speed in the sample fluid; the torque applied by the viscometer is related to shear stress, as described by Equation 30. The uncertainty of shear

stress (ω_τ) is a function of uncertainties of all the associated variables in Equation 30, including, torque, spindle radius and spindle length; and is equal to the root sum of the squares of the contributions of associated variables (given by partial derivate of shear stress with respect to the associated variable, multiplied by the uncertainty of the variable), as shown in Equation 33.

$$\omega_\tau = \sqrt{\left(\frac{\partial \tau}{\partial T} * \omega_T\right)^2 + \left(\frac{\partial \tau}{\partial R_s} * \omega_{R_s}\right)^2 + \left(\frac{\partial \tau}{\partial L} * \omega_L\right)^2} \quad \text{Equation 33}$$

Where, the partial derivative of shear stress with respect to Torque is shown in Equation 34.

$$\frac{\partial \tau}{\partial T} = \frac{1}{2\pi R_s^2 L} \quad \text{Equation 34}$$

The partial derivative of shear stress with respect to spindle radius is shown in Equation 35.

$$\frac{\partial \tau}{\partial R_s} = -\frac{T}{\pi R_s^3 L} \quad \text{Equation 35}$$

And the partial derivative of shear stress with respect to spindle length, is shown in Equation 36.

$$\frac{\partial \tau}{\partial L} = -\frac{T}{2\pi R_s^2 L^2} \quad \text{Equation 36}$$

Rotational speed is related to shear rate, according to Equation 31, where the uncertainty of shear rate (ω_γ) is a function of uncertainties of all the associated variables and is equal to the root sum of the squares of the contributions of associated variables (given by partial derivate of shear rate with respect to the associated variable, multiplied by the uncertainty of the variable), as shown in Equation 37.

$$\omega_\gamma = \sqrt{\left(\frac{\partial \gamma}{\partial \omega} * \omega_\omega\right)^2 + \left(\frac{\partial \gamma}{\partial x} * \omega_x\right)^2 + \left(\frac{\partial \gamma}{\partial R_c} * \omega_{R_c}\right)^2 + \left(\frac{\partial \gamma}{\partial R_s} * \omega_{R_s}\right)^2} \quad \text{Equation 37}$$

Where the partial derivative of shear rate with respect to angular velocity is shown in Equation 38.

$$\frac{\partial \gamma}{\partial \omega} = \frac{2R_c^2 R_s^2}{x^2(R_c^2 - R_s^2)} \quad \text{Equation 38}$$

The partial derivative of shear rate with respect to gaussian maximum distance, x, is shown in Equation 39.

$$\frac{\partial \gamma}{\partial x} = -\frac{4\omega R_c^2 R_s^2}{x^3(R_c^2 - R_s^2)} \quad \text{Equation 39}$$

The partial derivative of shear rate with respect to container radius is shown in Equation 40.

$$\frac{\partial \gamma}{\partial R_c} = -\frac{4\omega R_c R_s^4}{x^2(R_c^2 - R_s^2)^2} \quad \text{Equation 40}$$

And the partial derivative of shear rate with respect to spindle radius is shown in Equation 41.

$$\frac{\partial \gamma}{\partial R_s} = \frac{4\omega R_c^4 R_s}{x^2(R_c^2 - R_s^2)^2} \quad \text{Equation 41}$$

Lastly, the uncertainty of the dynamic viscosity (ω_μ) is a function of uncertainties of shear stress and shear rate and is equal to the root sum of the squares of the contributions of associated variables, as shown in Equation 42.

$$\omega_\mu = \sqrt{(\frac{\partial \mu}{\partial \tau} * \omega_\tau)^2 + (\frac{\partial \mu}{\partial \gamma} * \omega_\gamma)^2} \quad \text{Equation 42}$$

In order to verify the uncertainty of dynamic viscosity measurements given by the viscometer, as well as the respective uncertainties of shear stress and shear rate (which aren't provided for, by the viscometer or the viscometer manual), shear rate, as well as shear stress, including their respective uncertainties were calculated using the python code. Calculations were performed based on the knowns (such as beaker, low sample container and spindle measurements), given in Table 6:

Table 6: Measured parameters of container and spindle radius/length, required for uncertainty calculations.

Parameter Type	Parameter (mm)	Uncertainty (mm)
Beaker Radius	41.5	0.1
Low Sample Container Radius	32.5	0.1
Spindle Radius	12.5	0.1
Spindle Length	90	0.1

Referring to Equation 31, calculating the uncertainty requires knowledge of an unknown, specifically, x, the gaussian maximum distance (the distance between rotational axis and the layer of liquid at which the measurements are taken). A method to determine how to obtain x is not provided in the manual nor is it one of the viscometer data outputs. The gaussian maximum distance, x, is calculated by isolating for x (from Equation 31), and then substituting known container radius and spindle radius values, as per Equation 43:

$$x = \sqrt{\frac{2\omega R_c^2 R_s^2}{\gamma(R_c^2 - R_s^2)}} \qquad \text{Equation 43}$$

It must also be noted that when the container is swapped from a beaker to the "LSC", the gaussian maximum distance, x, will change as a function of container radius change. RPM and shear rate parameters are obtained from the viscometer output dataset post experimentation.

Similar to the gaussian maximum distance, x, torque (T), is also an unknown variable and is associated with shear rate. After isolating torque, the known parameters, specifically, spindle length and radius quantities can be substituted into Equation 44:

$$T = \tau * (2\pi R_s^2 L) \qquad \text{Equation 44}$$

Shear stress is a known and is output as a viscometer parameter. These knowns are then used to calculate torque, which in turn is necessary to determine the uncertainty associated with shear stress.

The uncertainty of shear stress (Equation 33) and shear rate (Equation 37) was used to calculate the viscosity uncertainty using Equation 42. This uncertainty was found to vary between ± 0.002 to ± 0.6, depending on the diameter of the sample container used (beaker diameter or low sample container diameter), the viscosity of the fluid and the RPM of the spindle.

5.2.11.3.2 Low Sample Container

The viscosity manual only states an uncertainty of 1% for all measurements obtained when the fluid container is equal to or greater than 83 mm [136], and does not provide uncertainty percentages for when the fluid container is swapped to the low sample type container which is necessary for temperature controlled rheological measurements. The python curve fitting function detailed in section 11.3.3 determines the coefficients of the equation that best correlates LSC viscosity to beaker viscosity values. The correlation in Equation 75 (section 11.3.2) , complete with coefficients solved using the curve fitting function, is then used to solve for y, the beaker equivalent values (by substituting values for x, the viscometer output obtained using the LSC). The uncertainty associated with the correction factor function in Equation 75, specifically for the coefficients must also be calculated for and compounded to the error. Equation 45 details how the compounded uncertainty of the correction factor function is calculated:

$$\omega_y = \sqrt{\left(\frac{\partial y}{\partial x} * \omega_x\right)^2 + \left(\frac{\partial y}{\partial a} * \omega_a\right)^2 + \left(\frac{\partial y}{\partial b} * \omega_b\right)^2 + \left(\frac{\partial y}{\partial c} * \omega_c\right)^2 + \left(\frac{\partial y}{\partial d} * \omega_d\right)^2} \quad \text{Equation 45}$$

Where, the partial derivative of the correction factor function y, with respect to LSC viscosity, x, from Equation 75 is shown in Equation 46.

$$\frac{\partial y}{\partial x} = 3ax^2 + 2bx + c \quad \text{Equation 46}$$

The partial derivative of the correction factor function y, with respect to coefficient, a, is shown in Equation 47.

$$\frac{\partial y}{\partial a} = x^3 \qquad \text{Equation 47}$$

The partial derivative of the correction factor function y, with respect to coefficient, b, is shown in Equation 48.

$$\frac{\partial y}{\partial b} = x^2 \qquad \text{Equation 48}$$

And the partial derivative of the correction factor function y, with respect to coefficient, c, is shown in Equation 49.

$$\frac{\partial y}{\partial c} = x \qquad \text{Equation 49}$$

Partial derivative of the correction factor function y, with respect to coefficient, d, is shown in Equation 50.

$$\frac{\partial y}{\partial d} = 1 \qquad \text{Equation 50}$$

The python code is used to plot the LSC viscosities that are converted into beaker equivalent using the correction factor function along with the compounded uncertainty.

5.2.12 Characterization: Rheology – Thermal Hysteresis

Temperatures can be varied at any point during viscosity observations by adjusting the thermal setpoint of the thermostatic bath user interface. The maximum temperature of thermal hysteresis experiment, and various intermediary temperatures can be investigated. The thermostatic bath can be used between 299.15-348.15 ^{o}K using H_2O as the reservoir fluid.

The thermostatic controller cannot be used to cool, so the reservoir was emptied while adding room temperature water to observe temperatures in a decreasing fashion. The thermostatic bath maintained the temperature at the lowered setpoint.

The equations of the trendlines used to describe the apparent viscosity as a function of temperature (section 7.1.2.1) were developed using python code. Specifically, the SciPy optimize.curve_fit function, which uses non-linear least squares to fit a function to any data.

5.2.13 Characterization Experiment Matrices

Table 7 is a matrix for the various experiments performed for density and viscosity characterizations of constituents and constituent combinations. Table 7 consists of test cases for both density and viscosity characteristics, since density and viscosity were measured in tandem. Table 8 is a matrix of the pH, non-Newtonian, and borax hydration state experiments that were performed.

Table 7: Characterization Experiment Matrix – Experiment Types = Density; Viscosity; Batch Counter = BC

Test Case Identifier: Density	Test Case Identifier: Viscosity	Constituent	Concentration (w/v%)	RO Water Batch Used:
Refer to Table 10	**Refer to Table 10**	Water	N/A	N/A
D-2A-I	**V-2A-I**	Borax	1	WTR-BC-1
D-2B-I	**V-2B-I**	Borax	3	WTR-BC-2
D-2B-II	**V-2B-II**	Borax	3	WTR-BC-2
D-2C-I	**V-2C-I**	Borax	4	WTR-BC-3
D-2D-I	**V-2D-I**	Borax	5	WTR-BC-4
D-3A-I	**V-3A-I**	Fructose	3.6	WTR-BC-5
D-3B-I	**V-3B-I**	Fructose	6.6	WTR-BC-5
D-3C-I	**V-3C-I**	Fructose	10.6	WTR-BC-6
D-3C-II	**V-3C-II**	Fructose	10.6	WTR-BC-7
D-3D-I	**V-3D-I**	Fructose	13.6	WTR-BC-6
D-3D-II	**V-3D-II**	Fructose	13.6	WTR-BC-7
D-3E-I	**V-3E-I**	Fructose	14.6	WTR-BC-6
D-3E-II	**V-3E-II**	Fructose	14.6	WTR-BC-7
D-3F-I	**V-3F-I**	Fructose	16.6	WTR-BC-6
D-4A	**V-4A**	Borax-fructose	02-13.6	WTR-BC-8
D-4B	**V-4B**	Borax-fructose	04-13.6	WTR-BC-8
D-4C	**V-4C**	Borax-fructose	07-13.6	WTR-BC-8
D-4D	**V-4D**	Borax-fructose	10-13.6	WTR-BC-8
D-4E	**V-4E**	Borax-fructose	12-13.6	WTR-BC-9
D-5A	**V-5A**	PVA Solution	1.58	WTR-BC-10
D-5B	**V-5B**	PVA Solution	2.37	WTR-BC-10
D-5C	**V-5C**	PVA Solution	3.36	WTR-BC-10
D-5D	**V-5D**	PVA Solution	4.35	WTR-BC-10

Table 8: Characterization Experiment Matrix – Experiment Types = pH, Non-Newtonian, and Hydration State

Test Case Identifier	Characterization Experiment Type	Constituent	Concentration (w/v%)	RO Water Batch Used:
pH-1A-I	pH	Borax	1	WTR-BC-1
pH-1B-II	pH	Borax	3	WTR-BC-2
pH-1C-I	pH	Borax	5	WTR-BC-4
pH-2A-I	pH	Fructose	3.6	WTR-BC-5
pH-2B-I	pH	Fructose	6.6	WTR-BC-5
pH-2C-I	pH	Fructose	10.6	WTR-BC-6
pH-2D-I	pH	Fructose	14.6	WTR-BC-7
pH-2E-I	pH	Fructose	16.6	WTR-BC-6
pH-3A	pH	Borax-fructose	02-13.6	WTR-BC-8
pH-3B	pH	Borax-fructose	04-13.6	WTR-BC-8
pH-3C	pH	Borax-fructose	07-13.6	WTR-BC-8
pH-3D	pH	Borax-fructose	10-13.6	WTR-BC-8
pH-4A	pH	PVA Solution	1.58	WTR-BC-10
pH-4B	pH	PVA Solution	3.36	WTR-BC-10
pH-4C	pH	PVA Solution	4.35	WTR-BC-10
NN-1A	Non-Newtonian	PVA Solution	1.58	WTR-BC-10
NN-1B	Non-Newtonian	PVA Solution	3.36	WTR-BC-10
NN-1C	Non-Newtonian	PVA Solution	4.35	WTR-BC-10
HS-1	Hydration State	Borax Powder	N/A	N/A
SL-1	Solubility Limit	Borax Solution	7	WTR-BC-4

Table 9 is a matrix of the various evaporation and thermal hysteresis characterization tests performed. The "Relevant Parameter" column identifies the parameters unique to the specific test case.

Table 9: Evaporation and Thermal Hysteresis Characterization Experiment Matrix; Note: The "Relevant Parameter" column details parameters unique to the specific test case such as Time and Flow Rate, Temperature as well as if the Thermal Hysteresis test case was incremental or non-incremental in nature.

Test Case Identifier	Characterization Experiment Type	Constituent	Concentration (w/v%)	Relevant Parameter: Time; Flow Rate / Temperature / Incremental OR Non-Incremental
EV-1A	Evaporation	PVA Solution	1.58	95.38 Hours; 0.1 LPM
EV-1B-I	Evaporation	PVA Solution	1.58	24.00 Hours; 0.1 LPM
EV-1B-II	Evaporation	PVA Solution	1.58	05.00 Hours; 0.5 LPM
EV-1C	Evaporation	PVA Solution	1.58	21.03 Hours; 0.5 LPM
TH-1	Thermal Hysteresis	PVA Solution	1.58	45 °C; Incremental
TH-2A-I	Thermal Hysteresis	PVA Solution	1.58	60 °C; Incremental
TH-2A-II	Thermal Hysteresis	PVA Solution	1.58	60 °C; Post Cooldown H_2O Addition
TH-2B	Thermal Hysteresis	PVA Solution	1.58	60 °C; Incremental
TH-2C	Thermal Hysteresis	PVA Solution	1.58	60 °C; Non-Incremental
TH-3A	Thermal Hysteresis	PVA Solution	1.58	75 °C; Incremental
TH-3B	Thermal Hysteresis	PVA Solution	1.58	75 °C; Incremental
TH-3C	Thermal Hysteresis	PVA Solution	1.58	75 °C; Non-Incremental

6 Results

This chapter presents the results obtained from experiments performed to address the objectives of this work. The result from wall effects that occurs when sample beakers are not adequately centred relative to the spindle of the viscometer is presented first as this is a source of error that results in high viscosities.

Next, the density, viscosity and pH results of the individual constituents are described, starting with reverse osmosis water (which was used to manufacture the gels and the gel constituents), and then the remainder of the constituents, borax, fructose, borax-fructose, and PVA. Specific to PVA solution characterization, additional sub-sections detailing non-Newtonian, thermal hysteresis and evaporation rate results were included.

6.1 Wall Effects on Viscometer Measurements

During rheological constituent characterization of large samples, which required the use of a beaker, inadequate centring of the beaker relative to the spindle, results in wall effects causing increased viscosity. Viscosity measurements of RO water with the beaker placed at the centre as well as near the edge of the beaker in relation to the spindle (as can be seen in Figure 29 and Figure 30) were obtained to verify wall effects on viscosity readings.

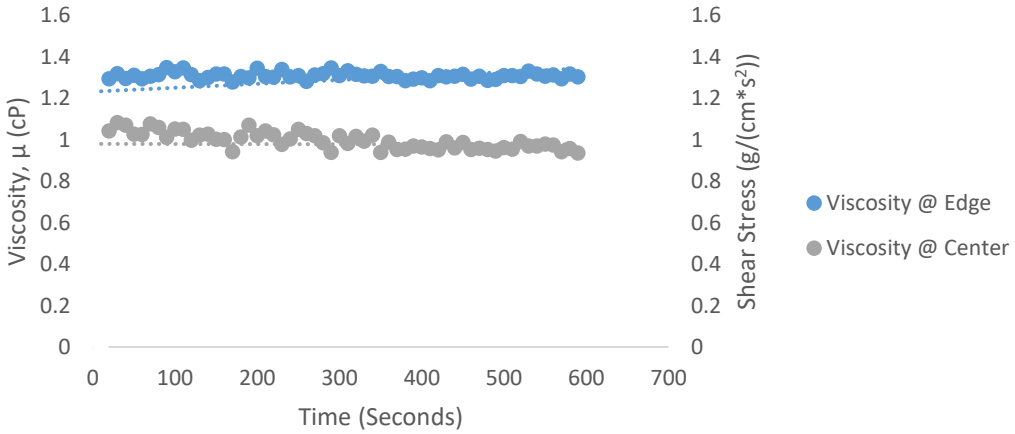

Figure 28: Wall effects on viscosity reading; Centre Vs Off Centre Viscosities of reverse osmosis water

The viscosity measurements of RO water at the centre in comparison to when the beaker is placed off centre in relation to the spindle is depicted in Figure 28, where an increase of viscosity is observed when the spindle is placed closer to the edge of the beaker, allowing for us to verify that wall effects do in fact result in artificially larger than normal viscosity readings. In this case, the dynamic viscosity at the centre was measured to be 0.99 mm^2/s compared to 1.3 mm^2/s at the edge.

Figure 29: Wall effects on Viscosity Reading; At center

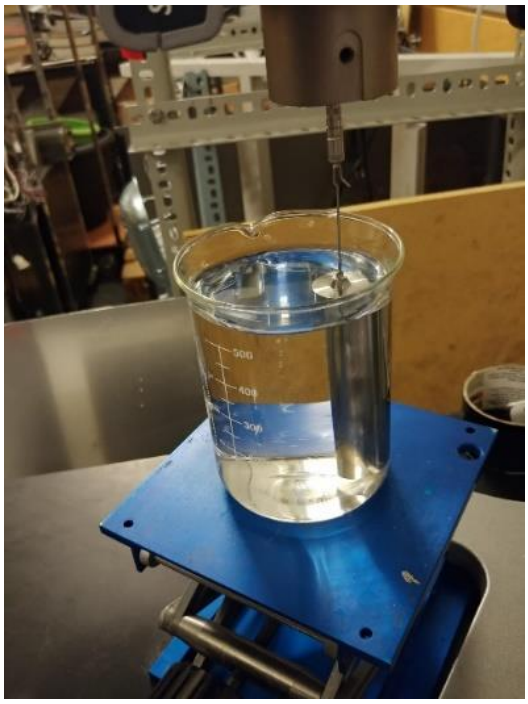

Figure 30: Wall effects on Viscosity Reading; At Edge

6.2 Constituent Characterization

Results from the characterization of borax, fructose, borax-fructose, and PVA, including density, rheology, evaporation as well as qualitative observations have been presented within this section.

6.2.1 Reverse Osmosis Water

The density and viscosity characteristics of reverse osmosis water was determined first, both for baseline characterization as well as for verification of the quality of the water. The density and dynamic viscosity of water at 294.15 °K was reported to be 0.998 $\frac{g}{mL}$ and 0.978 cP respectively [139]. Comparison to measured values are in Table 10.

Table 10: Density Characterization of RO Water used for the manufacturing of various constituents.

Sample size of 50 ± 0.5 mL.

Test Case Identifier	Mass (g) ±0.5	Density Calculated from Experimental Results (g/mL) ±0.02	Experimental Viscosity (cP)
WTR-BC-1	49.41	0.988	0.987
WTR-BC-2	49.49	0.989	0.987
WTR-BC-3	49.57	0.991	1.041
WTR-BC-4	49.13	0.983	0.989
WTR-BC-5	49.61	0.992	0.945
WTR-BC-6	49.62	0.992	0.944
WTR-BC-7	49.62	0.992	0.928
WTR-BC-8	49.46	0.989	0.942
WTR-BC-9	49.47	0.989	0.965

Different batches of RO water were used for the manufacturing of varied concentrations of the different constituents. The first batch was used for the manufacturing of various concentrations of borax solutions, likewise, the second batch was used for the manufacturing of various concentrations of fructose solutions and the third batch was used for manufacturing of various concentrations of borax-fructose solutions. Density and viscosity characterization results, of the various batches of RO water, are in Table 10. The results of the density and viscosity characterization of RO water from Table 10, are comparatively depicted in Figure 31 and Figure 32.

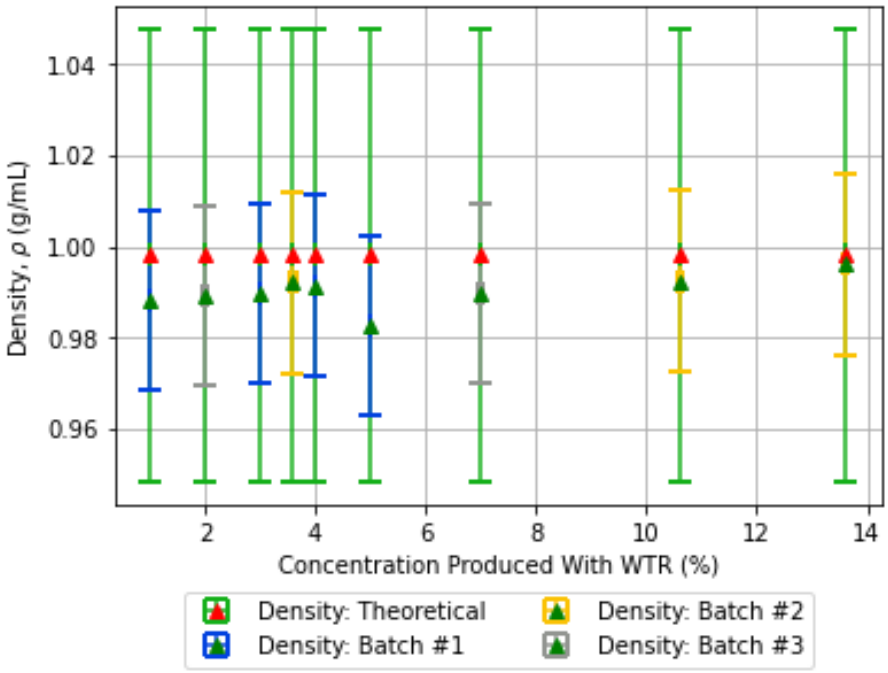

Figure 31: Comparison of densities of RO Water used for the manufacturing of varied concentrations of constituent solutions; Batch #1 = Borax Solutions, Batch #2 = Fructose Solutions, Batch #3 = Borax-fructose Solutions

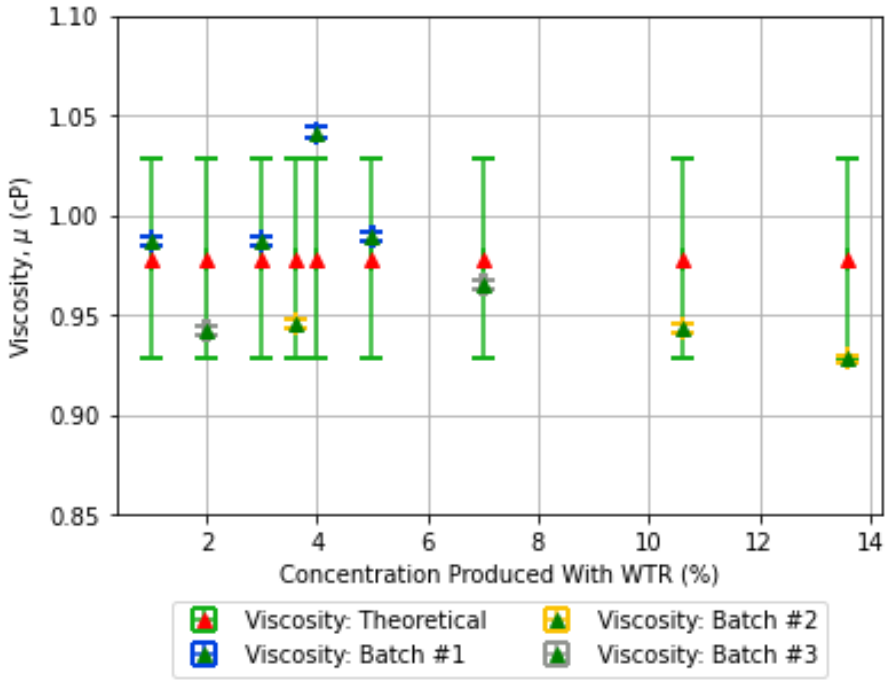

Figure 32: Comparison of average Dynamic Viscosity of RO Water used for the manufacturing of varied concentrations of constituent solutions; Batch #1 = Borax Solutions, Batch #2 = Fructose Solutions, Batch #3 = Borax-fructose Solutions

Batch #1 in Figure 31 and Figure 32 represents RO water used for the manufacturing of various concentrations of borax solutions. Batch #2 and batch #3, are RO water used for various concentrations of fructose and borax-fructose solutions respectively. The acceptable uncertainty of 5% for theoretical density and viscosity of water is indicated in green in Figure 31 and Figure 32. Comparing the uncertainty for theoretical density (Figure 31) and theoretical viscosity (Figure 32) to the experimental density and viscosity characterization results of RO water, it can be determined that the results are within uncertainty, excluding the singular viscosity outlier from batch #1, in Figure 32. Given that the density and viscosity characterization results for RO water are within the uncertainty values, when RO water baseline data is referred to within depictions of density and viscosity characterization results of the other constituents (such as Figure 36, and Figure 43), it is the averaged density and viscosity of RO water that is depicted.

The outlier from batch #1 is due to wall effects related error. Specifically, the beaker holding the RO water not being adequately centered relative to the spindle. This was confirmed as the source of error when results from viscosity observations of the borax solution manufactured with this batch of water was examined relative to other concentrations of borax manufactured with alternative batches of water (WTR-BC-1, WTR-BC-2, and WTR-BC-4, as per Table 7). The viscosities of the various concentrations of borax follow the power law trend (discussed in section 6.2.2.3). If the viscosity of the "WTR-BC-3" RO water batch were indeed truly 1.04 cP, and higher than the viscosities of the batches used to manufacture the other concentrations of borax solutions, this increased viscosity would be reflected in the viscosity observation results of borax solutions however this was not the case with the 4 w/v% borax solution manufactured using this batch, which has a viscosity of 1.04 cP, following the increasing trend as indicated by Figure 38. This confirmed that the high viscosity of the "WTR-BC-3" batch was due to an error.

The pH of different batches of RO water were measured and recorded. The pH of the RO water batches used for fructose solution and PVA solution manufacturing were measured and are in Table 11:

Table 11: pH of various batches of RO water used to manufacture Fructose and PVA constituent solutions of varied concentrations.

Concentration (%)	pH (± 0.01)	Temperature (± 2.5 °C)
WTR-BC-6	7.45	21.8
WTR-BC-7	7.45	22.4
WTR-BC-10	7.44	22.5

6.2.2 Borax / Borax Solutions

6.2.2.1 Thermogravimetric Analysis

This section discusses the results of the borax hydration state experiments which is identified by test case HS-1 as per Table 8. The borax constituent has various states of hydration depending on the environmental conditions of storage and transportation. The purpose of analyzing borax using a thermogravimetric analyzer (TGA) was to quantify the water content to verify the state of hydration of the borax as reported by the manufacturer [98]. This is important to identify the hydration of borax used in the formulation of the PVA-borax gel, as well as for the purposes of adjusting the water content of gels manufactured in the future in cases where the state of hydration may vary from the state determined here due to using borax of a different hydration state.

The method outlined in section 5.2.10 was used to perform the thermogravimetric experiments. 772.25 ± 0.01 mg of borax was deposited into a crucible, which was placed inside the TGA. The sample was then heated, at a heating rate of 288.15 $\frac{^{o}K}{min}$ until a temperature of 573.15 °K was reached, at which point temperature was held steady for approximately 1.5 hours. Heating and holding at elevated temperatures resulted in the evaporation of the water content. The reduction in mass, as well as temperature were observed continuously throughout the experiment, results of which are depicted in Figure 33, to Figure 35.

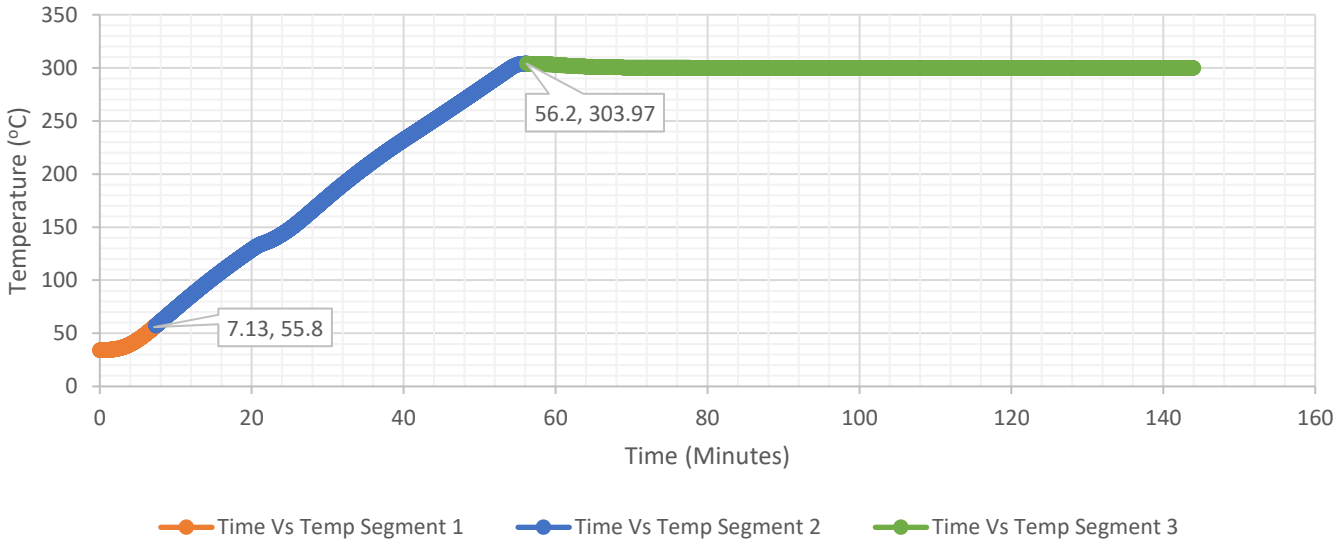

Figure 33: Temp vs Time Plot of TGA Experiment #1; Temperature Hold of 573.15 °K (300 °C) for 1.5 hrs reached at around the 56-min mark.

The first segment of raw data that has been plotted, indicated in orange, were measured by the TGA during the start-up phase [140] and is the instrument self-calibration phase and was not used. During the calibration phase the mass measured was higher than the initial mass of 772.25 mg. Once calibration was completed at the 7-min mark, readings were obtained, at which point the temperature was measured to be approximately 329.15 °K (or 56 °C as indicated by the callout in Figure 33.

Data obtained during the temperature hold are indicated by the green segment of Figure 33, Figure 34, and Figure 35; up until this point the borax sample was exposed to a constant increase in temperature of 15 K/min. A linear increase in temperature occurs up until 573.15 °K (300 °C). A rapid decrease in mass begins to occur around the 20-min mark at approximately 406.15 °K (133 °C), and with a rate of mass decrease of 9.3 mg/min for segment 2, and 2.5 mg/min for segment 3. Prior to this point the mass had already decreased to approximately 763 mg.

The rate of mass change slows down around 56 mins, when the temperature hold setpoint is reached, at which point the mass has dropped to 587 ± 0.01 mg. The rate of mass decrease at this point was approximately 0.09 mg/min, as indicated via the linear line of best fit for segment 4 (Figure 34).

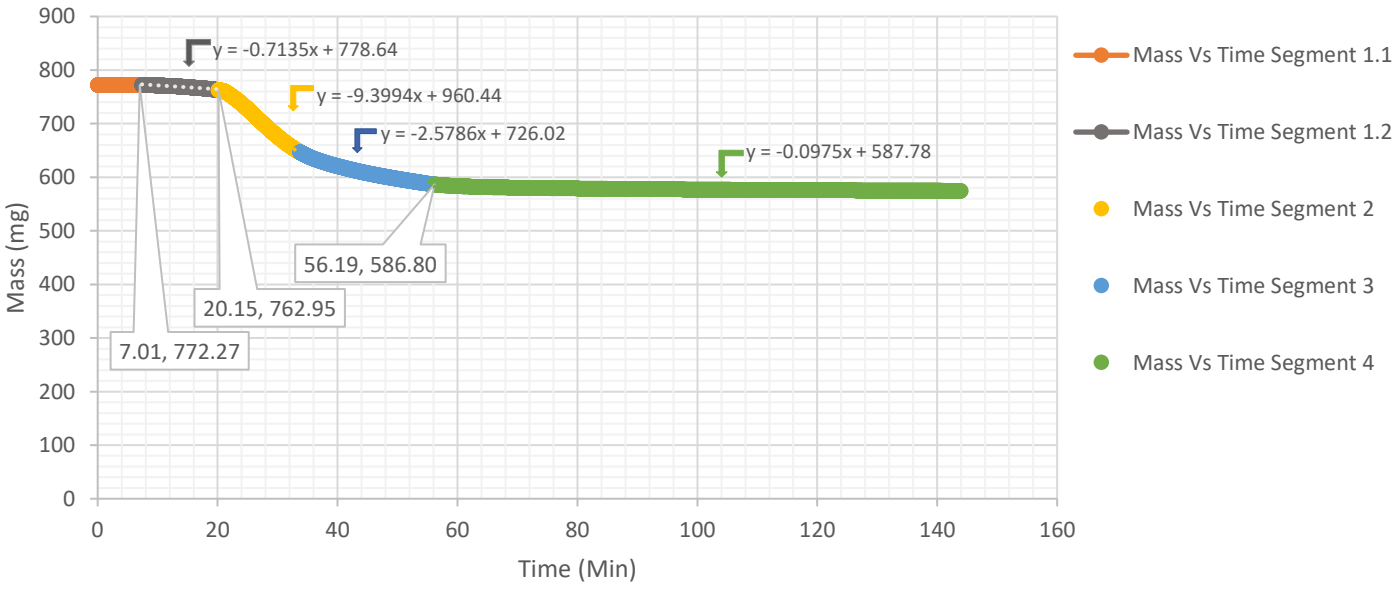

Figure 34: Mass Vs Time Plot of TGA Experiment #1; Temperature Hold at 300 0C for 1.5 hrs

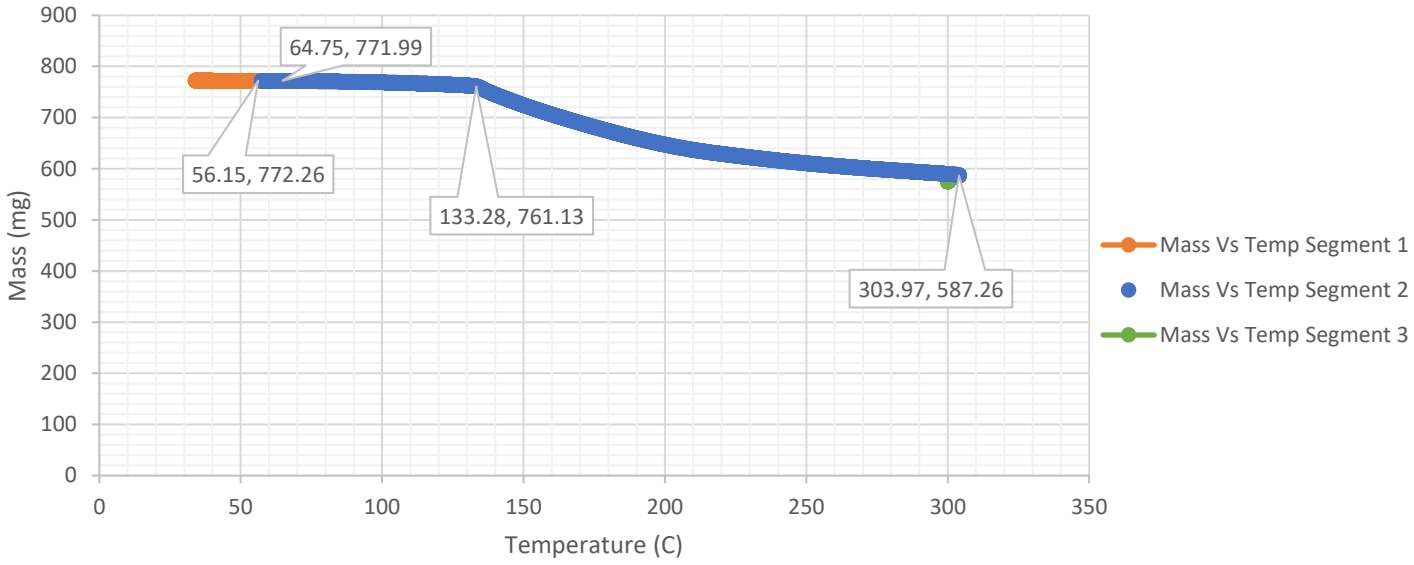

Figure 35: Mass Vs Temp Plot of TGA Experiment #1; Temperature Hold at 300 °C for 1.5 hrs

An important observation is that in the range of 331.15-334.15 °K (or 58-61 °C, which is the temperature point at which borax decahydrate transitions to borax pentahydrate [100]), there was very little change in mass, as can be seen from Figure 35. The change in mass across this range in data is only 0.27 mg. Based on this most of the constituents of the initial borax was already of the borax pentahydrate state. This was verified using stochiometric calculation in the next section.

6.2.2.1.1 Stochiometric Calculation

Assuming that the hydration level is at minimum, borax monohydrate, after holding the temperature at 300 °C for 1.5 hr, the hydration level of the borax prior to heating can be calculated from:

$$w\left(Na_2B_4O_7 \cdot Y(H_2O)\right) \rightarrow w\left(Na_2B_4O_7 \cdot 2(H_2O)\right) + z(H_2O) \qquad \text{Equation 51}$$

Assuming that holding the temperature for 1.5 hrs at 300 °C produced borax Monohydrate, the hydration state prior to heating using the TGA is given by Y below:

$$Y = 1 + \frac{z}{w} \qquad \text{Equation 52}$$

The parameter z can be calculated from:

$$z = \frac{\Delta_{mass}}{18.0153\ amu} = \frac{772.25 - 574.95\ mg}{18.0153\ amu} = \frac{0.1973\ g}{18.0153 \frac{g}{mol}} = 0.01095\ mol \quad \text{Equation 53}$$

and w was calculated to be:

$$w = \frac{Mass_{final}}{Molar\ Mass_{Na_2B_4O_7 \cdot 1(H_20)}} = \frac{0.57495g}{219.228 \frac{g}{mol}} = 2.6226 * 10^{-3} \quad \text{Equation 54}$$

Hence:

$$Y = 1 + \frac{0.01095}{2.6226 * 10^{-3}} = 5.1752 \quad \text{Equation 55}$$

The initial hydration level was determined to be 5.5. This is in agreement with the hypothesis made earlier of Pentahydrate due to the insignificant mass change at 61 °C. It is physically not possible to have a hydration state of 5.1752 (or 5.1752 H_2O). Rather, what this means is that a large portion of borax constituent is at a hydration state of 5 while some of the constituent is of a higher state of hydration.

6.2.2.2 Density

The densities of the varied concentrations of borax solutions are shown in Figure 36. Concentrations of 1%, 3%, 4%, and 5% solutions are plotted relative to their densities. As can be seen in Figure 36, density as a function of concentration increases with increasing concentration. The blue and the magenta-colored data points in Figure 36 are the datapoints associated with the original 3% (test case identifier D-2B-I), as well as the second batch of 3% borax solutions (test case identifier D-2B-II), respectively.

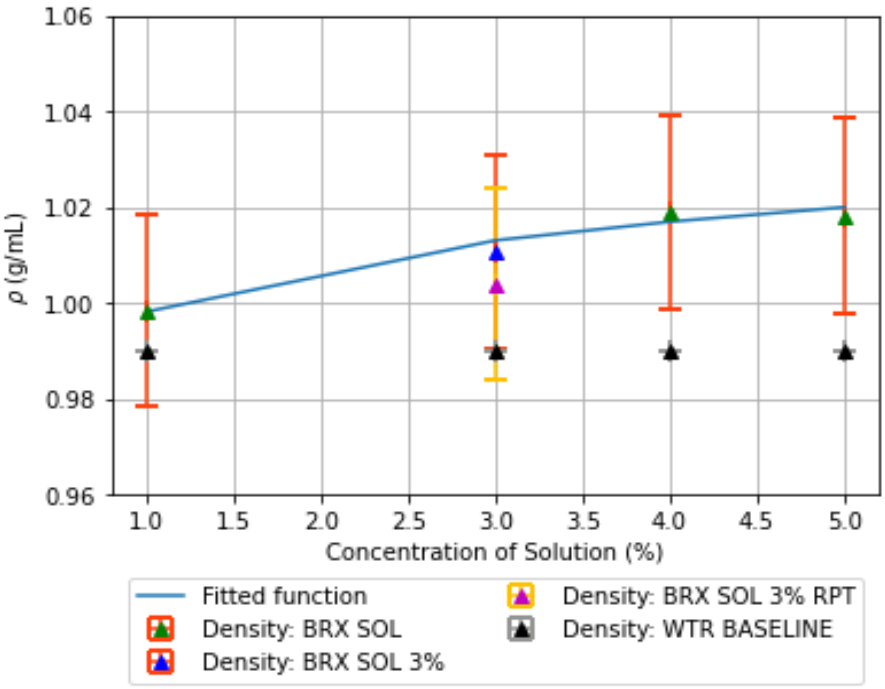

Figure 36: Averaged Densities of the Various Borax Concentrations. Measurements of water is displayed for baseline purposes. Uncertainty for water measurements is not displayed.

The datapoints in Figure 36 are tabulated in Table 12:

Table 12: Tabulated values - Viscosity as a Function of Concentration; Borax Solution

Concentration, $\frac{w}{v}$% ; Borax	Density, ρ ($\frac{g}{ml}$); ± 0.02 Experiment: Batch #1	Density, ρ ($\frac{g}{ml}$); ± 0.02 Experiment: Repeat Batch	Test Case Identifier (As per Table 7)
1	0.99	N/A	D-2A-I
3	1.01	1.00	D-2B-I; D-2B-II
4	1.02	N/A	D-2C-I
5	1.02	N/A	D-2D-I

Density increases in a logarithmic fashion, as depicted in Figure 36, plateauing at a concentration of 5 w/v%. This plateauing can be attributed to having reached the solubility limit, resulting in borax existing in solid form and settling at the bottom of the solution. This was observed in Figure 37. Beyond the point of saturation, any further addition of borax will only result in further precipitation. Therefore, the density of borax beyond 5 w/v% was not obtained.

A trendline of a natural logarithmic form, with an equation of y = 0.998+0.013*ln(x), with an R^2 value of 0.95 was found to best fit the data depicted in Figure 36; The 5 w/v% solubility limit [98] is indicated, not only by the precipitation observed in Figure 37, but also by the logarithmic behaviour of the density – concentration relationship.

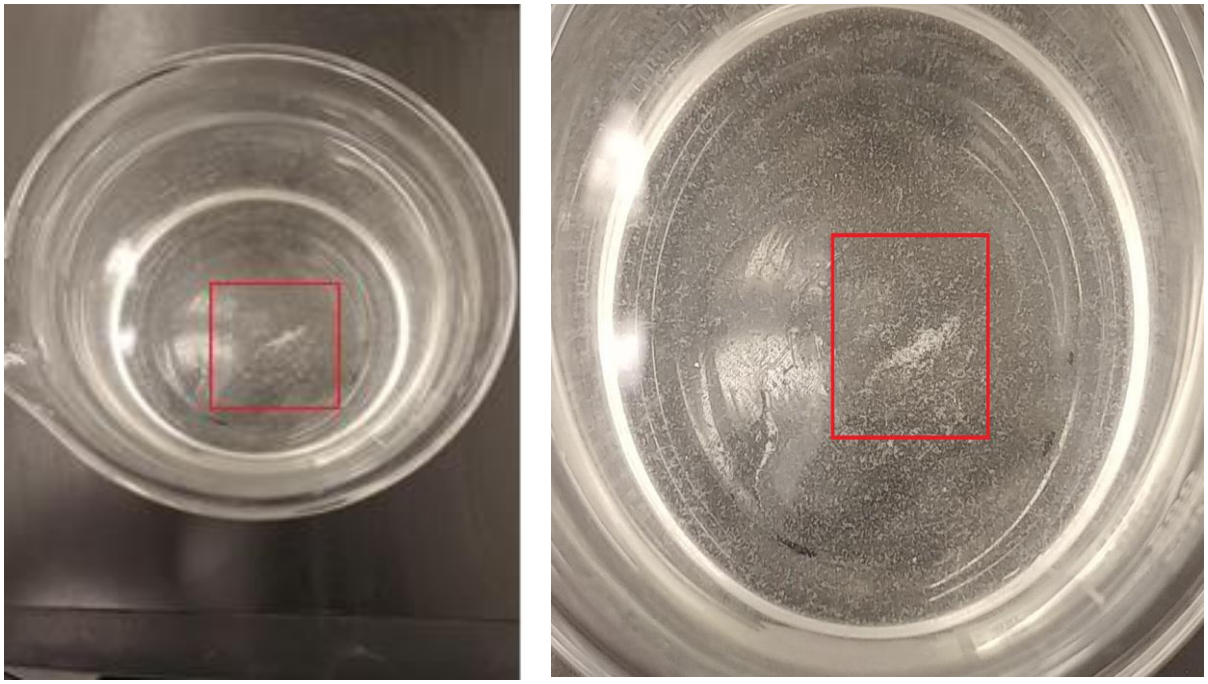

Figure 37: Borax Solution 5 w/v%; Precipitation Observed.

6.2.2.3 Viscosity

Viscosities of varied concentrations of borax were measured using the viscometer. The average of the viscosity – time data for each of the borax solutions identified in Table 7 were then determined, based on the methods described in section 5.2.11. The averaged viscosity as a function of concentration, was plotted (Figure 38). Viscosity was observed to exponentially increase with concentration, with 4 w/v% having a higher viscosity than 1 w/v% and 5 w/v% having a higher viscosity than 1 and 4 w/v%.

The blue datapoint in Figure 38 is the 3 w/v% outlier with a higher viscosity attributable to beaker centering related errors. Due to the error in dynamic viscosity of the 3% borax solution and because the original solution was discarded, a new batch was manufactured. The density and dynamic viscosity of this solution is indicated in magenta in Figure 36 and Figure 38. The density of this 3 w/v% solution follows the logarithmic trend in Figure 36, without deviation.

The averaged viscosities of the various concentrations of borax solutions, depicted in Figure 38, are tabulated in Table 13. The viscosity increased from 0.99 cP at a concentration of 1 w/v% to a viscosity of 1.07 cP at a concentration of 5 w/v%.

Table 13: Tabulated values - Viscosity as a Function of Concentration; Borax Solution

Concentration, $\frac{w}{v}$% ; Borax	Viscosity (cP); Experiment: Batch #1	Viscosity (cP) Experiment: Repeat Batch	Test Case Identifier (As per Table 7)
1	0.99 ± 0.002	N/A	V-2A-I
3	1.07 ± 0.002	1.01 ± 0.002	V-2B-I; V-2B-II
4	1.04 ± 0.002	N/A	V-2C-I
5	1.07 ± 0.003	N/A	V-2D-I

The averaged viscosity of the 3 w/v% borax solution has a viscosity higher than that of the 4 w/v% and 5 w/v% solutions; this datapoint was deemed an outlier due to errors associated with centering the container of the solution relative to the spindle, as discussed in section 6.1. Removing the outliers in the datasets, and combining viscosity observations from both batches, the viscosity trendline depicted within Figure 38 was developed. A power law based trendline, with an equation of: $y = 0.99 + 1.25 * 10^{-3} * (x^{2.56})$ and R^2 value of 0.99 was used to describe the viscosity of borax solution as a function of increasing concentration.

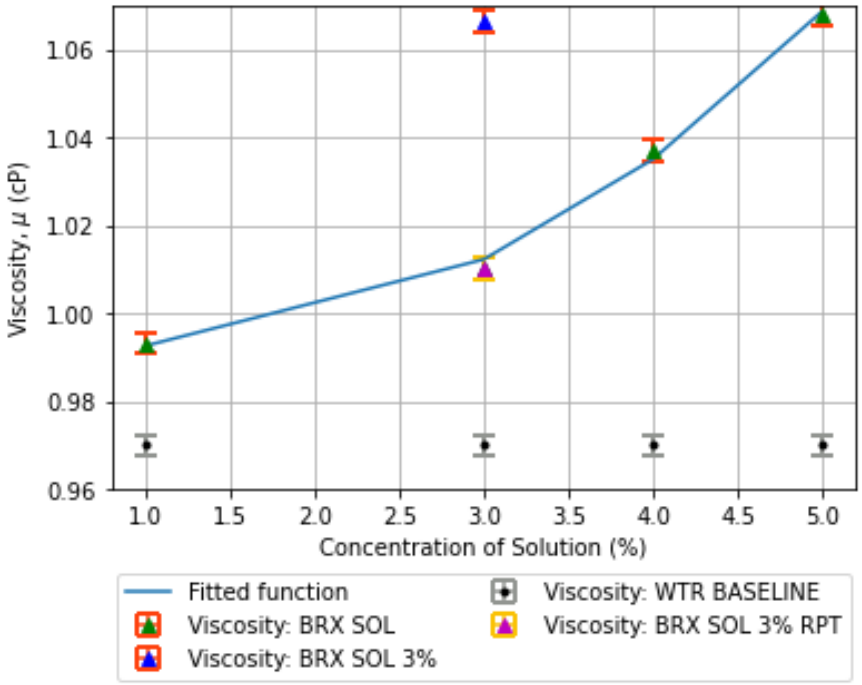

Figure 38: Averaged Dynamic Viscosity of Varied Borax Concentrations; With 3% outlier (blue datapoint) and repeat datapoint.

6.2.2.4 7% Borax Solution

The solubility limit of borax was reported to be 5 w/v% [98]. This was consistent with the precipitation that was observed after manufacturing a 5 w/v% borax solution (Figure 37) and further validated after manufacturing a 7% borax solution (test case identifier SL-1, as per Table 8) as depicted in Figure 39.

After adding 500 mL of RO water to 35g of borax (equivalent to 7 w/v%), the solution was then heated to approximately 333.15 °K, while being stirred. After approximately 30 mins of heating and stirring, a clear solution was obtained. However, as the solution was allowed to cool it became super saturated, as observed in Figure 40. The warm clear solution was then placed in a cold bath to bring the temperature back down to ambient room temperature (approximately 24 °C) resulting in the formation of precipitation (as labelled within Figure 40)

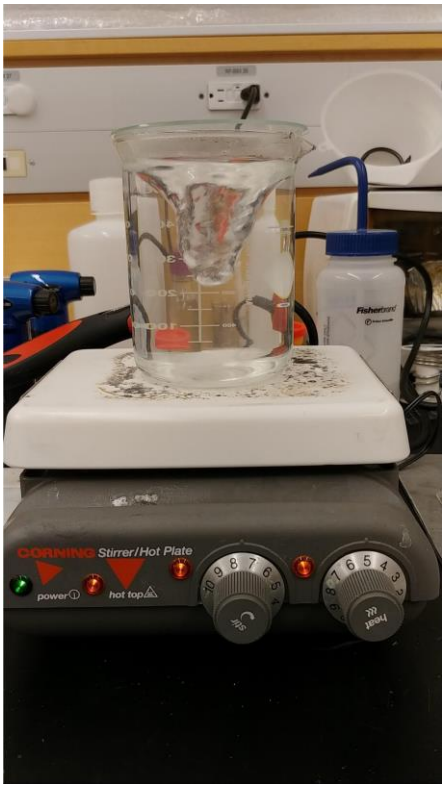

Figure 39: 7% Borax Solution @ Approximately 60 °C

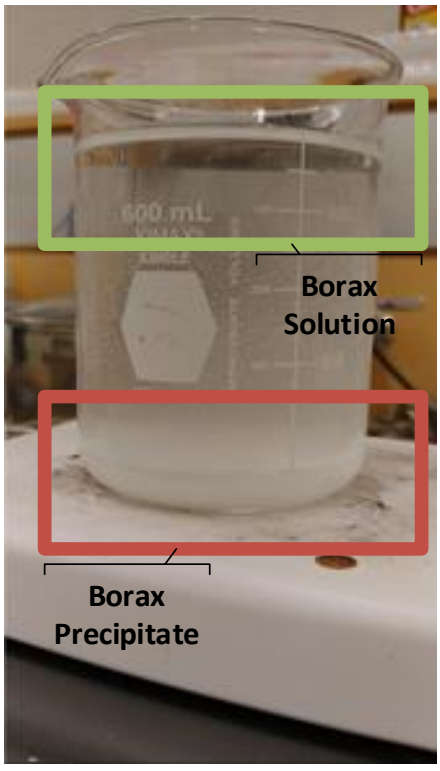

Figure 40: Post Cold Bath; Approximately 24 °C

6.2.2.5 pH

The pH for various concentrations of borax solutions were recorded and were found to be alkaline in nature and tabulated in Table 14:

Table 14: pH of various concentrations of Borax solutions at ambient temperatures

Concentration (%)	pH (± 0.01)	Temperature (± 1 °C)	Test Case Identifier (As per Table 8)
1	9.00	20.8	pH-1A-I
3	9.03	21.3	pH-1B-II
5	9.05	21.3	pH-1C-I

The pH remained the same across the various borax concentrations at an alkaline pH of approximately 9 (± 0.01). The results from Table 14, depicted within Figure 41 is verified using literature which states that borax in aqueous form, where boric acid and $B(OH)_4^-$ exist in equilibrium the overall pH of the environment is approximately 9.13 [141].

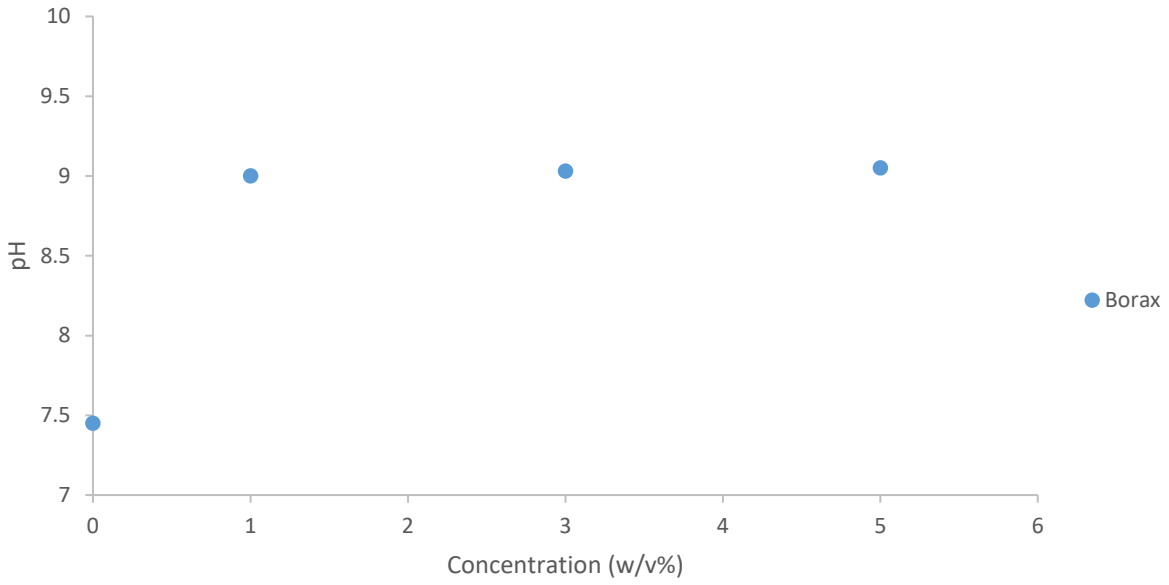

Figure 41: Plot of pH as a function of borax solution concentration; Includes 0 w/v% Concentration, equivalent to RO Water pH.

6.2.3 Fructose Solution

6.2.3.1 Density

The densities of the various fructose solutions have been plotted, relative to their concentration, in Figure 42. Density as a function of concentration was found to increase with increasing concentration. A linear trendline with an equation of $y = 0.003x + 0.99$, and an R^2 value of 0.95 was found to best fit the data depicted in Figure 42. The densities of the various concentrations of Fructose solutions, depicted in Figure 42, are tabulated in Table 15.

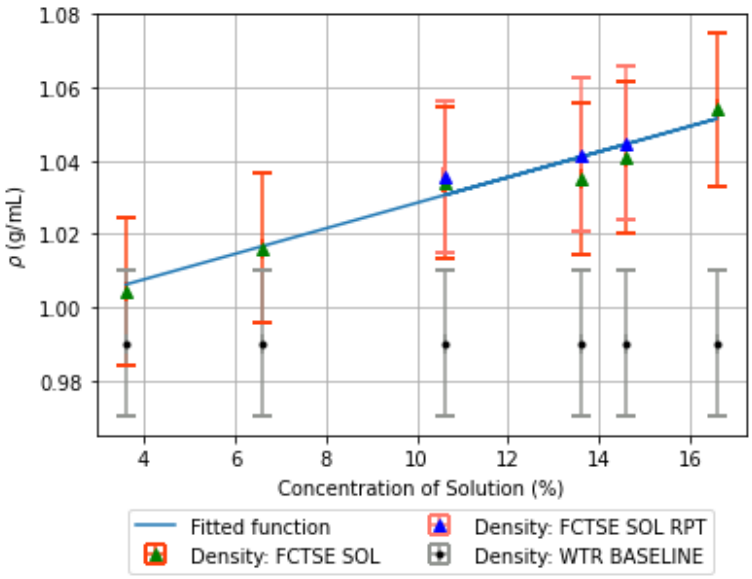

Figure 42: Averaged Densities of the Various Fructose Concentrations

Table 15: Tabulated values – Density as a Function of Concentration; Fructose Solution – batch #1 and repeat batch.

Concentration, $\frac{w}{v}$% ; Fructose	Density, ρ ($\frac{g}{ml}$); ± 0.02 Batch #1; Repeat Batch	Test Case Identifier; Repeat Test Case Identifier (As per Table 7)
3.6	1.00	D-3A-I
6.6	1.016	D-3B-I
10.6	1.034; 1.035	D-3C-I; D-3C-II
13.6	1.035; 1.042	D-3D-I; D-3D-II
14.6	1.040; 1.045	D-3E-I; D-3E-II
16.6	1.054	D-3F-I

6.2.3.2 Viscosity

Viscosities of various fructose solutions were obtained from the viscometer. The average of the viscosity – time data for each of the concentrations of Fructose solutions were then determined, based on the methods described in section 5.2.11.

Averaged viscosity as a function of concentration, was plotted, as per Figure 43). As expected, the viscosity of fructose increases with concentration [142]. A power law function was found to best fit this increasing behaviour, as observed in Figure 43. The viscosity of the 13.6 w/v% solution of the first dataset (test case identifier: V-3D-I) and the viscosity of the 14.6 w/v% solution of the repeat dataset (test case identifier: V-3E-II) relative to the other averaged viscosities do not follow the power law trend. Referring to Figure 42 these outliers can be attributed to viscosity alone as it can be seen that the density of the repeat D-3D-II solution is in between the densities of 10.6 w/v% and 14.6 w/v% solutions, and follows the trend of increasing density as a function of increasing concentration. Inadequate centring of the container of the solution relative to the spindle may be one reason for this outlier, as discussed in section 6.1.

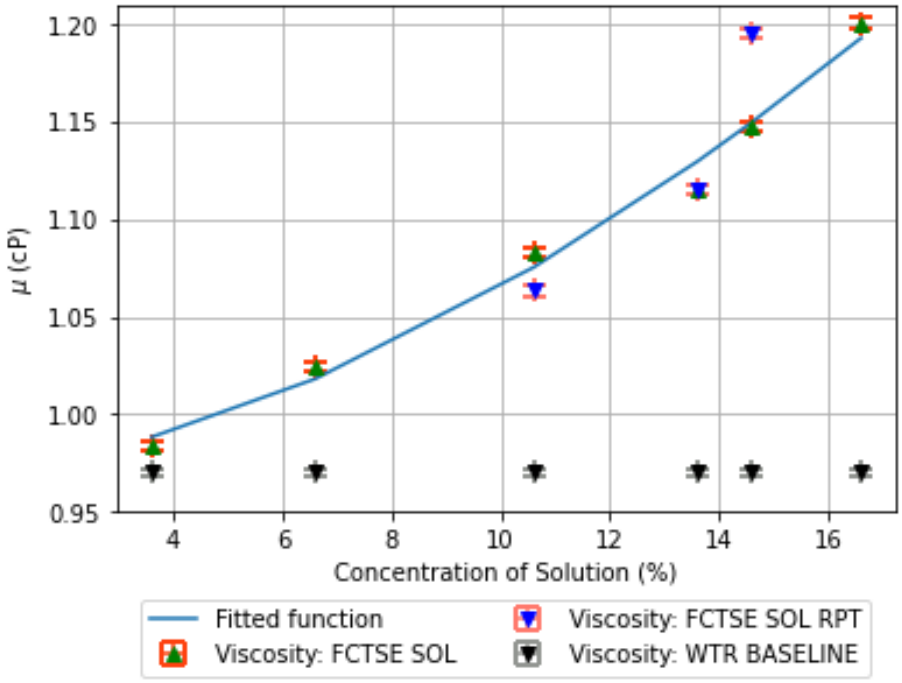

Figure 43: Averaged Dynamic Viscosity of Varied Fructose Concentrations; With 3% outlier (blue datapoint) and repeat datapoint.

The averaged viscosities of the various concentrations of Fructose solutions, depicted in Figure 43, are tabulated in Table 16:

Table 16: Tabulated values - Viscosity as a Function of Concentration; Fructose Solution – batch #1

Concentration, $\frac{w}{v}\%$; Fructose	Viscosity (cP) Experiment: Batch #1; Repeat Batch ± 0.05	Test Case Identifier; Repeat Test Case Identifier (As per Table 7)
3.6	0.98	V-3A-I
6.6	1.02	V-3B-I
10.6	1.08; 1.06	V-3C-I; V-3C-II
13.6	*1.18; 1.12*	V-3D-I; V-3D-II
14.6	1.15; 1.195	V-3E-I; V-3E-II
16.6	1.2	V-3F-I

As tabulated above, the viscosity increased from 0.98 cP at a concentration of 3.6 w/v% to a viscosity of 1.2 cP at a concentration of 16.6 w/v%. Removing the outliers in the datasets, and combining viscosity observations from both batches, the viscosity trendline depicted in Figure 43 was developed.

A power law based trendline, with an equation of: $y = 0.97 + 1.93 * 10^{-3} * (\mathrm{x}^{1.69})$ and R^2 value of 0.99 was used to describe the correlation of the viscosity of Fructose solution as a function of increasing concentration.

6.2.3.3 pH

The pH for the various concentrations of fructose solutions were recorded. The pH for all concentrations of fructose solutions were found to be close to neutral and are tabulated in Table 17. Although there was a slight change in pH from a pH of 7.57 at a Fructose concentration of 3.6 wt% to a pH of 7.12 at a fructose concentration of 16.6 wt%, the change in pH is within the uncertainty of the instrument and is negligible. Plotting the data from Table 17, Figure 41 was produced. A decreasing trend of pH as a function of concentration can be observed.

Table 17: pH of various concentrations of Fructose solutions at ambient temperatures

Concentration (%)	pH (± 0.01)	Temperature (± 1 °C)	Test Case Identifier (As per Table 8)
3.6	7.57	20.8	pH-2A-I
6.6	7.19	22.4	pH-2B-I
10.6	7.18	21.8	pH-2C-I
14.6	7.17	22	pH-2D-I
16.6	7.15	21.8	pH-2E-I

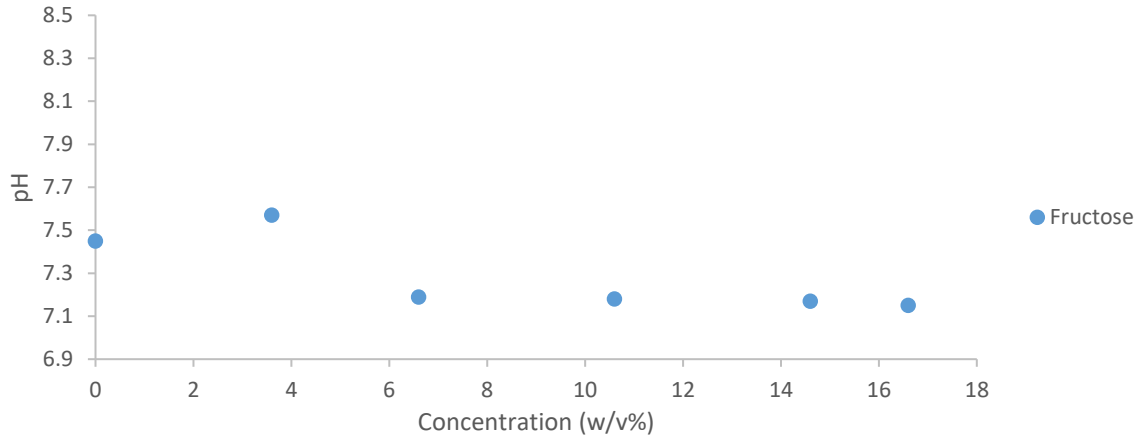

Figure 44: Plot of pH as a Function of increasing concentration of Fructose Solutions; Includes 0 w/v% Concentration, equivalent to RO Water pH.

6.2.4 Borax-Fructose Solution

6.2.4.1 Density

The densities of the various borax solutions, with a constant concentration of fructose of 13.6 W/v% are depicted in Figure 45 where it can be seen that density increases with increasing concentration. The datapoints indicated in black are of the RO water used for the manufacturing of the solutions. It must be noted that 0 w/v% borax-fructose is simply 13.6 w/v% fructose solution alone, without the addition of any borax. Hence, the density and density delta measurement of the 0 w/v% borax-fructose solution in Figure 45 are equivalent to the measurements of 13.6 w/v% Fructose (test case identifier: D-3D-II), in Figure 42 of section 6.2.3.1. A trendline of exponential form, with an equation of $y = 1.04 * e^{0.0045x}$, and an R^2 value of 0.98 was found to best fit the data.

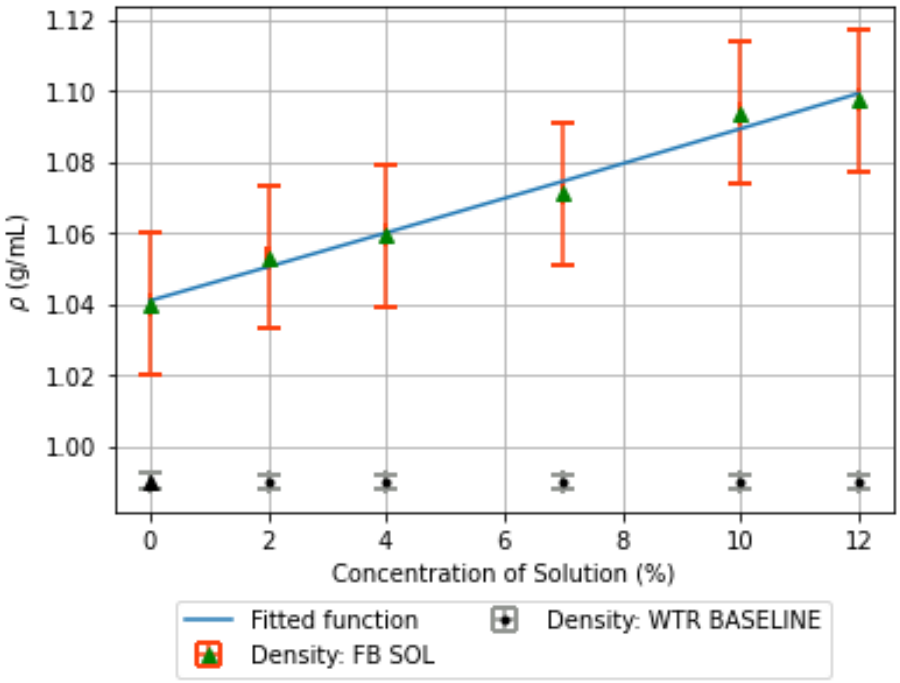

Figure 45: Averaged Densities of the Various Borax-fructose Solution Concentrations; Constant Fructose Concentration of 13.6 w/v%

Results

The densities of the various concentrations of Fructose solutions, depicted in Figure 42, are tabulated in Table 18:

Table 18: Tabulated values – Density as a Function of Concentration; Fructose Solution – batch #1 and repeat batch.

Concentration, $\frac{w}{v}$% ; Fructose	Density, ρ ($\frac{g}{ml}$); ± 0.02	Test Case Identifier; Repeat Test Case Identifier (As per Table 7)
0	1.04	V-4A
2	1.053	V-4B
4	1.059	V-4C
7	1.071	V-4D
10	1.093	V-4E
12	1.097	V-4A

6.2.4.2 Viscosity

Viscosities of borax-fructose solutions were obtained from the viscometer averaged viscosity as a function of concentration was plotted in Figure 46. The viscosity exponentially increases with concentration in Figure 46. The concentration of fructose remained constant at 13.6 w/v% in all the borax-fructose solutions. The viscosity of the 0 w/v% borax-fructose solution is equivalent to the viscosity of the 13.6 w/v% fructose solution (test case identifier: V-3D-II). The averaged viscosities of the various concentrations of borax-fructose solutions, depicted in Figure 46, are tabulated in Table 19:

Table 19: Tabulated values - Viscosity as a Function of Concentration; Borax-fructose Solution

Concentration, $\frac{w}{v}$% ; Borax-fructose Solution	Viscosity (cP) ± 0.002	Test Case Identifier (As per Table 7)
2	1.17	V-4A
4	1.20	V-4B
7	1.32	V-4C
10	1.43	V-4D
12	1.50	V-4E

The averaged viscosity increased from 1.17 cP at a borax concentration of 2 w/v% to a viscosity of 1.5 cP at a borax concentration of 12 w/v%. Based on the results in Table 19, the viscosity trendline in Figure 46 was developed. A power law based trendline, with an equation of: $y = 0.01 * e^{0.445x}$ and R^2 value of 0.99 was found to best fit the data and was used to describe borax-fructose solutions as a function of increasing borax concentration.

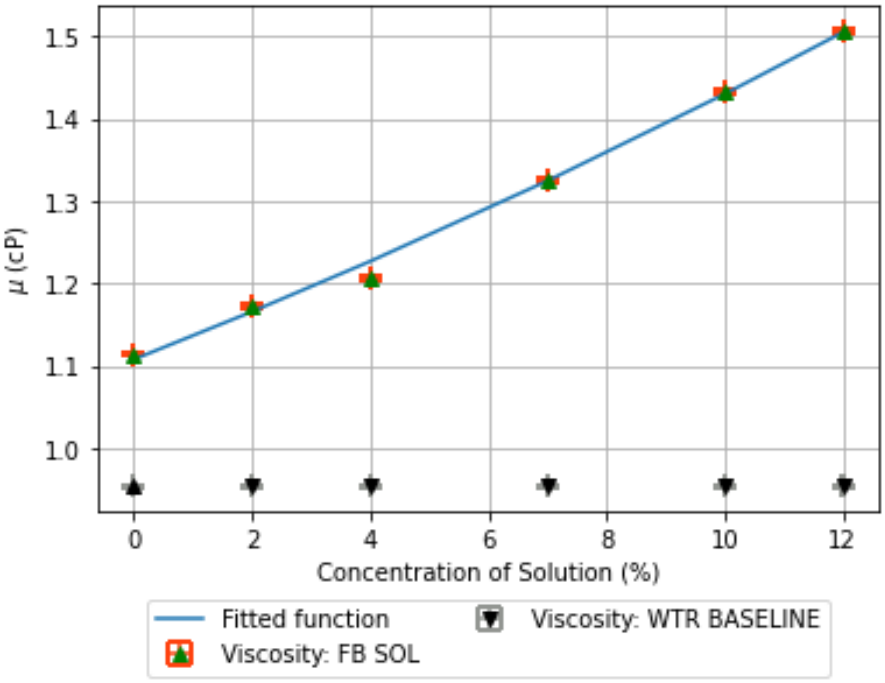

Figure 46: Averaged Viscosities of the Various Borax-fructose Solution Concentrations; Constant Fructose Concentration of 13.6 w/v%

6.2.4.3 pH

The pH for the various concentrations of borax-fructose solutions were recorded. pH increased as a function of increasing borax concentration (while fructose concentration remained at a constant 13.6 w/v% for all solutions), as tabulated in Table 20:

Table 20: pH of varied concentrations of Borax of Borax-fructose concentrations

Concentration (w/v%)	pH (± 0.01)	Temperature (± 1 °C)	Test Case Identifier (As per Table 8)
0	7.17	N/A	Interpolated from Table 17
2	4.55	20.9	pH-3A
4	5.23	22	pH-3B
7	5.78	21.5	pH-3C
10	7.23	22.2	pH-3D

The pH changed from being slightly alkaline at 0 w/v% borax concentration to a slightly acidic pH of 4.55 at a borax concentration of 2 wt%, (Table 20), and finally slightly alkaline, at a pH of 7.23 and a borax concentration of 10 wt%, as per Table 20. Plotting the data from Table 20, Figure 47 was produced. The results from Table 20 and Figure 47 shows the initial acidification and then the return to a relatively neutral environment. This trend is discussed in section 7.1.1.

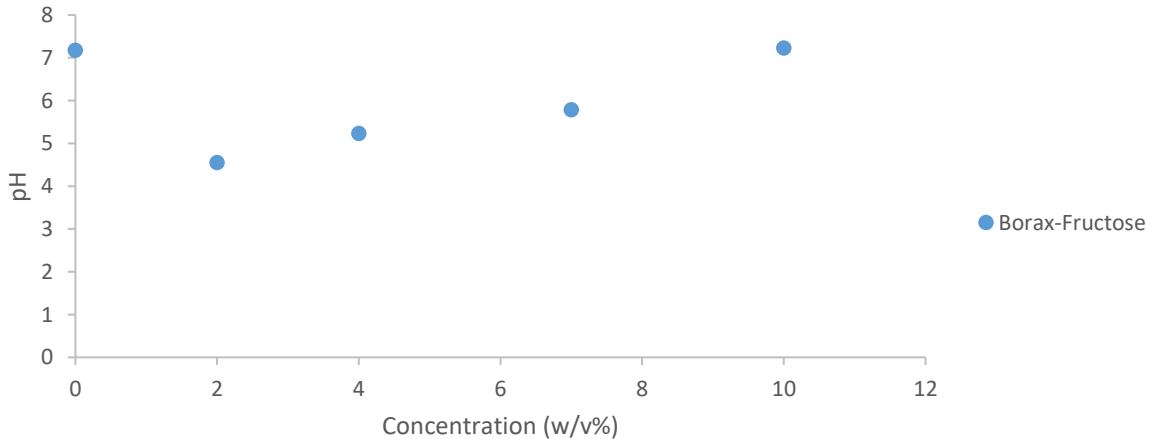

Figure 47: Plot of pH as a Function of increasing concentration of Borax-fructose Solutions; Includes 0 w/v% Concentration, equivalent to Fructose 13.6 w/v% pH.

6.2.5 PVA Solution

6.2.5.1 Density

The densities of PVA solutions are plotted in Figure 48. It can be seen that density increases with increasing concentration. It must be noted that no functional trendline within error can be used to fit the data in Figure 48. The densities of the various concentrations of PVA solutions are tabulated in Table 21.

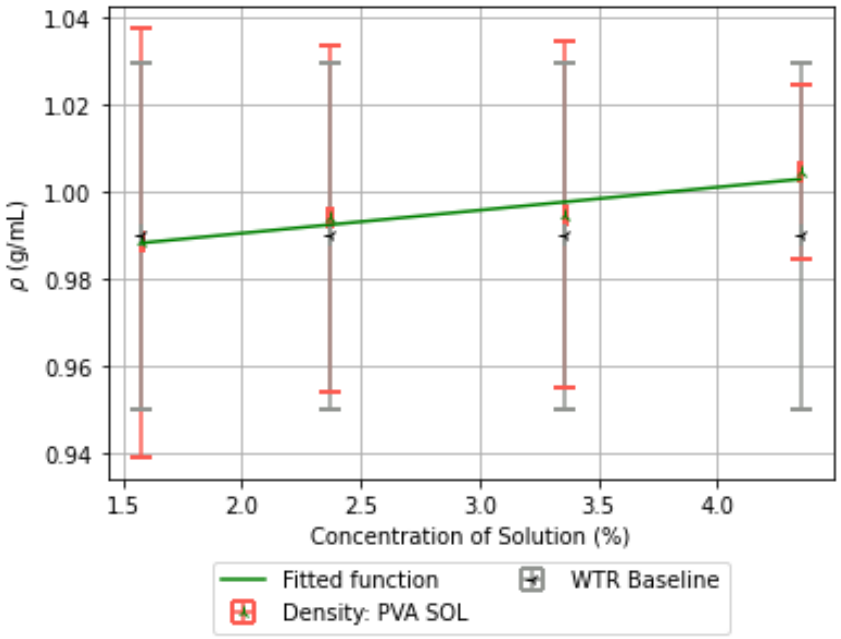

Figure 48: Averaged Densities of the Various PVA Concentrations

Table 21: Tabulated values - Density as a Function of Concentration; PVA Solution

Concentration, $\frac{g}{dL}$; PVA Solution	Density, ρ ($\frac{g}{ml}$); ± 0.02	Test Case Identifier (As per Table 10)
1.58	0.988	D-5A
2.37	0.994	D-5B
3.36	0.994	D-5C
4.35	1.00	D-5D

6.2.5.2 Viscosity

The viscosity of PVA solutions at room temperature (295.65 °K ± 2.5) using an LCP spindle and a beaker with a diameter ≥ 83 mm. The averaged viscosity in Figure 49 was observed to increase with concentration. The viscosities of the 1.58, 2.37 and 3.36 g/dL solutions were obtained at an RPM of 100 and a shear rate of 122.3 $\frac{1}{s}$. The viscosity of the 4.35 g/dL solution (test case identifier: V-5D) was obtained at an RPM of 60 and a shear rate of 73.38 $\frac{1}{s}$.

The averaged viscosities of the various concentrations of PVA solutions are tabulated in Table 22:

Table 22: Tabulated values - Viscosity as a Function of Concentration; PVA Solution

Concentration, $\frac{g}{dL}$; PVA Solution	Viscosity (cP)	Test Case Identifier (As per Table 10)
1.58	1.84 ± 0.06	V-5A
2.37	2.80 ± 0.09	V-5B
3.36	5.02 ± 0.23	V-5C
4.35	8.72 ± 0.63	V-5D

The viscosity increased from 1.84 cP at a concentration of 1.58 g/dL to a viscosity of 8.72 cP at a concentration of 4.35 g/dL. Based on the results in Table 22, the viscosity trendline was developed. A power law based trendline, with an equation of: $y = 1.36 + 0.14 * (x^{2.7})$ and R^2 value of 0.99 was used to describe the correlation of the viscosity of borax-fructose solutions as a function of increasing borax concentration.

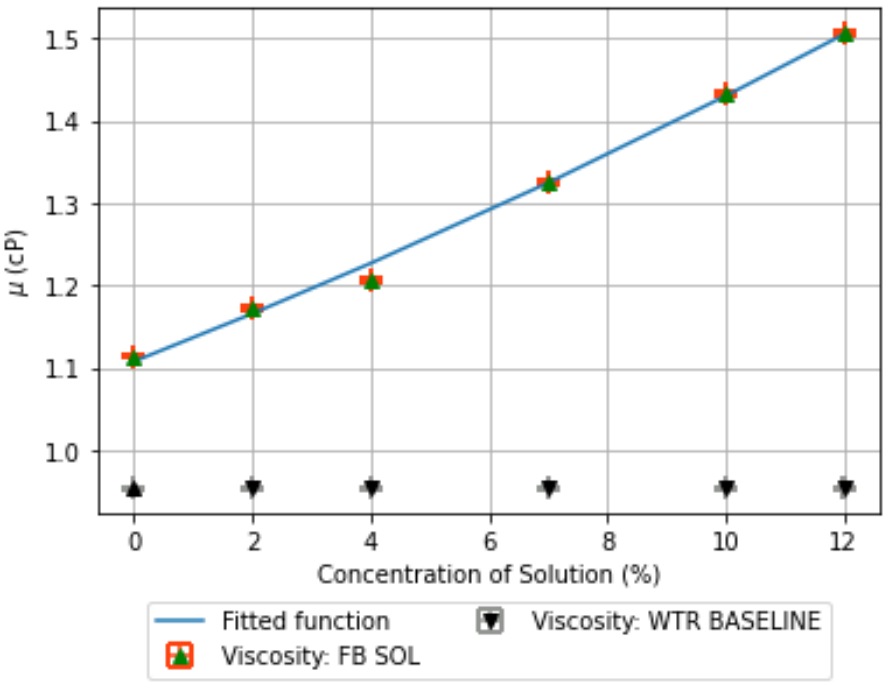

Figure 49: Depiction of the viscosities of the varied concentrations of PVA solutions manufactured; specifically, 1.58, 2.37, 3.36, and 4.35 g/dL solutions. The apparent viscosities for varied solutions were obtained using the same RPM of 100.

6.2.5.2.1 Non-Newtonian Behaviour

PVA solutions of concentrations up to 1.5 g/dL are expected to have Newtonian behaviour [143]; at concentrations greater than 1.5 g/dL, however, the fluid is expected to demonstrate non-Newtonian behaviour, with authors observing non-Newtonian behaviour for a 10 g/dL PVA solution [144]. This behaviour was verified by observing viscosity as a function of changing shear rate. The viscosity of a 1.58 g/dL PVA solution (test case identifier: NN-1A in Table 8) was measured at 100, 60, 50 and 30 RPM, equivalent to shear rates (Equation 31) of 122.3, 73.38, 61.5 and 36.69 $\frac{1}{s}$ respectively. In Figure 50, viscosity decreases from 1.71 cP at an RPM of 30 (shear rate of 36.69 $\frac{1}{s}$) to 1.68 cP at an increased RPM of 100 (shear rate of 122.3 $\frac{1}{s}$).

The viscosity of 3.36 g/dL PVA solution (test case identifier: NN-1B, in Table 8) was observed at 30, 20, 12, 10 and 6 RPM, which translates into shear rates of 36.69, 24.46, 14.68, 12.23 and 7.34 $\frac{1}{s}$ respectively. The resulting apparent viscosities are depicted in Figure 51. The viscosity decreases from 4.6 cP at 6 RPM (shear rate of 7.34 $\frac{1}{s}$) to 4.39 cP at an increased RPM of 30 (shear rate of 36.69 $\frac{1}{s}$).

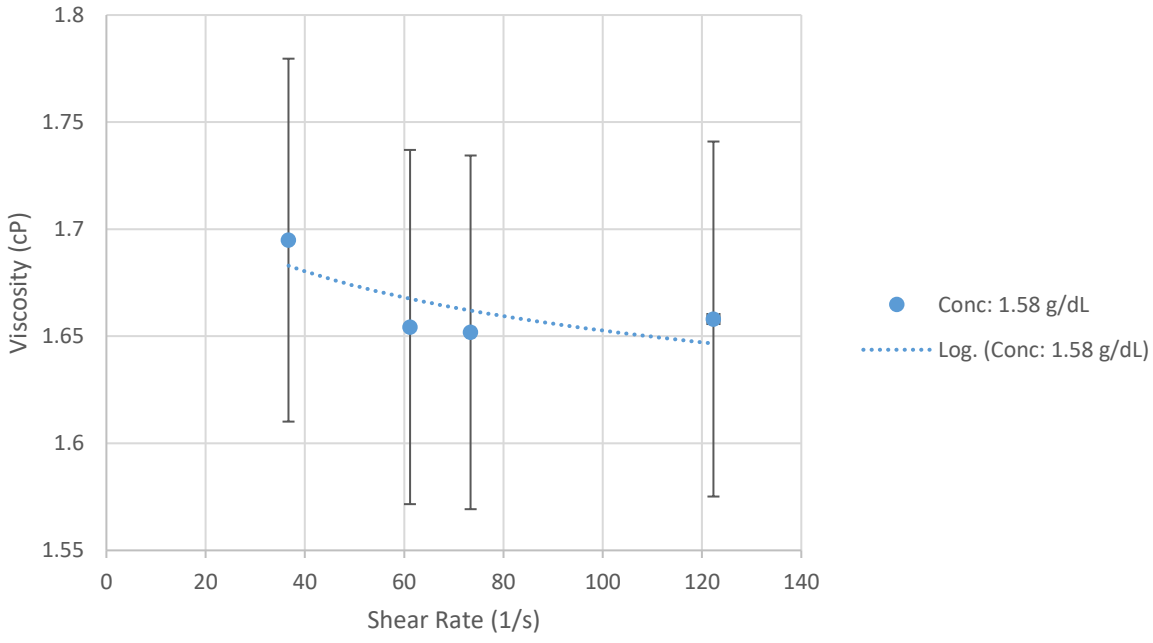

Figure 50: Plot of viscosity as a function of shear rate; PVA solution of concentration 1.58 g/dL

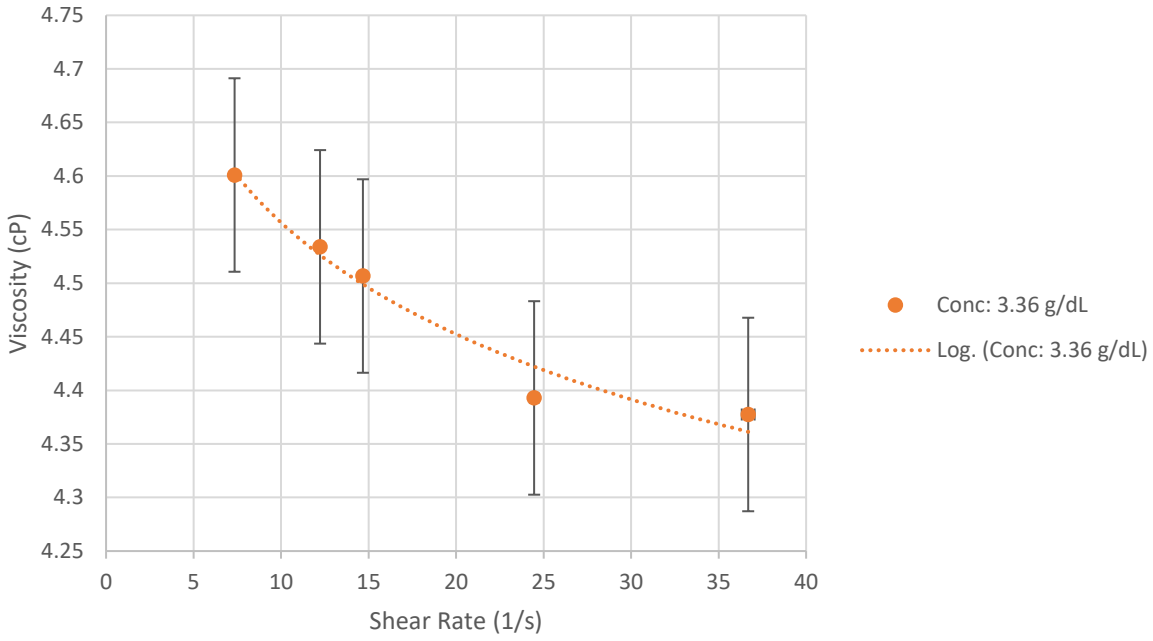

Figure 51: Plot of viscosity as a function of shear rate; PVA solution of concentration 3.36 g/dL

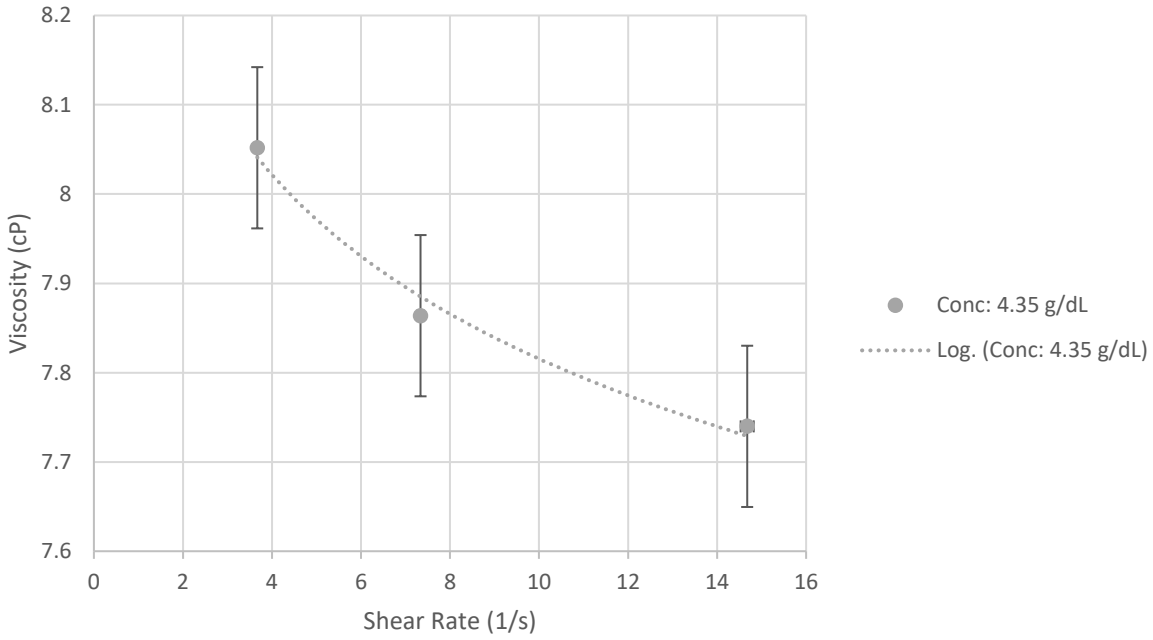

Figure 52: Plot of viscosity as a function of shear rate; PVA solution of concentration 4.35 g/dL

The viscosity of 4.35 g/dL PVA solution (test case identifier: NN-1C in Table 8) was measured 12, 6, and 3 RPM, equivalent to shear rates of 14.68, 7.34, and 3.67 $\frac{1}{s}$ respectively. The viscosities seen in Figure 52 decreases from 8.06 cP, (measured at 3 RPM, equivalent to a shear rate of 3.67 s-1) to 7.75 cP at an (measured at 12 RPM, equivalent to a shear rate of 14.67 $\frac{1}{s}$).

From Figure 50, Figure 51 and Figure 52, the change in viscosity for different concentrations of PVA solutions decreased as a function of increasing shear rate. This behaviour is indicative of shear-thinning behaviour [144]. Given that PVA solution demonstrates non-Newtonian shear-thinning behaviour, refencing of viscosities of PVA solutions above 1.5 g/dL must be accompanied by the associated shear rate used to obtain the respective viscosity; as the viscosity of non-Newtonian fluids are shear rate dependent.

6.2.5.2.2 Thermal Hysteresis Experiments

One of the primary environmental characteristics that can change the viscosity of fluids is temperature. Specific to polymers, as is the case with PVA, temperature dependent include storage modulus, loss modulus [87], damping coefficients and onsetting of glass transition [145]. This results in changes to viscosity [146]. According to literature, glass transition setpoints for PVA were observed at temperatures of 51, 63, and 75 °C [133]. In order to characterize viscosity as a function of temperature, observe any glass transition setpoints, as well as observe any time and/or temperature dependent viscosity changing effects, hysteresis temperature experiments were performed. Temperature hysteresis cycling were performed on 1.58, 3.36, and 4.35 g/dL PVA solutions.

The 1.58 g/dL PVA solution, temperature hysteresis cycling was performed at various maximum temperature setpoints. Maximum temperature cycling to 45, 60 and 75 °C were performed at an RPM of 100 and a shear rate 122.3 $\frac{1}{s}$. For the maximum temperature setpoint of 45 °C, viscosity of the 1.58 g/dL PVA solution was observed from a starting temperature of 30 °C, up to 45 °C and back to 30 °C (test case identifier: TH-1 from Table 9.

An intermediary setpoint of 40 °C was included, and the temperature and viscosity measurement for this dataset was not continuous. Data was observed from 30 °C to 40 °C and then measurements were interrupted and a new measurement for the 40 °C steady state point was obtained. Similarly, measurements were obtained for 40 °C to 45 °C and the 45 °C steady state point. A measurement was also obtained once the temperature was decreased back to 30 °C. The averaged dynamic viscosity at the steady state temperatures are in Figure 53. It can be observed that viscosity remains within the absolute uncertainty when comparing the viscosity at 30 °C pre and post cycling, up to the maximum of 45 °C. The viscosities depicted in Figure 53 are tabulated in Table 23. Furthermore, it must be noted that condensation was observed on the underside of the low sample container, as depicted in Figure 54.

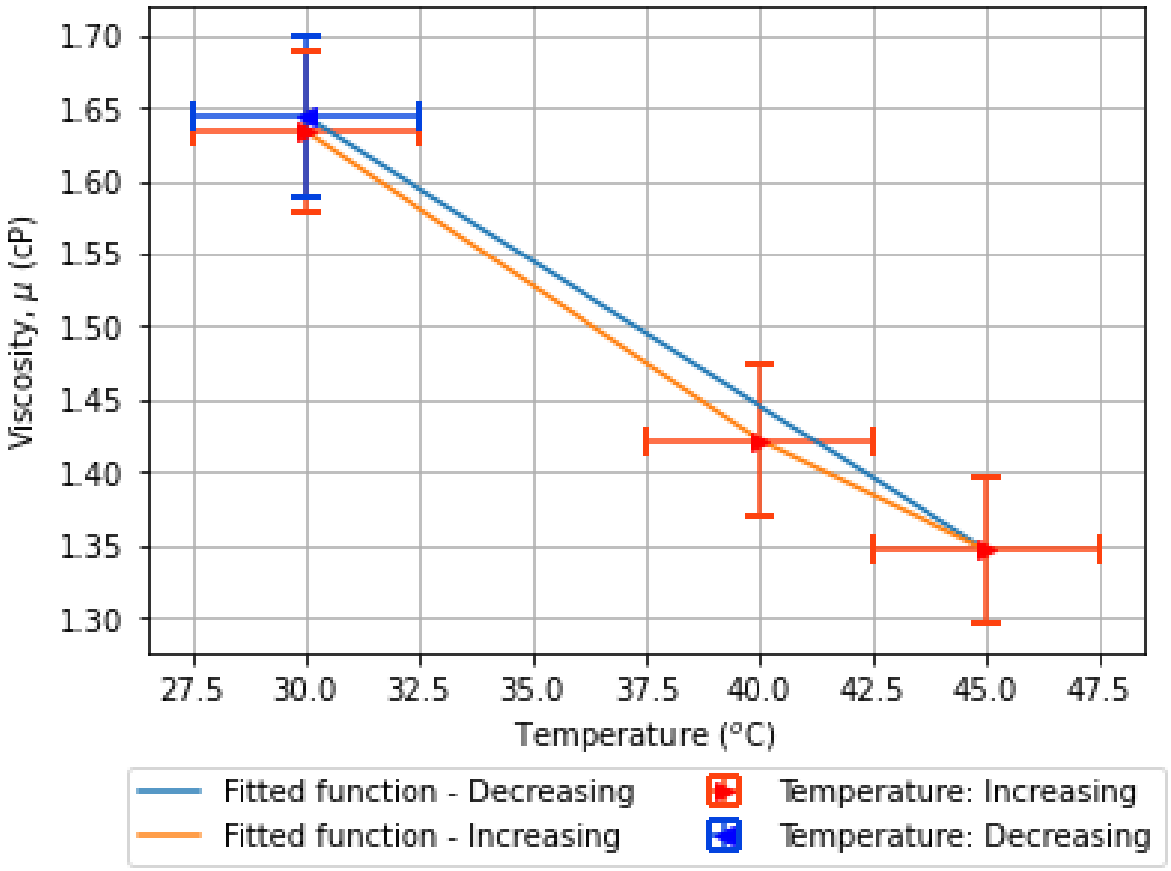

Figure 53: 1.58 g/dL Thermal Hysteresis Experiment: Maximum Temperature Setpoint: 45 °C. Viscosity converted into beaker equivalent using correction factor from method described in section 5.2.11

Table 23: Viscosities of 1.58 g/dL Thermal Hysteresis Experiment: Maximum Temperature Setpoint: 45 °C

Temperature (°C)	Viscosity (cP) – Increasing. ± 0.05	Viscosity (cP) – Decreasing. ± 0.05
30	1.63	1.64
40	1.42	N/A
45	1.35	N/A

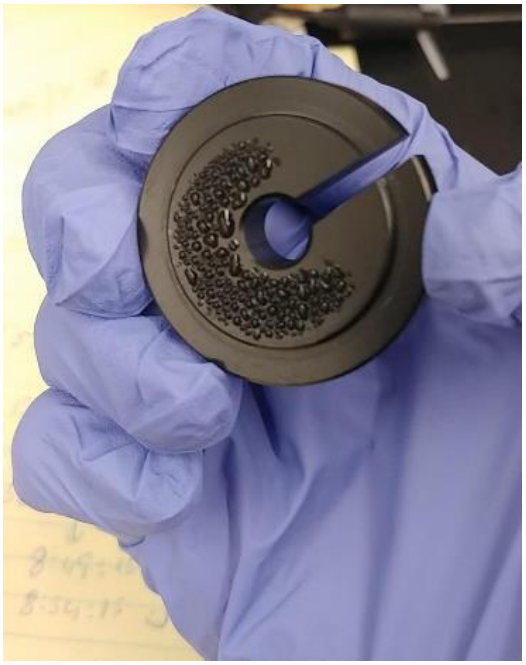

Figure 54: Condensation on the under side of the LSC lid after thermal hysteresis cycling - Max Temp Setpoint = 45 °C, Incremental

For the maximum hysteresis temperature of 60 °C, the viscosity of the 1.58 g/dL was measured from 30 °C up to 60 °C and back to 30 °C. Three observations, two of which were incremental (TH-2A, and TH-2B from per Table 9) and one of which were non incremental (TH-2C from Table 9), were performed. With regards to the first incremental thermal hysteresis experiment, besides the initial temperature setpoint of 30 °C and the maximum setpoint of 60 °C, three other intermediary setpoints were observed; specifically, temperature setpoints of 40 °C, 45 °C, and 50 °C, wherein 9 separate observations of increasing temperature, 4 transient and 5 steady state, as well as 8 separate observations of decreasing temperature, 4 transient and 4 at steady state were performed.

The total time taken for the experiment including all transient and steady state observations was 373 ± 1 min. The averaged dynamic viscosity at the steady state temperatures are in Figure 55 and tabulated in Table 24, where the viscosity for both increasing and decreasing temperatures remain within the absolute uncertainty.

Table 24: 1.58 g/dL Thermal Hysteresis Experiment: Maximum Temperature Setpoint: 60 °C Incremental #1. Viscosities tabulated include increasing and decreasing from 60 °C, as well as after cooldown to room temperature.

Temperature (°C)	Viscosity (cP) – Increasing. ± 0.05	Viscosity (cP) – Decreasing. ± 0.05	Viscosity (cP) – Increasing. After Cooldown ± 0.05
30	1.64	1.70	1.69
40	1.44	1.47	1.47
45	1.36	1.38	N/A
50	1.29	1.30	N/A
60	1.19	1.19	N/A

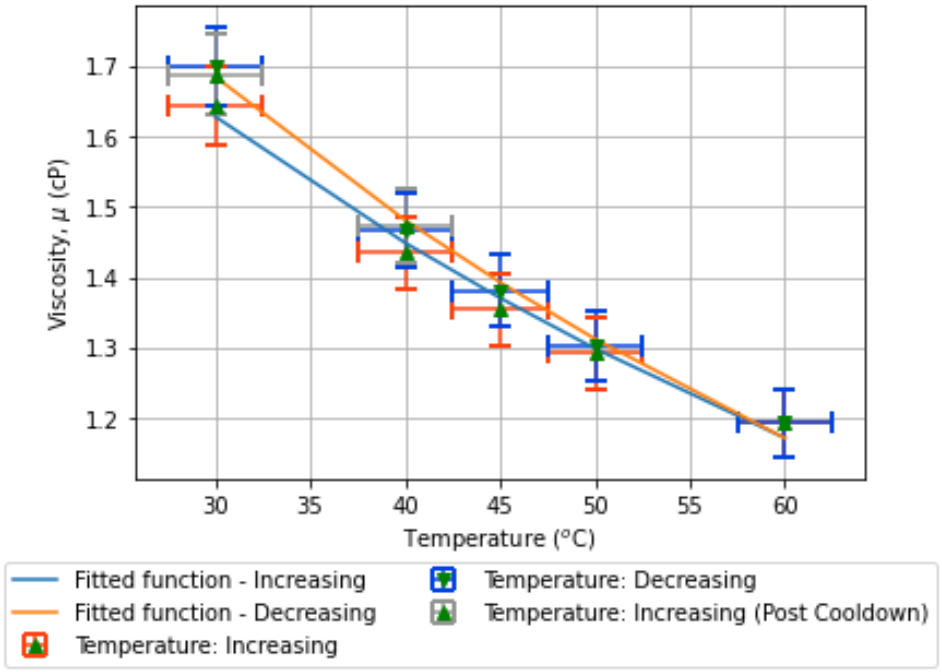

Figure 55: 1.58 g/dL Thermal Hysteresis Experiment: Maximum Temperature Setpoint: 60 °C Incremental #1. Viscosity converted into beaker equivalent using correction factor from method described in section 5.2.11

The mass of the sample was also observed to be 15.90 and 15.40 ± 0.01 g before and after temperature cycling respectively, equivalent to a mass difference of 0.5 ± 0.25 g. The large uncertainty of this mass difference (in addition to instrumental uncertainty) is attributed to wetting of the inner walls of the LSC and the spindle. In order to observe any lingering hysteresis effects induced via the thermal cycling, the viscosity of the solution was observed after approximately 17.67 +- 0.02 h of storage at room temperature conditions (test case identifier: TH-2A-II, as per Table 9) of approximately 24.5 ±1 °C; the results of the averaged dynamic viscosity after cooldown at steady state temperatures are tabulated in Table 24.

The second incremental thermal hysteresis experiment, TH-2B, was measured with intermediary setpoints of 40, 45 and 50 °C, in addition to the initial and final setpoints of 30 °C and 60 °C. However, unlike the first incremental thermal hysteresis experiment, transient and steady state temperature and viscosity were combined in one observation, with 5 observations of increasing temperature and 4 observations of decreasing temperature. The total time taken for the experiment was approximately 381 ± 1 min. The mass of the sample was measured, both before and after temperature cycling, and tabulated in Table 25. The averaged dynamic viscosity at the steady state temperatures are in Figure 56 and tabulated in Table 26, where it can be observed that the viscosity remains within the absolute uncertainty.

Table 25: Mass of 1.58 g/dL PVA Sol sample pre vs post thermal hysteresis cycling - Max Temp Setpoint = 60 °C, Increment #2

Observation Type:	Mass (± 0.01 g)
Pre-Thermal Hysteresis Cycling	20.17
Post-Thermal Hysteresis Cycling	19.87

A mass difference of 0.294 +- 0.25 g was observed from Table 25. The uncertainty (in addition to instrumental uncertainty) is attributed to wetting of the inner walls of the LSC and the spindle.

To minimize evaporative effects, the LSC of experiment TH-2B was lidded (using the lid provided by the manufacturer) and shimmed (a shim was placed on top of the lid to further reduce evaporation. The shim is necessary as the lid has a cut-out open to atmosphere so that it does not interfere with the spindle attached to the viscometer as seen in Figure 57. This resulted in the reduction of evaporated mass when comparing the first incremental dataset to the second; detailed in Chapter 7.

Table 26: 1.58 g/dL Thermal Hysteresis Experiment: Maximum Temperature Setpoint: 60 °C Incremental #2. Viscosities tabulated include increasing and decreasing from 60 °C, as well as after cooldown to room temperature.

Temperature (°C)	Viscosity (cP) – Increasing. ± 0.05	Viscosity (cP) – Decreasing. ± 0.05
30	1.65	1.66
40	1.43	1.44
45	1.34	1.35
50	1.27	1.28
60	1.1	N/A

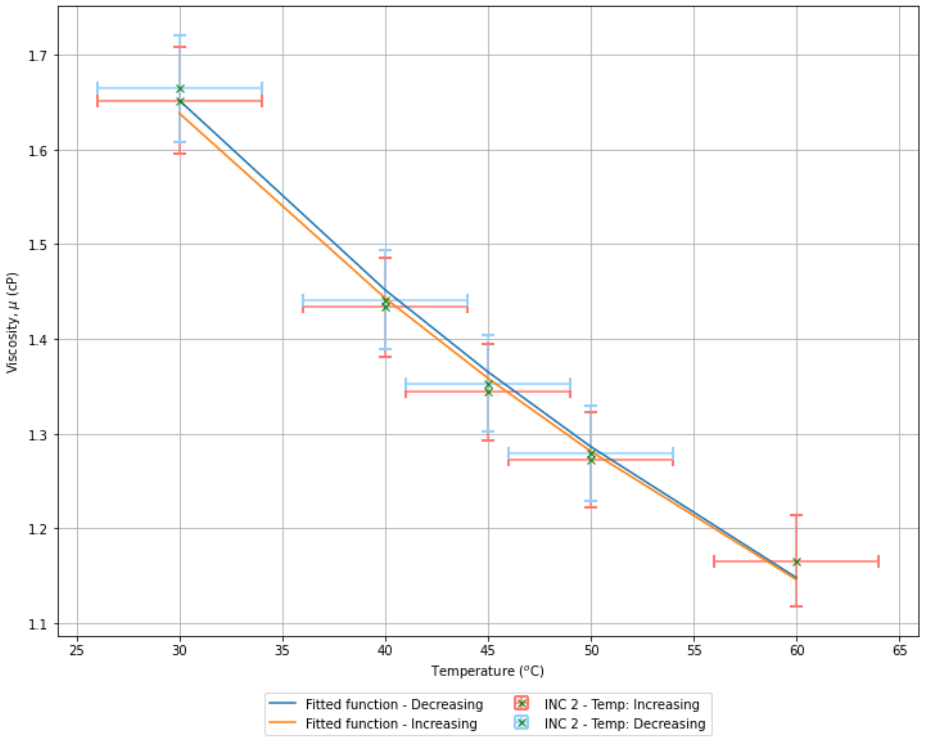

Figure 56: 1.58 g/dL Thermal Hysteresis Experiment: Maximum Temperature Setpoint: 60 °C Incremental #2. Viscosity converted into beaker equivalent using correction factor from method described in section 5.2.11

Figure 57: LSC lidded and shimmed to minimize evaporation; pre thermal hysteresis cycling - Max Temp = 60 °C, Increment #2

The non-incremental observation, TH-2C, with a maximum temperature of 60 °C was performed with the LSC lidded and shimmed to minimize evaporation. The total time taken for the experiment, including increasing to maximum temperature setpoint and decreasing temperature back to room temperature, was 141 ± 1 min.

The averaged dynamic viscosity at the steady state temperatures, and the mass of the sample, before and after temperature cycling are tabulated in Table 27. It can be observed that the viscosity remains within the uncertainty.

Table 27: Mass of 1.58 g/dL PVA Sol sample pre thermal hysteresis cycling - Max Temp Setpoint = 60 °C, Non-Incremental

Observation Type:	Mass (± 0.01 g)	Viscosity (cP) ± 0.05
Pre-Thermal Hysteresis Cycling	18.09	1.64
Post-Thermal Hysteresis Cycling	17.71	1.61

A mass difference of 0.37 ± 0.25 g was measured (Table 27) above; the uncertainty of which (in addition to instrumental uncertainty) is attributed to wetting of the inner walls of the LSC and the spindle.

For the maximum temperature of 75 °C, a viscosity of the 1.58 g/dL PVA solution was measured from 30 °C up to 75 °C and back to 75 oC. Two measurements performed were incremental and one was non incremental (TH-3A, TH-3B and TH-3C from Table 9). With regards to the first incremental thermal hysteresis experiment, TH-3A, besides the initial temperature setpoint of 30 °C and the maximum setpoint of 75 °C, seven intermediary setpoints of increasing temperature and five intermediary setpoints of decreasing temperature were observed.

Specifically, increasing temperature setpoints of 35, 40, 45, 50, 55, 60, and 65 °C, and decreasing temperature setpoints of 65, 60, 50, 45 and 40 °C, where 17 measurements of increasing temperature, 8 transient and 9 steady state, as well as 12 separate measurements of decreasing temperature, 6 transient and 6 at steady state were performed. The steady state dynamic viscosities increasing and decreasing from a maximum of 75 °C, as well as viscosities after cooldown to room temperature are tabulated in Table 28 and depicted in Figure 58.

Table 28: 1.58 g/dL Thermal Hysteresis Experiment: Maximum Temperature Setpoint: 75 °C Incremental #1. Viscosities tabulated include increasing and decreasing from 75 °C, as well as after cooldown to room temperature.

Temperature (°C)	Viscosity (cP) – Increasing. ± 0.05	Viscosity (cP) – Decreasing. ± 0.05	Viscosity (cP) – Increasing. After Cooldown ± 0.05	Viscosity (cP) – Decreasing. After Cooldown ± 0.05
30	1.66	1.79	1.60	1.66
35	1.54	N/A	N/A	N/A
40	1.45	1.54	N/A	N/A
45	1.38	1.45	1.35	1.3
50	1.31	1.37	N/A	N/A
55	1.26	N/A	N/A	N/A
60	1.22	1.25	N/A	N/A
65	1.18	1.20	N/A	N/A
75	1.11	N/A	1.07	N/A

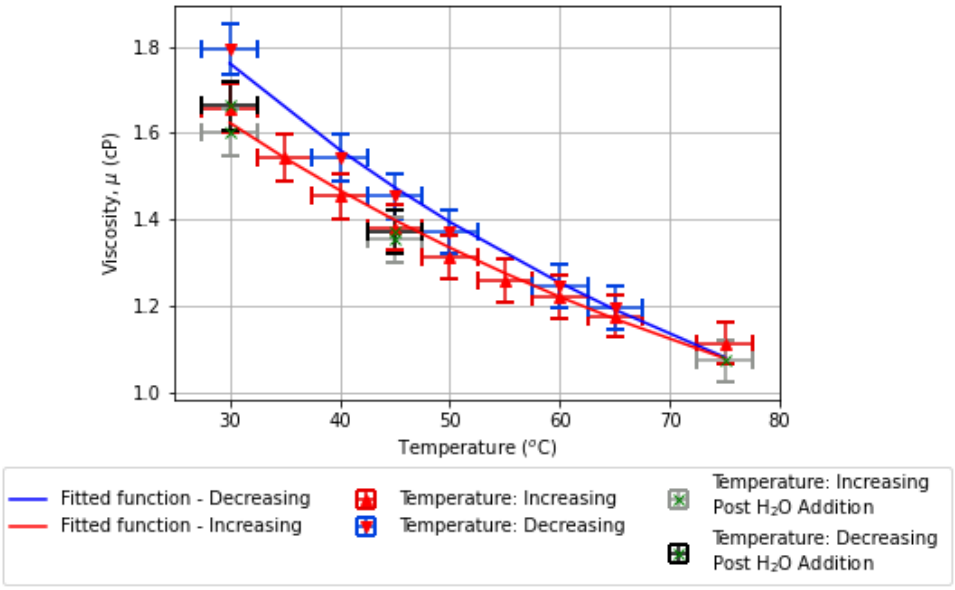

Figure 58: 1.58 g/dL Thermal Hysteresis Experiment: Maximum Temperature Setpoint: 75 °C, Increment #1. Comparison of viscosities before and after water addition. Viscosity converted into beaker equivalent using correction factor from method described in section 5.2.11

The total time taken for the experiment including all transient and steady state observations, was 660 min ± 1 min. From Figure 58 it can be seen that the averaged dynamic viscosity at 30 °C after temperature cycling is higher when compared to before. This is due to evaporation, as can be seen in Table 29.

Table 29: Mass of 1.58 g/dL PVA Sol sample pre vs post thermal hysteresis cycling - Max Temp = 75 °C, Increment #1

Observation Type:	Mass (± 0.01 g)
Pre-Thermal Hysteresis Cycling	17.76
Post-Thermal Hysteresis Cycling	15.53

A mass difference of 2.23 ± 0.25 g (Table 29) was calculated. The uncertainty (in addition to instrumental uncertainty) is attributed to wetting of the inner walls of the LSC and the spindle. This mass of water lost to evaporation was replaced dropwise into the LSC to 17.67 ± 0.01g and the viscosity at steady state setpoints at 30, 45 and 75 °C are measured as seen in Figure 58.

The averaged dynamic viscosities of steady state temperatures after the addition of water (the green datapoints with the grey and black uncertainty bars in Figure 58) returns within the absolute error bounds of viscosity before incremental thermal cycling. Comparing the viscosity before and after cycling up to 75 °C, after the addition of water, the viscosity remains within the absolute uncertainty.

The second incremental thermal hysteresis experiment with a maximum temperature setpoint of 75 °C was performed between the temperature of 30 °C and the maximum of 75 °C, with four intermediary temperatures. Specifically, 45 °C, 50 °C, and 60 °C measurements of increasing temperature, and 4 measurements of decreasing temperature were performed, and transient and steady state temperatures were observed together. The steady state viscosities are depicted in Figure 59 and tabulated in Table 30. The total time taken for the experiment including all transient, steady state and additional observations was 615 ± 1 min.

Table 30: 1.58 g/dL Thermal Hysteresis Experiment: Maximum Temperature Setpoint: 75 °C Incremental #2. Viscosities tabulated include increasing and decreasing from 75 °C, as well as after cooldown to room temperature.

Temperature (°C)	Viscosity (cP) – Increasing. ± 0.05	Viscosity (cP) – Decreasing. ± 0.05
30	1.65	1.69
45	1.37	1.39
50	1.30	1.31
60	1.18	1.19
75	1.08	N/A

The averaged dynamic viscosity at the steady state temperatures in Figure 59 show that the viscosity remains within the absolute uncertainty when comparing the viscosity of the second incremental experiment at 30 °C, before and after temperature cycling up to of 75 °C. It should be noted that the LSC was lidded and shimmed to minimize evaporative effects. The mass before and after temperature cycling of the second incremental experiment was tabulated in Table 31. A mass difference of 0.59 ± 0.25 g was observed.

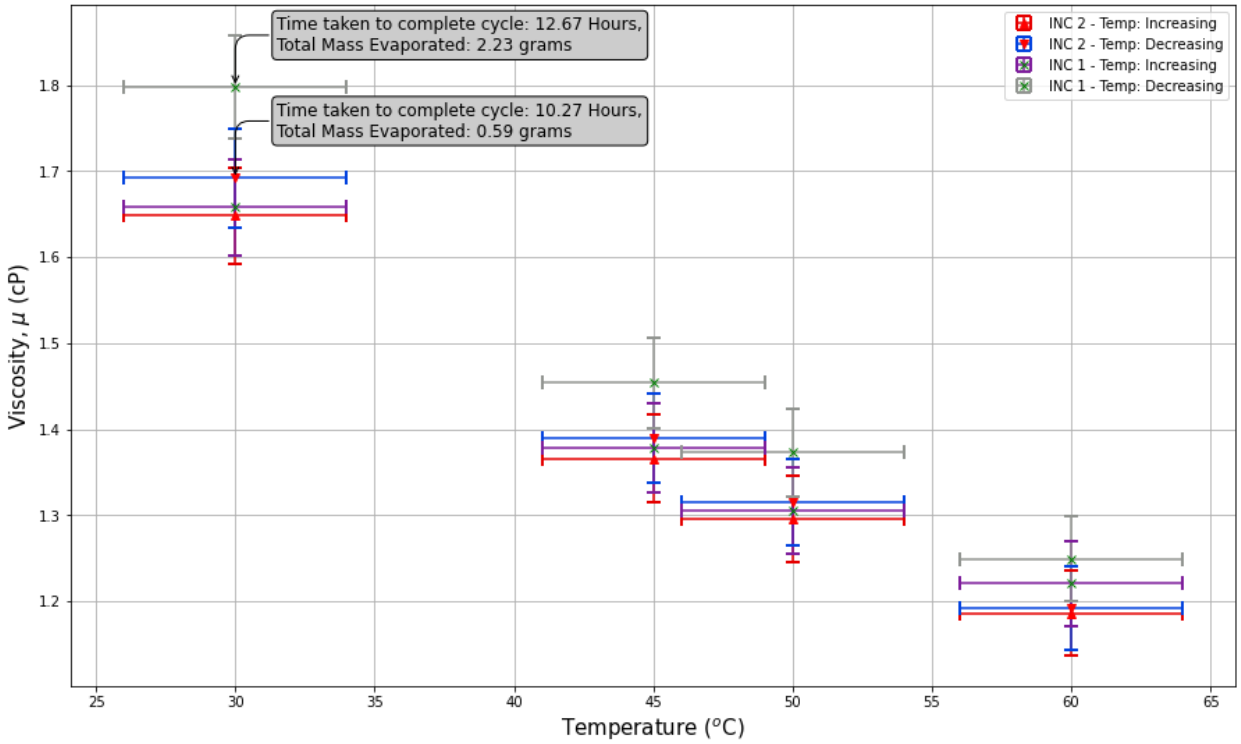

Figure 59: 1.58 g/dL Thermal Hysteresis Experiment: Maximum Temperature Setpoint: 75 °C, Increment #2. Comparison of Incremental 1 versus Incremental 2 viscosities.

Table 31: Mass of 1.58 g/dL PVA Sol sample pre vs post thermal hysteresis cycling - Max Temp Setpoint = 75 °C, Increment #2

Observation Type:	Mass (± 0.01 g)
Pre-Thermal Hysteresis Cycling	19.81
Post-Thermal Hysteresis Cycling	19.23

The third and final thermal hysteresis experiment at the maximum temperature setpoint of 75 °C, TH-3C, was non-incremental (and hence no intermediary temperature setpoints) and was both lidded and shimmed to minimize evaporation. The total time taken for the experiment, including increasing to maximum temperature setpoint and decreasing temperature back to room temperature, was 121.2 ± 1 min. Due to the non-incremental nature of this experiment, no steady state intermediary observations were available.

Although no intermediary setpoints are available, the mass and the viscosity at 25 °C, before and after temperature cycling up to 75 °C was measured and tabulated in Table 32. A mass difference of 0.26 +- 0.25 g was observed. The uncertainty of which (in addition to instrumental uncertainty) is attributed to wetting of the inner walls of the LSC and the spindle.

Table 32: Mass of 1.58 g/dL PVA Sol sample pre vs post thermal hysteresis cycling – Max Temp Setpoint = 75 °C, Non-Incremental

Observation Type:	Mass (± 0.01 g)	Viscosity (± 0.05 cP) at 25 °C
Before Thermal Hysteresis Cycling	17.04	1.77
After Thermal Hysteresis Cycling	16.78	1.84

6.2.5.3 Evaporation Rate

6.2.5.3.1 Experiment 1

In experiment #1, (test case identifier: EV-1A from Table 9) 60.22 g or 60 mL, of 0.16 wt% PVA solution was obtained for evaporation. Evaporation was performed by suctioning air through a bubbler column - pump type setup (detailed in section 5.2.9) for a total of 95.38 hrs, at an approximate flowrate of 0.1 litres per min. This resulted in the complete evaporation of water content and solidification of the remaining PVA. This was not the desired outcome.

6.2.5.3.2 Experiment 2

In this experiment (EV-1B-I, from Table 9), 50 mL or 49.3 g of 0.16 wt% PVA solution was evaporated over a total of 24 h at an approximate flowrate of 0.1 lpm. After 24 hrs, the mass was measured again and found to be 43.73 g with the total mass lost to evaporation being 5.57 g. It was expected more water would have been evaporated over 24 hrs but due to the low flowrate this was not the case. Based on the mass lost to evaporation and the flowrate, the rate of evaporation was calculated to be 0.23 g/hr.

Hence, bubbling was restarted to allow for more solution to evaporate, to measure a change in characteristics, if any exists, after evaporation and water addition. Bubbling was run for a period of 5 hrs at a flow rate of 0.5 lpm (EV-1B-II from Table 9). This mass decreased to 41.4 g, so the evaporation rate of 0.47 g/hr, and the combined total loss of 7.91 g of water. After the evaporation of 7.91 g, water was added to return the mass of the solution to the 49.3 g, prior to evaporation. After thorough mixing, a portion of the contents were poured into the small sample container of the viscometer, and the viscosity was measured and compared to the viscosity of the 0.16 wt% solution.

The averaged dynamic viscosity after evaporation was found to be 1.63 cP, compared to the averaged dynamic viscosity pre-evaporation, determined to be 1.625 cP. These two viscosities are within the error and hence the same. The viscosity of the solution after evaporation but before the addition of water was not measured.

6.2.5.3.3 Experiment 3

In order to observe the viscosity after evaporation, but before water was added, this experiment (EV-1C from Table 9) was conducted. In this experiment, 54.6 g of 0.16 wt% PVA solution was evaporated over a total of 21.03 hrs, at an approximate flowrate of 0.4 – 0.5 lpm. After evaporation, the total mass lost to evaporation was calculated to be 9.73 g at a rate of evaporation of 0.46 g/hr. A portion of the evaporated solution was extracted for viscosity measurements.

The averaged dynamic viscosity was measured to be 1.97 cP. Comparing this viscosity to the average viscosity of 0.16 wt% PVA solution before evaporation, measured to be 1.625 cP, viscosity increased by 0.34 cP. Substituting the viscosity post evaporation into x, from the trendline equation for the viscosity versus concentration plot in Figure 60, the concentration of the PVA solution, after evaporation was calculated to be 0.017 w/w%, as per Equation 56:

$$y = 0.7246e^{56.72x} \rightarrow \frac{\ln\left(\frac{1.96}{0.724}\right)}{56.72} = x \rightarrow x = 0.0176\frac{g}{mL} = 0.17\frac{w}{w}\% \quad \text{Equation 56}$$

The data in Figure 60 was measured at room temperature (approximately 23 °C), whereas the viscosity data for Experiments #2 and #3 was measured at 30 °C. Due to this, the calculated concentration of 0.17 w/w% in Equation 56 must only be used as an approximate of the viscosity.

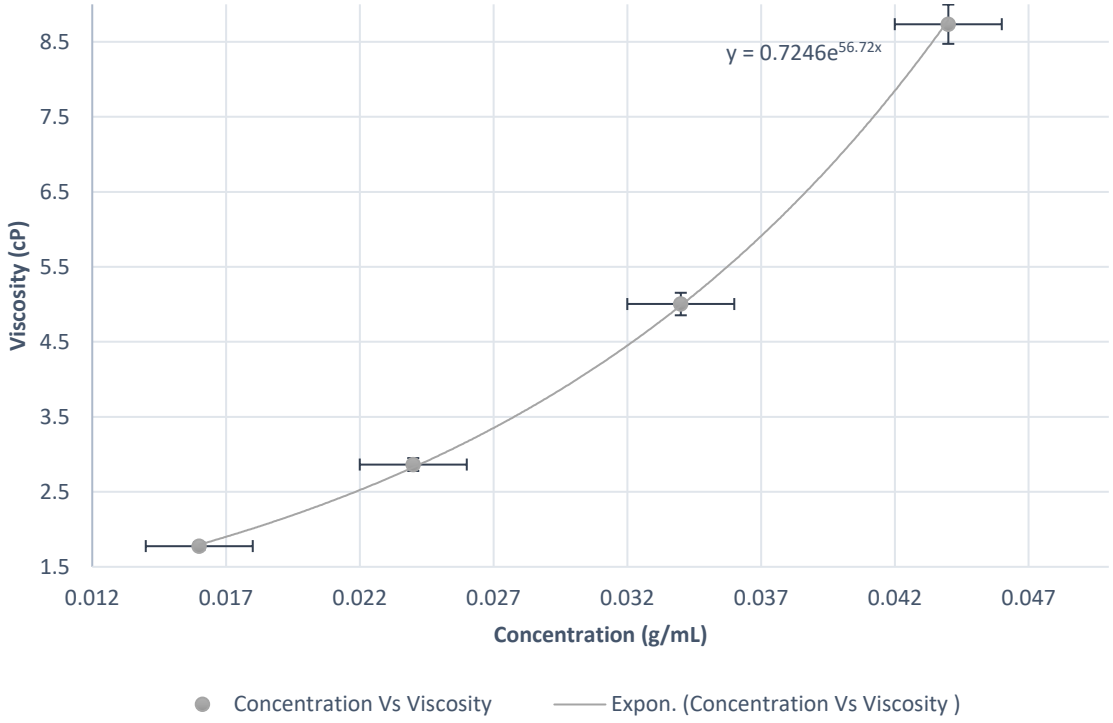

Figure 60: PVA Solution Viscosity as A Function of PVA Solution Concentration

6.2.5.4 pH

The pH for concentrations of PVA solutions were found to be acidic as a function of concentration, tabulated in Table 33:

Table 33: pH of various concentrations of PVA solutions at ambient temperatures

Concentration (w/w%)	Concentration (g/dL; Absolute)	pH (± 0.01)	Temperature (± 1 °C)	Test Case Identifier (As per Table 8)
24	2.4	5.37	22.5	pH-4A
34	3.4	5.39	22.4	pH-4B
44	4.4	4.53	21.8	pH-4C

From Table 33, it can be observed that the acidity of the PVA solutions increases with increasing PVA concentration, from a pH of 5.37 at a concentration of 2.4 g/dL to a pH of 4.53 at a concentration of 4.4.

7 Discussion

The purpose of this chapter is to interpret the characterization results of the various constituents including their effects on viscosity (the primary characteristic), as well as interpretation of how constituents, based on characterization results, effect gels and gel types.

7.1 Constituent Impact on Viscosity

7.1.1 Borax-Fructose Solution

The results from density and viscosity characterization of varied concentrations of borax-fructose solutions have been detailed in section 6.2.2, where, as per Figure 45 and Figure 46, an increasing trend in density (Figure 45) and averaged viscosity (Figure 46), as a function of increasing concentration were, respectively, observed.

Comparing the results of viscosity as a function of increasing borax concentration of borax-fructose solutions (Figure 46), to the viscosity results of the individual constituents (before combining), borax (Figure 38) and Fructose (Figure 43), respectively, allows for the validation of an important phenomenon; that phenomenon being that Fructose chemically interacts with borax, as per the theory discussed in sub-section 4.1.2. Figure 61, provides a comparison of the results of viscosity as a function of increasing concentration of the various constituent and combined constituent solutions:

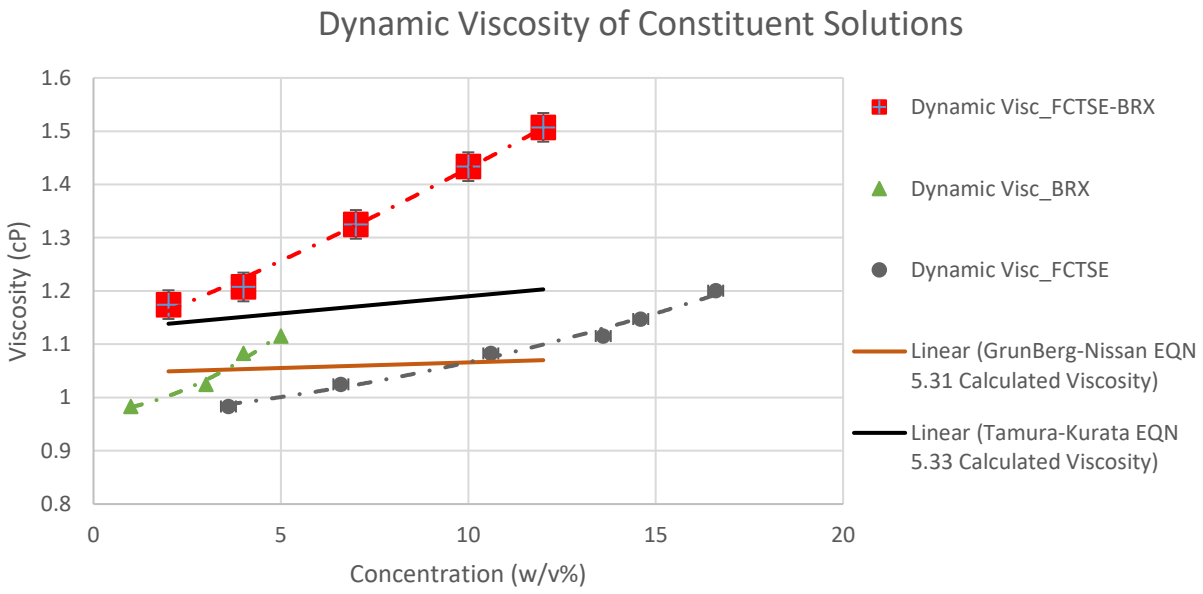

Figure 61: Average Dynamic Viscosity Plot of Fructose, Borax and Borax-fructose Solutions of Varied Concentrations

The viscosity of mixtures cannot exceed the viscosity of the most viscous constituent. In this case, borax is the most viscous constituent, and from Figure 61, when comparing the dynamic viscosity of borax to that of Fructose at the same w/v% concentrations, borax is higher. The Grunberg-Nissan and the Tamura-Kurata theoretical correlations (detailed in section 4.1.2.3 and depicted in Figure 61) were used to validate the interaction between fructose and borax.

Comparing the experimentally determined viscosity to Grunberg-Nissan (solid orange line in Figure 61) and the Tamura-Kurata (solid black line in Figure 61) correlations, the Tamura-Kurata correlation is within 12% difference of the experimentally determined viscosity, whereas the difference between the experimental and Grunberg-Nissan values are as large as 21%. The Tamura-Kurata correlation with the 12% difference, confirms the hypothesis that fructose does in fact complex with the borax. Specifically, since the resulting theoretically predicted viscosity is much higher than the viscosities of the individual constituents. If no interaction had occurred, the resulting viscosities would not have exceeded the viscosity of the most viscous constituent as would have been the case if the experimental data was in agreement with the Grunberg-Nissan correlation.

In addition to the verification through the Tamura-Kurata correlation, the borax-fructose interaction was also verified by Xia et al, through the use of liquid chromatography and orbital mass spectrometry analysis [114]. In this work, the interaction was validated using the pH measurements

of the various borax-fructose solutions, relative to the individual constituents before combining. As discussed in section 6.2.4.3, the pH of borax solutions are relatively alkaline with a pH of 9. On the other hand, fructose solutions are neutral. When 13.6 w/v% fructose is in the presence of 2 w/v% borax, an acidic pH of 4.55 is the result. This phenomenon was expressed in Equation 9 and Equation 10 in sub-section 4.1.2.1 which expresses the overall protonation of the environment. This was experimentally observable from Figure 47 in section 6.2.4.3. This observable protonation is the by product of the borax-fructose complexation hypothesized in sub-section 4.1.2.1.

Due to this borax-fructose complexation, the multi equilibria reaction is driven further to the right (section 4.1.2) allowing for the addition of borax beyond the solubility limit of 5 w/v% [98]. As the concentration of borax is increased, the concentration of boric acid increases accordingly. However, a portion of this boric acid is consumed by complexation with fructose. This results in a relatively higher concentration of tetrahydroxyborate ions (Equation 6 from section 3.2). As the relative concentration of tetrahydroxyborate ions increases with increasing borax concentration, the pH is driven back to a relatively neutral environment, with a pH of 7.23 at a borax concentration of 10 w/v%.

A constant concentration of 13.6 w/v% fructose was maintained when combining constituents, as well as when manufacturing gels. The hypothesis that increasing fructose concentration results in the increased viscosity of gels when constituents are combined cannot be verified. Nonetheless, the literature indicates both possibilities [74]. Specifically, when fructose concentration is increased, complexing with borate, due to the anionic environment, results in an increase in hydrophilicity, which then increases the interactions with the hydrophilic PVA monomers. The monomers are capable of crosslinking [74], resulting in an increase in viscosity. Alternatively the literature also indicates at the possibility of reaching a threshold concentration after which fructose can compete with PVA for interactions with borate ions [74]. This results in an increased concentration of doubly coordinated fructo-borate complexes [74] (section 4.1.2), and a reduction in viscosity.

7.1.2 PVA Solution

The results from density and viscosity characterization of varied concentrations of PVA solutions have been detailed in section 6.2.5, where an increasing trend in density (Figure 48) and averaged viscosity (Figure 49), as a function of increasing concentration were observed.

The increasing density and viscosity as a function of PVA concentration and based on the borax-PVA theory discussed in section 4.1.1, a similar increase in density and viscosity when combined with other constituents for purposes of gelation, can be expected. Furthermore, an increase in PVA concentration allows for the presence of more 1-2 diols, which increases the concentration of crosslinking, and in turn, as seen in the literature [147], results in the increase of viscosity.

7.1.2.1 Thermal Hysteresis

7.1.2.1.1 45 °C

Thermal hysteresis characterization was performed using various concentrations of PVA solution with various maximum temperatures. The purpose was to observe any glass transition behaviour, any temperature related viscosity changes, as a result of thermal hysteresis effects. From Table 23 and Figure 53, it can be seen that viscosity decreased as a function of increasing temperature; and conversely, increased as a function of decreasing temperature. No dramatic changes in viscosity were apparent after the temperature returned to the initial thermal setpoint with the viscosity after thermal cycling within the error and, as such, viscosity does not suffer a permanent change.

7.1.2.1.2 60 °C

The second batch of experiments consisted of a maximum temperature setpoint of 60 °C. From Figure 55 and Table 24, it can be seen that viscosity decreased with increasing temperature and increased with decreasing temperature; results of this thermal run tabulated in Table 24, were used to develop the viscosity trendlines depicted within Figure 55. With regards to the trendlines used to describe the apparent viscosity of the 1.58 g/dL PVA solution as a function of temperature, a number of relationships could be used.

The Arrhenius relationship describes the effect of temperature on the apparent viscosity for Newtonian as well as constant shear rate power law fluids [148]. To describe the thermal hysteresis trendlines of PVA solutions in this work a multi parametric model that combines the Arrhenius relationship with additional parameters was used. The multi parametric model is described in Equation 57 [148]:

$$\eta = A_o * \dot{\gamma}^{n-1} * e^{(B*C+\frac{E_a}{RT})} \quad \text{Equation 57}$$

As can be seen from Equation 57, the $\dot{\gamma}$ variable accounts for shear rate, and the C variable accounts for the concentration of constituent of the sample fluid. Variables A_o, B, and E_a, are determined using multiple regression analysis based on experimental viscosity and temperature data [149]. These variables are defined under Appendix section 11.3.4, which also includes the values for some of these variables. The variable n represents the flow behaviour index where a value of $n < 1$ is indicative of shear thinning behaviour, $n > 1$ is indicative of shear thickening behaviour and $n = 1$ is indicative of Newtonian behaviour [150]. The flow behaviour index was determined by plotting the $\log_{10}$(Shear Stress) vs $\log_{10}$(Shear Rate). The slope of the linear line of best fist is equivalent to n [151].

The multiple regression model expressed in Equation 57, was used to develop the thermal hysteresis trendlines of PVA solutions with maximum temperatures of 60 and 75 °C. For the first incremental experiment with a maximum temperature of 60 °C, trendlines (Figure 55) found to best correlate increasing and decreasing viscosity-temperature profiles were:

$$y = 0.0079 * \left(122.3^{(0.9686-1)}\right) * e^{((1.1407*1.6)+(\frac{9.2}{(0.0083)*(273.15+x)}))} \quad \text{Equation 58}$$

$$y = 0.0075 * \left(122.3^{(0.9686-1)}\right) * e^{((0.9574*1.6)+(\frac{10.16}{(0.0083)*(273.15+x)}))}$$ Equation 59

The viscosity of the solution was also measured after approximately 17.67 +- 0.02 hrs of storage at room temperature condition (test case identifier TH-2A-II, as per Table 9), in order to determine if any thermal hysteresis variation in viscosity occurs post interim storage at ambient conditions; results of 1.69 cP at 30 °C and 1.47 at 40 °C, (Table 24) were compared to 1.70 cP at 30 °C and 1.47 cP at 40 °C during cooldown, and reveal no significant difference in comparison to all comparative values within the uncertainty.

The averaged dynamic viscosity of the second incremental and discontinuous experiment, (TH-2B, from Table 9) with a maximum setpoint of 60 °C is depicted in Figure 56 and tabulated in Table 26. It can also be seen that viscosity decreased as a function of increasing temperature and increased as a function of decreasing temperature. The multiple regression model expressed in Equation 57, was used to develop the thermal hysteresis trendlines of Figure 56, with equations of:

$$\mathrm{y} = 0.0068 * \left(122.3^{(0.9686-1)}\right) * e^{((1.0387*1.6)+(\frac{10}{(0.0083)*(273.15+x)}))}$$ Equation 60

$$\mathrm{y} = 0.0074 * \left(122.3^{(0.9686-1)}\right) * e^{((0.9462*1.6)+(\frac{10.17}{(0.0083)*(273.15+x)}))}$$ Equation 61

Equation 60 and Equation 61 were found to best correlate increasing and decreasing viscosity - temperature profiles respectively, for the second incremental experiment with a maximum temperature of 60 °C.

7.1.2.1.3 75 °C

The third batch of thermal hysteresis experiments were to a maximum temperature setpoint of 75 °C. Three experiments were run in total. The averaged dynamic viscosities of the first incremental and discontinuous experiment, TH-3A, is depicted in Figure 58 and tabulated in Table 28. The viscosity decreased as a function of increasing temperature and increased as a function of decreasing temperature. The multiple regression model expressed in Equation 57 was used to develop the thermal hysteresis trendlines of Figure 58, with equations of:

$$y = 0.0046 * \left(122.3^{(0.9686-1)}\right) * e^{((1.7757*1.6)+(\frac{7.97}{(0.0083)*(273.15+x)}))} \quad \text{Equation 62}$$

$$y = 0.0093 * \left(122.3^{(0.9686-1)}\right) * e^{((1.0079*1.6)+(\frac{9.5}{(0.0083)*(273.15+x)}))} \quad \text{Equation 63}$$

Equation 62 and Equation 63 were found to best correlate increasing and decreasing viscosity - temperature profiles respectively, for the first incremental experiment, with a maximum temperature set point of 75 °C.

An increase in viscosity after decreasing temperatures back to 30 °C was observed. Specifically, viscosity at 30 °C after cooldown from 75 °C (1.79 cP) was found to be outside the bounds of uncertainty (± 0.06) relative to the original viscosity at 30 °C of 1.66 cP. Although an increase in viscosity is observed, it must also be noted that significant mass loss, equivalent to 2.23 ± 0.25 g was also observed. To determine if the increased viscosity was due to evaporation or a combination of evaporation and hysteresis, the viscosity of the solution was measured after adding water to replace the mass loss. The temperature was then cycled again to a maximum of 75 °C, with only two intermediary setpoints at 30 °C and 45 °C. Similar to the first thermal cycling, the viscosity decreased as a function of increasing temperature and increased as a function of decreasing temperature. The resulting viscosities of 1.6 cP at 30 °C and 1.35 cP at 45 °C, during increasing temperature compared to viscosities measured during the original temperature cycling (as per 30 °C and 45 °C rows of Table 28) reveal no significant difference, with comparative values within uncertainty of one another.

The averaged dynamic viscosities of the second non-incremental and discontinuous experiment with a maximum temperature of 75 °C, TH-3B, as per Table 9, is depicted in Figure 59 and tabulated within Table 30. The viscosity decreased as a function of increasing temperature and increased as a function of decreasing temperature. Results of this thermal run (Table 30) were used to develop the correlations in Figure 62:

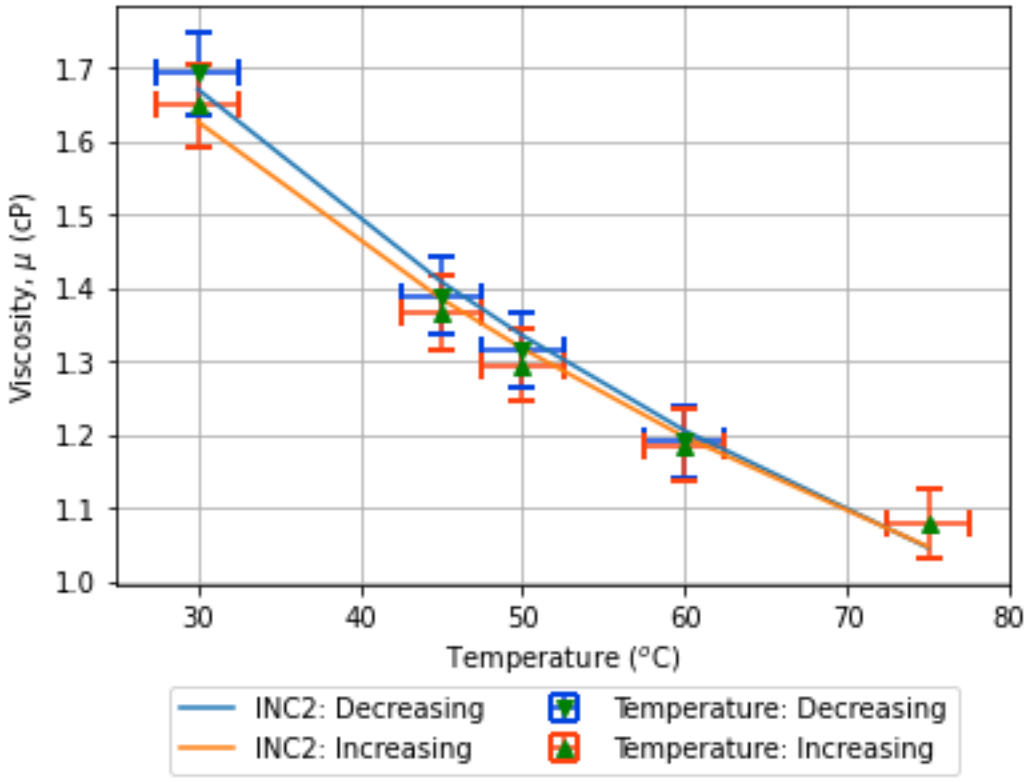

Figure 62: Thermal viscosity hysteresis experiment #2 – 75 °C Maximum Thermal Setpoint; Correlating Trendlines.

Discussion

The multiple regression model expressed in Equation 57, was used to develop the thermal hysteresis trendlines with equations of

$$y = 0.0159 * \left(122.3^{(0.9686-1)}\right) * e^{((0.8597*1.6)+(\frac{8.5468}{(0.0083)*(273.15+x)}))} \quad \text{Equation 64}$$

$$y = 0.0109 * \left(122.3^{(0.9686-1)}\right) * e^{((0.9757*1.6)+(\frac{9.1131}{(0.0083)*(273.15+x)}))} \quad \text{Equation 65}$$

Equation 64 and Equation 65 were found to best correlate increasing and decreasing viscosity - temperature profiles respectively, for the second incremental experiment with a maximum temperature set point of 75 °C.

7.1.2.2 Non-Newtonian Behaviour

The viscosity of PVA solutions of different concentrations was observed as a function of shear rate. The results show viscosity decreases as a function of increasing shear rate. A more intuitive method of observing non-Newtonian behaviour is by determining the flow behaviour index by plotting $\log_{10}$(Shear Stress) vs $\log_{10}$(Shear Rate) as discussed in section 7.1.2.1.2. Table 34 details Shear Stress, Shear Rate, $\log_{10}$(Shear Stress), and $\log_{10}$(Shear Rate) measured during experiments which produced Figure 50 - Figure 52 (the figures which represent non Newtonian observations).

Table 34: Rheological Parameters from Non-Newtonian Experiments on PVA solutions of varied concentrations

Concentration (g/dL)	Shear Rate (SR)	Log_{10}(SR)	Shear Stress (SS)	Log_{10}(SS)
1.6	122.3	2.09	4.34	0.64
1.6	73.38	1.87	2.58	0.41
1.6	61.15	1.79	2.16	0.33
1.6	36.69	1.56	1.35	0.13
3.4	36.69	1.56	5.39	0.73
3.4	24.46	1.39	3.61	0.56
3.4	14.68	1.17	2.24	0.35
3.4	12.23	1.09	1.88	0.27
3.4	7.338	0.87	1.15	0.06
4.4	14.68	1.17	4.81	0.68
4.4	7.34	0.87	2.47	0.39
4.4	3.67	0.56	1.28	0.11

Values in Table 34 were used to develop Figure 63 where 3 lines of best fit are shown. The blue coloured line with square datapoints depict 1.6 g/dL PVA solution (NN-1A, as per Table 8), the orange coloured line with triangle datapoints depict 3.4 g/dL PVA solution (NN-1B), and the grey coloured line with circular datapoints depict 4.4 g/dL PVA solution (NN-1C).

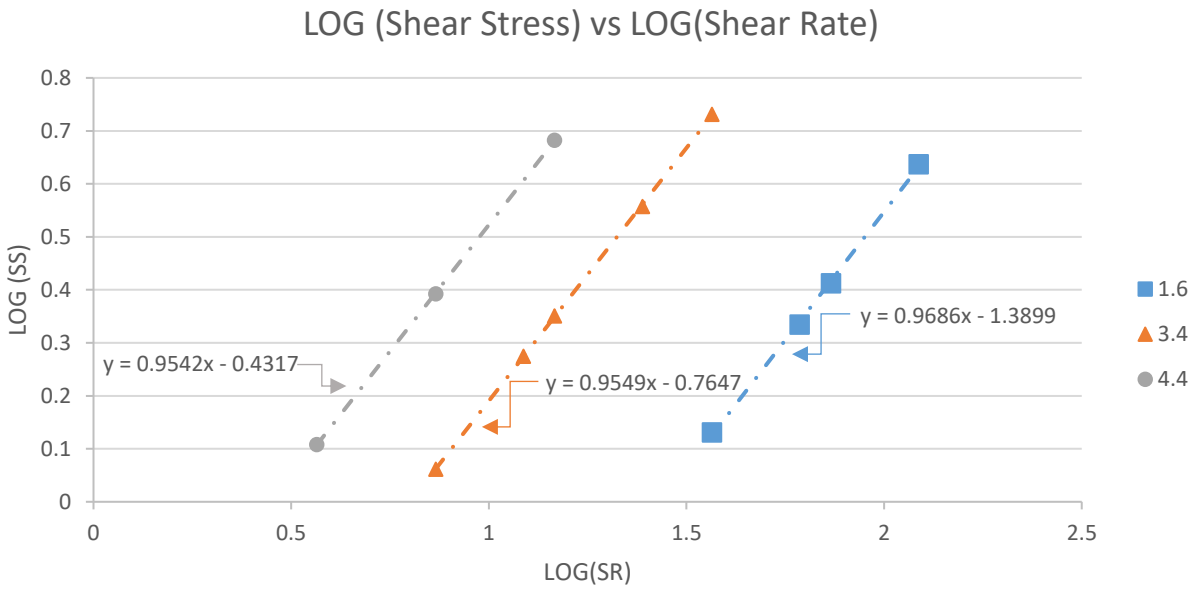

Figure 63: Log (Shear Stress) Vs Log (Shear Rate) Plot to Determine Flow Behaviour Index, n.

The slopes of the linear lines of best fit from Figure 63, represents n [151], with values of 0.96, 0.95, and 0.95 ± 0.05; representative of 1.6 g/dL, 3.4 g/dL and 4.4 g/dL PVA solutions'. Given that these values are all n<1, it is indicative of shear thinning behaviour.

7.1.2.3 Evaporation Rate

Based on the results of evaporation experiment #3, (test case identifier EV-1C, as per Table 9), the viscosity was initially found to be 1.625 cP, and after running the experiment, but prior to adding water, the viscosity was observed to be 1.97 cP. After adding water equivalent to the mass lost, the viscosity returned to 1.62 cP. This indicates that evaporation results in only the loss of the water content of the PVA solution, while the constituent contents remain *in-situ*, and this has implications when considering PVA solutions and gels for the capture and storage of wastes. Specifically when gels are used for the capture and storage of wastes, evaporation can be used to drive off excess water content while retaining the captured wastes within the gel structure.

7.2 Preliminary Gel Manufacturing

To understand some of the issues with the gelation process, gels were manufactured based on a pre-existing laboratory procedure, as described in section 5.2.6. This resulted in a de-mixed gel, with two distinct components. One of the components was a relatively "hard" gel and the other component was a clear liquid, as can be seen in Figure 64.

Similar to the results above, manufacturing a gel using a 30% higher fructose concentration also resulted in a de-mixed gel, as can be seen in Figure 65. A 30% higher fructose concentration was attempted because it was believed that a protonation of the environment (section 4.1.2) could prevent a localized high concentration of crosslinking. This gel was observed to be extremely elastic, as seen in Figure 66.

A third attempt at manufacturing gels with the assistance of Dr. Sunagawa yielded a homogeneous gel, as desired. As can be seen in Figure 67, there are no distinct components but rather a homogeneous gel/slime like substance. It must be noted that with regards to the successful attempt depicted in Figure 67 a key step in the way the borax-fructose and the PVA solutions were combined was different (as per the new procedure described in section 5.2.6). Furthermore, the concentrations of constituents were different as well.

The key takeaway from the results of these experiment is the fact that characterization of the individual constituents and an understanding of the chemistry of how the constituents interact is important to be able to manufacture homogeneous gels of the same characteristics successfully and repeatedly. The new procedure was developed based on this understanding as detailed within in the next section. characterization of the individual constituents and the fact that borax and PVA act as crosslinking agents.

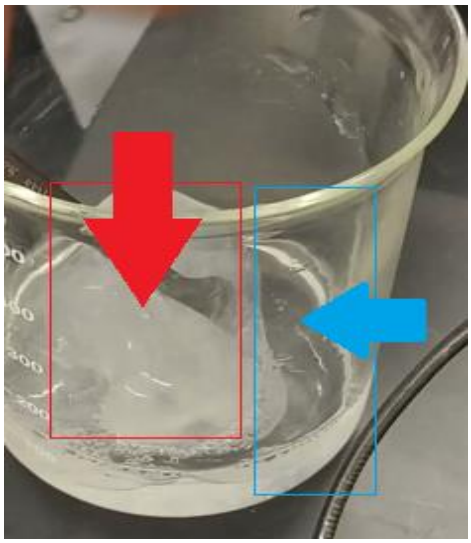

Figure 64: Image of Demixed Gel; No changes to the procedure

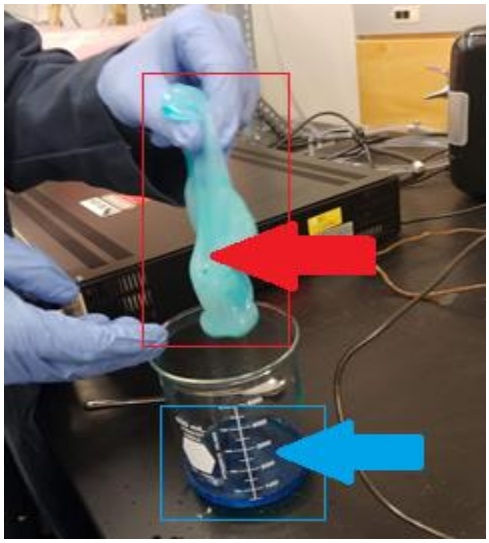

Figure 65: Image of Demixed Gel; 30% Increase in Fructose Concentration

Figure 66: Image of Demixed Gel; 30% Increase in Fructose Concentration; High elastic properties observed

Figure 67: Successful attempt at manufacturing gel; Borax-fructose Sol Added Drop Wise to PVA

7.3 Constituent Impact on Gel Types

The initial acidification of the environment that occurs due to fructose interacting with the added borax (Table 20), was predicted as per the borax-fructose interaction theory discussed within section 4.1.2. As the concentration of borax is increased to 10 w/v%, the aqueous environment becomes more alkaline, as discussed in section 7.1.1, eventually resulting in a pH of 7.23 ±0.01. In terms of gelation, an environment greater than a pH of 7 and less than a pH of 11 is ideal for the formation of stable gels, specifically, di-diol crosslinking [118].

It must be noted, however, that the pH of the various PVA solutions are relatively acidic, and as such, after the combination of aqueous borax-fructose constituent with the PVA solution, the pH of the overall environment returns to being relatively acidic (which is especially true for Type I gels, with a relative borax-fructose concentration of 3.85 w/w% concentration (Table 36). Nonetheless a sol to gel transition is enabled and gelation still occurs albeit one of a less stable, mono diol crosslink [118].

Due to borax-fructose solution having a relatively alkaline pH (Table 20) compared to PVA solution (Table 33), intuitively, a hypothesis of a relatively more alkaline environment after the increment of the relative concentration of the borax constituent of borax-fructose solution, was expected. However, comparing pH results of Type I and Type II 1.58 g/dL and 2.37 g/dL gels (Table 35), it was evidenced that a higher relative concentration of borax-fructose solution resulted in a more acidic environment.

Table 35: pH of 1.58 and 2.37 g/dL Type I and Type II gels

Gel Type	PVA Concentration (g/dL)	pH (± 0.01)
Type I	1.58	7.97
Type II	1.58	7.69
Type I	2.37	7.62
Type II	2.37	7.30

Initially, as PVA and borax constituents are combined, boric acid species are consumed through the formation of crosslinks with PVA, as described by PVA-borax crosslinking theory #2 under section 4.1.1.2. This consumption of boric acid results in the relative excess of tetrahydroxyborate ion, and as such, the pH of the overall environment is driven to an alkalinity greater than the pH of borax-fructose solution before combining with PVA. It must be noted that this alkalinity is further evidence of boric acid species, rather than tetrahydroxyborate ion species that is responsible for crosslinking with PVA. If it were the tetrahydroxyborate ion species associated with crosslinking, an acidic, rather than an alkaline environment would have resulted due to the hypothetical consumption of tetrahydroxyborate ion species, which inadvertently would have caused the excess of boric acid.

Similar to the protonation that occurs when borax interacts with fructose, a protonation of the environment when the relative concentration of borax-fructose constituent for gel manufacturing is increased, occurs, as seen in Table 35.

Figure 68 provides a visual depiction of the protonation that occurs when boric acid crosslinks with PVA. The release of hydronium occurs with both Type I and Type II gels. However, Type II gels, with a relatively higher borax-fructose concentration of 11.54 w/v% (compared to 3.85 w/v% for Type I gels), provides for increased boric acid crosslinking species. The increased presence of boric acid results in additional crosslinks to form. As more crosslinking occurs, more hydronium ions are generated.

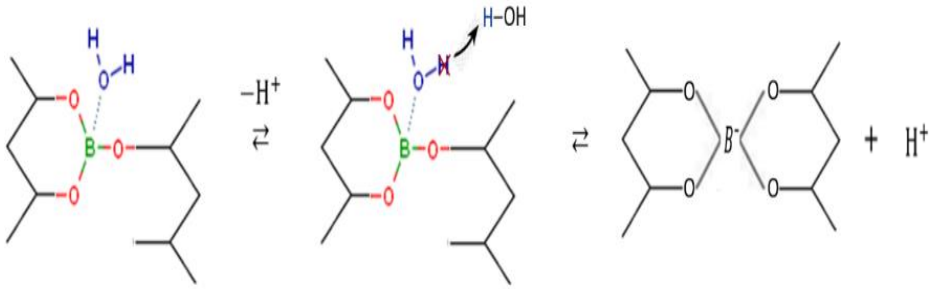

Figure 68: Protonation as a result of boric acid crosslinking with PVA

Additional cross link formation is experimentally evidenced via preliminary analysis of Stokes Law experiments, wherein, 2.37 g/dL PVA-Type I gels were compared to 2.37 g/dL PVA-Type II gels. The increment of borax-fructose from 3.85 to 11.54 w/w% results in a relatively higher viscosity. The results of preliminary analysis of Stokes Law experiments are depicted in Figure 69 where both photos were captured 10 seconds after the metal sphere reached the 45 mL mark. Comparing Figure 69-A to Figure 69-B, it can be seen that the metal sphere travels slower (slower velocity) within the Type II gel compared to Type I. This indicates a higher viscosity, according to Stokes Law, and is consistent with an increase in boric acid crosslinking agent and a relatively alkaline pH which results in an environment more favourable for di-diol crosslinking, or at the least, more crosslinking overall.

Type I gels (Table 36) are easier to manipulate due to their lower viscosity, while also having high qualitatively observable surface tension. As such, 16 w/w% PVA type I gels or alternatively even PVA solutions of various concentrations (Table 5), can be incorporated in liquid and gaseous waste capture system designs. The 34 w/w% PVA Type I gel can be used for adhesion surface decontamination. After waste capture applications, gels can be converted into Type II gels, by increasing the relative concentration of borax-fructose, and if necessary, by increasing the concentration of PVA solution to achieve significantly higher viscosities. This can result in a rubbery solid type gel, similar to the depiction within Figure 1.

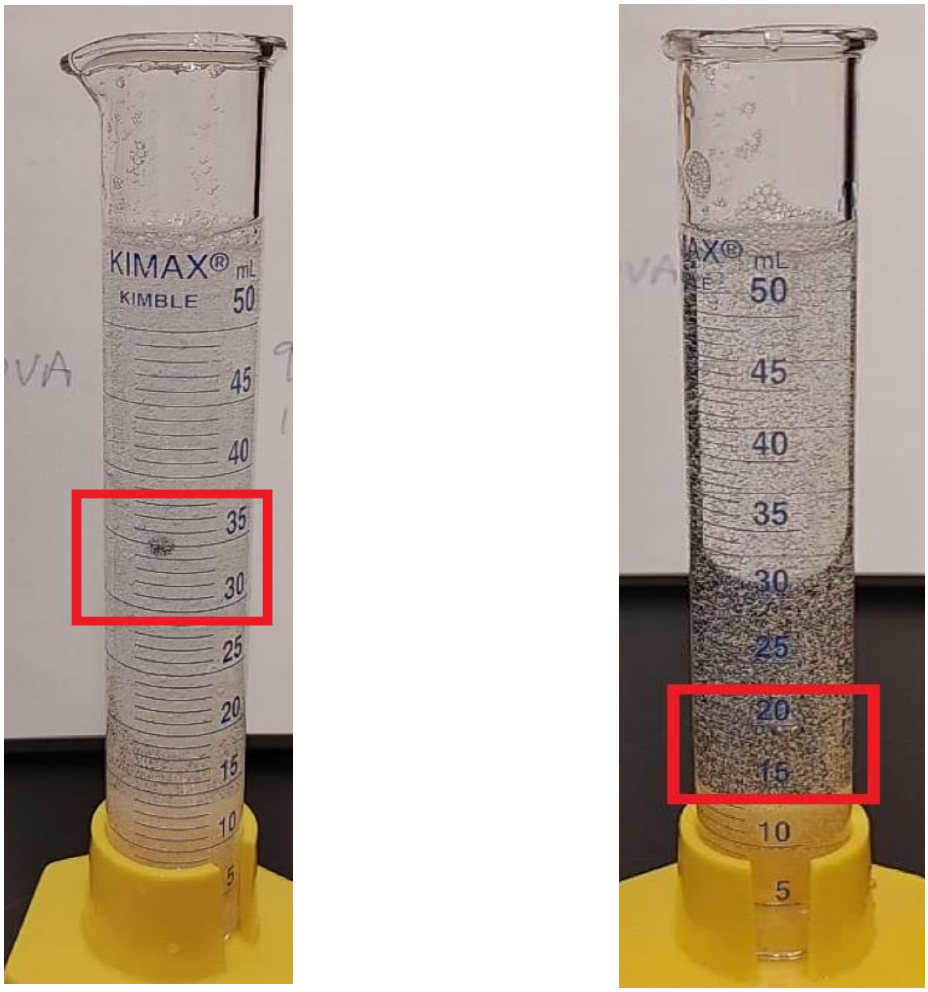

(A): 24 w/w% PVA Type I Gel

(B): 24 w/w% PVA Type II Gel

Figure 69: Preliminary Analysis of Stokes Law Experiment: 24 w/w% Type I vs Type II comparison

8 Concluding Remarks

A characterization of PVA-borax-fructose gels was completed in this work. This included the characterization of gels as well as individual constituents using various methods, including rheological techniques, with the purpose of applications to nuclear decommissioning. The following concluding remarks have been made based on this work:

- The individual constituents of borax, fructose and PVA were characterized in terms of observing density and rheology across a range of concentrations.
- Viscosity relationships of the constituents are now understood.
- PVA solutions and gels were characterized across a range of temperatures of possible exposure, from ambient room temperatures of 22.5 °C to a maximum temperature of 75 °C.
- The theory of borax interacting with fructose via boric acid, and the resulting acidification of the environment was measured experimentally.
- A summary of the various theories that describe crosslinking between PVA and borax was detailed and the theory most representative was ascribed.
- Gels of varied concentrations were successfully and repeatedly manufactured.

In summary, sufficient knowledge regarding the density and viscosity properties of the gels has been obtained such that gels can be prepared at different viscosity states. The homogeneity (demixing) issues have been solved and the gels are now understood well enough to apply to decommissioning related activities.

9 Future Work

This work concentrated on PVA type gels and specifically concentrated on the fluid properties of density and viscosity as those parameters are important for gel manufacturing and use. With respect to next steps, there is work required to relate and characterize different types of gels to specific applications with respect to decommissioning.

For improved understanding of the usability of gels, the following future work is suggested:

- exploration of methods for bulk production of the gel
- study of manipulation of the gel after manufacturing including changing the gel viscosity to transition the gel towards a solid formation
- study of reversing the gel into a liquid state for recovery of components within the gel
- the effects of increasing or decreasing the pH of the gel environment, including whether the gel can be recovered to its original state prior to pH variation

While the PVA gels used here show strong potential for easy manipulation and low cost, it is prudent to explore other types of gels. Guar gum and other protein-based gels are rather easy to make and could be used but may have some limitations due to the potential for bacterial growth. Other gels have been developed but appear to be costly to manufacture. A good evaluation of the different types of gels will be useful to determine the optimal applications for each.

With respect to decommissioning, the next steps for the PVA gel is to study a collection of contaminants of different types and forms and determine the effectiveness of the gel for capturing of materials.

10 References

[1] OECD, *Decommissioning Nuclear Power Plants: Policies, Strategies and Costs*: OECD Publishing, 2003.

[2] A. Khan, and P. Hilton, "Fibre Delivered Laser Beams - An Alternative Cost Effective Decommissioning Technology," in NOLAMP14, Gothenburg, 2013, pp. 247-258.

[3] H.-M. Yang, I.-H. Yoon, and Y. Lee, "Poly(vinyl alcohol)-borax complex-based spray coating for the decontamination of radioactive Cs from wide-area surfaces," *Chemical Engineering Journal,* vol. 402, pp. 126299, 2020/12/15/, 2020.

[4] I.-H. Yoon, C.-H. Jung, S. B. Yoon, C. Kim, S. Kim, H. B. Yang, J.-K. Moon, and W.-K. Choi, "Structure and stability of decontamination foam in concentrated nitric acid and silica nanoparticles by image analysis," *Annals of Nuclear Energy,* vol. 95, pp. 102-108, 2016/09/01/, 2016.

[5] R. Deleurence, T. Saison, F. Lequeux, and C. Monteux, "Time scales for drainage and imbibition in gellified foams: application to decontamination processes," *Soft matter,* vol. 11, no. 35, pp. 7032-7037, 2015.

[6] W. Zhang, L. Yang, S. Fang, and J. Chen, "HEA-PVA gel system for UVA radiation dose measurement," *Journal of Photochemistry and Photobiology B: Biology,* vol. 163, pp. 100-104, 2016/10/01/, 2016.

[7] S. M. M. Abtahi, and H. Sadeghi Abandansari, "Polymer gel dosimeters with PVA–GA matrix," *Australasian Physical & Engineering Sciences in Medicine,* vol. 40, no. 3, pp. 651-658, 2017/09/01, 2017.

[8] J. Liu, S. Qu, Z. Suo, and W. Yang, "Functional hydrogel coatings," *National Science Review,* vol. 8, no. 2, 2020.

[9] L. E. Millon, H. Mohammadi, and W. K. Wan, "Anisotropic polyvinyl alcohol hydrogel for cardiovascular applications," *Journal of Biomedical Materials Research Part B: Applied Biomaterials,* vol. 79B, no. 2, pp. 305-311, 2006/11/01, 2006.

[10] S. Demirel, "Temperature Dependent Polarization Effect and Capacitive Performance Enhancement of PVA-Borax Gel Electrolyte," *International Journal of Electrochemical Science*, pp. 2439-2448, 03/01, 2020.

[11] E. Al-Emam, H. Soenen, J. Caen, and K. Janssens, "Characterization of polyvinyl alcohol-borax/agarose (PVA-B/AG) double network hydrogel utilized for the cleaning of works of art," *Heritage Science,* vol. 8, no. 1, pp. 106, 2020/10/21, 2020.

[12] C. Riedo, F. Caldera, T. Poli, and O. Chiantore, "Poly(vinylalcohol)-borate hydrogels with improved features for the cleaning of cultural heritage surfaces," *Heritage Science,* vol. 3, no. 1, pp. 23, 2015/08/03, 2015.

[13] T. Sakai, "Experimental verification of homogeneity in polymer gels," *Polymer Journal,* vol. 46, no. 9, pp. 517-523, 2014/09/01, 2014.

[14] E. Casassa, A. Sarquis, and C. Van Dyke, "The gelation of polyvinyl alcohol with borax: A novel class participation experiment involving the preparation and properties of a" slime"," *Journal of Chemical Education,* vol. 63, no. 1, pp. 57, 1986.

[15] Z. Amir, I. M. Said, and B. M. Jan, "In situ organically cross-linked polymer gel for high-temperature reservoir conformance control: A review," *Polymers for Advanced Technologies,* vol. 30, no. 1, pp. 13-39, 2019.

[16] M. Wiśniewska, "Temperature effects on the adsorption of polyvinyl alcohol on silica," *Central European journal of chemistry,* vol. 10, no. 4, pp. 1236-1244, 2012.

[17] M. Bishop, N. Shahid, J. Yang, and A. R. Barron, “Determination of the mode and efficacy of the cross-linking of guar by borate using MAS 11B NMR of borate cross-linked guar in combination with solution 11B NMR of model systems,” *Dalton Transactions*, no. 17, pp. 2621-2634, 2004.

[18] A. E. Ivanov, H. Larsson, I. Y. Galaev, and B. Mattiasson, “Synthesis of boronate-containing copolymers of N, N-dimethylacrylamide, their interaction with poly(vinyl alcohol) and rheological behaviour of the gels,” *Polymer (Guilford),* vol. 45, no. 8, pp. 2495-2505, 2004.

[19] IAEA, *Methods for the Minimization of Radioactive Waste from Decontamination and Decommissioning of Nuclear Facilities*, Vienna: INTERNATIONAL ATOMIC ENERGY AGENCY, 2001.

[20] IAEA, *Decommissioning techniques for research reactors: final report of a co-ordinated research project 1997-2001*, IAEA, Vienna, 2002.

[21] NEA, *Recycling and Reuse of Materials Arising from the Decommissioning of Nuclear Facilities: A Report by the NEA Co-operative Program on Decommissioning,* NEA No. 7310, Organisation for Economic Co-Operation and Development, Paris, 2017.

[22] M. Schmittem, *Nuclear decommissioning in Japan: Opportunities for European companies*, Tokyo, 2016.

[23] CSA, *N292.6-18 Long-Term management of radioactive waste and irradiated fuel*, Canadian Standards Association Group, Toronto, Canada 2018.

[24] NRC, *The Impact of Low-Level Radioactive Waste Management Policy on Biomedical Research in the United States*, Washington, DC: The National Academies Press, 2001.

[25] A. Slimák, and V. Nečas, “Melting of contaminated metallic materials in the process of the decommissioning of nuclear power plants,” *Progress in Nuclear Energy,* vol. 92, pp. 29-39, 2016.

[26] G. Pilot, “Synthesis of results obtained with laser cutting, a promising dismantling tool,” in ICONE 18, 2010, pp. 469-475.

[27] L. Yang, Z. Tao, W. Zelei, and Z. Jigang, “The Research on Deposition of Iodine Aerosol in the Severe Nuclear Power Plant,” in 2011 Asia-Pacific Power and Energy Engineering Conference, Wuhan, China, 2011, pp. 1-4.

[28] M. I. Ojovan, *Handbook of advanced radioactive waste conditioning technologies*, Cambridge, UK: Woodhead Publishing, 2011.

[29] F. G. D. Lemma, “Characterisation of aerosols from simulated Radiological Dispersion Events,” Thesis Department of Radiation Science and Technology, Delft University of Technology, European Commission Joint Research CentreL Institute for Transuranium Elements, Delft, Holland, 2015.

[30] N. Chae, M.-H. Lee, S. Choi, B. G. Park, and J.-S. Song, “Aerodynamic diameter and radioactivity distributions of radioactive aerosols from activated metals cutting for nuclear power plant decommissioning,” *Journal of Hazardous Materials,* vol. 369, pp. 727-745, 2019/05/05/, 2019.

[31] C. Kim, S. Choi, and M. Shin, “Review—Electro-Kinetic Decontamination of Radioactive Concrete Waste from Nuclear Power Plants,” *Journal of The Electrochemical Society,* vol. 165, no. 9, pp. E330-E344, 2018.

[32] IAEA, *Radiological Characterization of Shut Down Nuclear Reactors for Decommissioning Purposes*, Vienna, 1998.

[33] M.-H. Lee, W. Yang, N. Chae, and S. Choi, “Performance assessment of HEPA filter against radioactive aerosols from metal cutting during nuclear decommissioning,” *Nuclear Engineering and Technology,* vol. 52, no. 5, pp. 1043-1050, 2019.

[34] M. T. Laraia, *Nuclear Decommissioning : Planning, Execution and International Experience*, Cambridge, UK: Woodheaed Publishing, 2012.

[35] CSA, *N292.0:19 General principles for the management of radioactive waste and irradiated fuel*, Canadian Standards Association Group Toronto, Ontario, Canada 2019.

[36] CNSC, "Nuclear Substances and Radiation Devices Regulations (SOR 2000-207)," *Nuclear Safety and Control Act*, C. N. S. Commission, ed., Gov. of Canada SOR, 2000, p. 61.

[37] T. Hirabayashi, Y. Kameo, and M. Myodo, “Application of a laser to decontamination and decommissioning of nuclear facilities at JAERI,” in Advanced High-Power Lasers and Applications, Osaka, Japan, 2000, pp. 94-103.

[38] R. Keith, “An integrated volume reduction system for radioactive waste,” *Nuclear and Chemical Waste Management,* vol. 1, no. 1, pp. 89-95, 1980.

[39] CSA, *N288.1:14 Guidelines for calculating derived release limits for radioactive material in airborne and liquid effluents for normal operation of nuclear facilities* Canadian Standards Association Group Toronto, Canada 2018.

[40] IAEA, *Treatment of Radioactive Gaseous Waste, IAEA-TECDOC-1744*, p.^pp. 53, Vienna, Austria: International Atomic Energy Agency, 2014.

[41] M. Okubo, and T. Kuwahara, "Chapter 2 - Emission regulations," *New Technologies for Emission Control in Marine Diesel Engines*, M. Okubo and T. Kuwahara, eds., pp. 25-51: Butterworth-Heinemann, 2020.

[42] CNSC, *Environmental Protection: Environmental Principles, Assessments and Protection Measures,* REGDOC-2.9.1 Canadian Nuclear Safety Commission Ottawa, Canada, 2017.

[43] OPG, *Environmental Emissions Data for Pickering Nuclear,* Environmental Emissions Data, Toronto, 2019.

[44] OPG, *Environmental Emissions Data for Nuclear Waste Management - Bruce Site,* Environmental Emissions Data, Toronto, Canada, 2019.

[45] CSA, "N288.5-11 Effluent monitoring programs at Class I nuclear facilities and uranium mines and mills" 15, CSA Group 2018, p. 128.

[46] CSA, *N288.4:19 Environmental monitoring programs at nuclear facilities and uranium mines and mills* Canadian Standards Association Group Toronto, Canada 2018.

[47] M. Laraia, "7 - Decommissioning of nuclear facilities and environmental remediation: generation and management of radioactive and other wastes," *Handbook of Advanced Radioactive Waste Conditioning Technologies*, M. I. Ojovan, ed., pp. 173-204: Woodhead Publishing, 2011.

[48] M. I. Ojovan, *An Introduction to Nuclear Waste Immobilisation*, 2nd ed. ed., Burlington: Elsevier Science, 2013.

[49] J. V. Alemán, A. V. Chadwick, J. He, M. Hess, K. Horie, R. G. Jones, P. Kratochvíl, I. Meisel, I. Mita, G. Moad, S. Penczek, and R. F. T. Stepto, “Definitions of terms relating to the structure and processing of sols, gels, networks, and inorganic-organic hybrid materials (IUPAC Recommendations 2007),” *Pure and Applied Chemistry,* vol. 79, no. 10, pp. 1801-1829, 01 Jan. 2007, 2007.

[50] P. Baglioni, M. Baglioni, N. Bonelli, D. Chelazzi, and R. Giorgi, "Chapter 9 - Smart Soft Nanomaterials for Cleaning," *Nanotechnologies and Nanomaterials for Diagnostic, Conservation and Restoration of Cultural Heritage*, G. Lazzara and R. Fakhrullin, eds., pp. 171-204: Elsevier, 2019.

[51] C. J. Brinker, and G. W. Scherer, *Sol-gel science : the physics and chemistry of sol-gel processing*, Boston: Academic Press, 1990.

[52] P. Innocenzi, "A Sol and a Gel, What Are They?," *The Sol-to-Gel Transition*, Cham, Switzerland: Springer International Publishing, 2019.

[53] P. Innocenzi, "Measuring the Sol to Gel Transition," *The Sol-to-Gel Transition*, Cham: Springer International Publishing, 2019.

[54] M. Shibayama, Y. Hiroyuki, K. Hidenobu, F. Hiroshi, and N. Shunji, “Sol-gel transition of poly(vinyl alcohol)-borate complex,” *Polymer,* vol. 29, no. 11, pp. 2066-2071, 1988.

[55] T. Fujii, T. Yano, H. Kumagai, and O. Miyawaki, “Dynamic light scattering analysis on critical behavior of cluster size distribution of polyacrylamide and agarose solutions near the sol-gel transition point,” *Food science and technology research,* vol. 6, no. 2, pp. 94-98, 2000.

[56] N. Ichinose, and H. Ura, “Concentration dependence of the sol-gel phase behavior of agarose-water system observed by the optical bubble pressure tensiometry,” *Scientific Reports,* vol. 10, no. 1, pp. 2620, 2020.

[57] X. Liu, G. Zhan, Y. Yu, and S. Li, “Rheological study on structural transition in polyethersulfone-modified bismaleimide resin during isothermal curing,” *Journal of Polymer Science Part B: Polymer Physics,* vol. 44, no. 21, pp. 3102-3108, 2006.

[58] T. Inoue, and K. Osaki, “Rheological properties of poly(vinyl alcohol)/sodium borate aqueous solutions,” *Rheologica Acta,* vol. 32, no. 6, pp. 550-555, 1993.

[59] A.-L. Kjøniksen, and B. Nyström, “Effects of Polymer Concentration and Cross-Linking Density on Rheology of Chemically Cross-Linked Poly(vinyl alcohol) near the Gelation Threshold,” *Macromolecules,* vol. 29, no. 15, pp. 5215-5222, 1996.

[60] A. Ponton, S. Barboux-Doeuff, and C. Sanchez, “Physico-chemical control of sol–gel transition of titanium alkoxide-based materials studied by rheology,” *Journal of Non-Crystalline Solids,* vol. 351, no. 1, pp. 45-53, 2005.

[61] A. Kumar, K. M. Rao, and S. S. Han, “Application of xanthan gum as polysaccharide in tissue engineering: A review,” *Carbohydrate Polymers,* vol. 180, pp. 128-144, 2018/01/15/, 2018.

[62] A. Kawano, K. Sato, K. Yamamoto, and J.-i. Kadokawa, “Preparation of Chitin Nanofiber-Reinforced Xanthan Gum Hydrogels,” *Journal of Polymers and the Environment,* vol. 27, no. 4, pp. 671-677, 2019.

[63] E. Ponzini, A. Natalello, F. Usai, M. Bechmann, F. Peri, N. Müller, and R. Grandori, “Structural characterization of aerogels derived from enzymatically oxidized galactomannans of fenugreek, sesbania and guar gums,” *Carbohydrate polymers,* vol. 207, pp. 510-520, 2019.

[64] J. A. Casas, A. F. Mohedano, and F. García-Ochoa, “Viscosity of guar gum and xanthan/guar gum mixture solutions,” *Journal of the science of food and agriculture,* vol. 80, no. 12, pp. 1722-1727, 2000.

[65] H. Huang, H. Xu, and J. Zhang, "Current Tissue Engineering Approaches for Cartilage Regeneration," *Cartilage Tissue Engineering and Regeneration Techniques*, D. D. Nikolopoulos, ed.: IntechOpen, 2019.

[66] A. Tiwari, J. J. Grailer, S. Pilla, D. A. Steeber, and S. Gong, “Biodegradable hydrogels based on novel photopolymerizable guar gum–methacrylate macromonomers for in situ fabrication of tissue engineering scaffolds,” *Acta biomaterialia,* vol. 5, no. 9, pp. 3441-3452, 2009.

[67] C. Wang, T. Yang, T. Wang, and L. Qiu, “Thermosensitive behavior of hydrophobically associating anionic guar gum solutions and gels,” *International journal of biological macromolecules,* vol. 111, pp. 169-177, 2018.

[68] A. T. Martínez, J. Rencoret, L. Nieto, J. Jiménez-Barbero, A. Gutiérrez, and J. C. Del Río, “Selective lignin and polysaccharide removal in natural fungal decay of wood as evidenced by in situ structural analyses,” *Environ Microbiol,* vol. 13, no. 1, pp. 96-107, Jan, 2011.

[69] M. Zhang, R. Helleur, and Y. Zhang, “Ion-imprinted chitosan gel beads for selective adsorption of Ag+ from aqueous solutions,” *Carbohydrate polymers,* vol. 130, pp. 206-212, 2015.

[70] Rajinder Khurmi, Evan Cross-Cooney, Nikhil Ghorpade, Joseph Shin, “OPG Pickering Nuclear Generating Station Heavy Water Storage Solution,” Faculty Of Energy Systems and Nuclear Sciences University Of Ontario Institute of Technology, Oshawa, 2018.

[71] F. Hua, and M. Qian, “Synthesis of self-crosslinking sodium polyacrylate hydrogel and water-absorbing mechanism,” *Journal of materials science,* vol. 36, no. 3, pp. 731-738, 2001.
[72] M. Liu, and T. Guo, “Preparation and swelling properties of crosslinked sodium polyacrylate,” *Journal of applied polymer science,* vol. 82, no. 6, pp. 1515-1520, 2001.
[73] V. Wong, “Hydrogels: Water abosrbing polymers,” *Catalyst,* vol. 18, no. 1, pp. 4, 2007.
[74] Y. Guan, and Y. Zhang, “Boronic acid-containing hydrogels: synthesis and their applications,” *Chemical Society reviews,* vol. 42, no. 2, pp. 816-8121, 2013.
[75] H. C. Hassan, Z. H. Z. Abidin, F. I. Chowdhury, and A. K. Arof, “A High Efficiency Chlorophyll Sensitized Solar Cell with Quasi Solid PVA Based Electrolyte,” *International journal of photoenergy,* vol. 2016, pp. 1-9, 2016.
[76] H.-M. Yang, C. W. Park, and K.-W. Lee, “Polymeric coatings for surface decontamination and ecofriendly volume reduction of radioactive waste after use,” *Progress in nuclear energy (New series),* vol. 104, pp. 67-74, 2018.
[77] H.-M. Yang, S.-C. Jang, S. B. Hong, K.-W. Lee, C. Roh, Y. S. Huh, and B.-K. Seo, “Prussian blue-functionalized magnetic nanoclusters for the removal of radioactive cesium from water,” *Journal of Alloys and Compounds,* vol. 657, pp. 387-393, 2016.
[78] R. Castellani, A. Poulesquen, F. Goettmann, P. Marchal, and L. Choplin, “A topping gel for the treatment of nuclear contaminated small items,” *Nuclear engineering and design,* vol. 278, pp. 481-490, 2014.
[79] J. Kim, C. W. Park, K.-W. Lee, and T. S. Lee, “Adsorption of Ethylenediaminetetraacetic Acid on a Gel-Type Ion-Exchange Resin for Purification of Liquid Waste Containing Cs Ions,” *Polymers,* vol. 11, no. 2, pp. 297, 2019.
[80] J. Taño, S. Hayashi, S. Hirota, C. A. Gonzales, and H. Yasuda, “Development of a reusable PVA-GTA-I gel dosimeter for 3D radiation dose assessments,” *Journal of physics. Conference series,* vol. 1305, pp. 12034, 2019.
[81] F. L. Buchholz, S. R. Pesce, and C. L. Powell, “Deswelling stresses and reduced swelling of superabsorbent polymer in composites of fiber and superabsorbent polymers,” *Journal of applied polymer science,* vol. 98, no. 6, pp. 2493-2507, 2005.
[82] M. Huang, Y. Hou, Y. Li, D. Wang, and L. Zhang, “High performances of dual network PVA hydrogel modified by PVP using borax as the structure-forming accelerator,” *Designed monomers and polymers,* vol. 20, no. 1, pp. 505-513, 2017.
[83] S. Naorem, “Effect of surfactants on polyvinyl alcoholborax hydrogel: Rheology and thermal aspects,” *Indian Journal of Chemistry - Section A Inorganic, Physical, Theoretical and Analytical Chemistry,* vol. 52, pp. 879-883, 2013.
[84] M. B. Lawrence, J. A. E. Desa, V. K. Aswal, and R. Rai, “Properties of poly(vinyl alcohol)–borax gel doped with neodymium and praseodymium,” *Bulletin of materials science,* vol. 37, no. 2, pp. 301-307, 2014.
[85] K. Dyamenahalli, A. Famili, and R. Shandas, "3 - Characterization of shape-memory polymers for biomedical applications," *Shape Memory Polymers for Biomedical Applications*, L. H. Yahia, ed., pp. 35-63, Bristol, U.K: Woodhead Publishing, 2015.
[86] C. W. Macosko, *Rheology : principles, measurements, and applications*, New York; Weinheim; Cambridge (UK): VCH Publishers : VCH Verlagsgesellschaft, 1994.
[87] A. Shrivastava, "3 - Plastic Properties and Testing," *Introduction to Plastics Engineering*, A. Shrivastava, ed., pp. 49-110, Norwich, New York, U.S.A: William Andrew Publishing, 2018.
[88] T. Eliades, S. Zinelis, D. G. Kim, and W. Brantley, "2 - Structure/property relationships in orthodontic polymers," *Orthodontic Applications of Biomaterials*, T. Eliades and W. A. Brantley, eds., pp. 39-59, Bristol, U.K: Woodhead Publishing, 2017.

[89] A. B. Kousaalya, B. I. Biddappa, S. Rai, and S. Pilla, "7 - Mechanical performance of poly(propylene carbonate)-based blends and composites," *Biocomposites*, M. Misra, J. K. Pandey and A. K. Mohanty, eds., pp. 161-200, Bristol, U.K: Woodhead Publishing, 2015.

[90] K. Deshmukh, M. Basheer Ahamed, R. R. Deshmukh, S. K. Khadheer Pasha, P. R. Bhagat, and K. Chidambaram, "3 - Biopolymer Composites With High Dielectric Performance: Interface Engineering," *Biopolymer Composites in Electronics*, K. K. Sadasivuni, D. Ponnamma, J. Kim, J. J. Cabibihan and M. A. AlMaadeed, eds., pp. 27-128, Amsterdam, Netherlands: Elsevier, 2017.

[91] S. Aruldass, V. Mathivanan, A. R. Mohamed, and C. T. Tye, "Factors affecting hydrolysis of polyvinyl acetate to polyvinyl alcohol," *Journal of Environmental Chemical Engineering,* vol. 7, no. 5, pp. 103238, 2019.

[92] A. Shrivastava, "2 - Polymerization," *Introduction to Plastics Engineering*, A. Shrivastava, ed., pp. 17-48, Bristol, U.K: William Andrew Publishing, 2018.

[93] K. Mamada, V. Fridrici, H. Kosukegawa, P. Kapsa, and M. Ohta, "Friction Properties of Poly(vinyl alcohol) Hydrogel: Effects of Degree of Polymerization and Saponification Value," *Tribology Letters,* vol. 42, no. 2, pp. 241-251, 2011.

[94] R. A. Croot, A. R. Goodall, and S. D. Lubetkin, "Adsorption properties of vinyl alcohol/vinyl acetate copolymers," *Colloids and Surfaces,* vol. 49, pp. 351-362, 1990.

[95] J. Huang, "Chapter 4 - Lignin Chemicals and Their Applications," *Lignin Chemistry and Applications*, S. Fu and L. Gan, eds., pp. 79-134, Amsterdam, Netherlands: Elsevier, 2019.

[96] Q. Fan, "5 - Fabric chemical testing," *Fabric Testing*, J. Hu, ed., pp. 125-147, Bristol, U.K: Woodhead Publishing, 2008.

[97] X. Li, M. Shu, H. Li, X. Gao, S. Long, T. Hu, and C. Wu, "Strong, tough and mechanically self-recoverable poly(vinyl alcohol)/alginate dual-physical double-network hydrogels with large cross-link density contrast," *RSC Advances,* vol. 8, no. 30, pp. 16674-16689, 2018.

[98] 20MuleTeamBorax, *Borax Material Safety Data Sheet*, Boron, California, U.S.A, May 2000.

[99] R. Cope, "Metalliods - Chapter 15," *Veterinary Toxicology for Australia and New Zealand*, R. Dalefield, ed., pp. 255 - 277, Amsterdam, Netherlands: Elsevier, 2015.

[100] O. Sahin, and A. N. Bulutcu, "Dehydration behaviour of borax pentahydrate to anhydrous borax by multi-stage heating in a fluidized," *Turkish Journal of Chemistry,* vol. 26, no. 1, pp. 89-96, 2002.

[101] S. Kocakuşak, "Production of anhydrous, crystalline borax in a fluidized bed," *Industrial & engineering chemistry research,* vol. 35, no. 4, pp. 1424-1428, 1996.

[102] L. S. Ruhl, "Thermodynamics of 1: 2 Sodium Borate Minerals," University of Florida, 2008.

[103] A. W. Coats, and J. Redfern, "Kinetic parameters from thermogravimetric data," *Nature,* vol. 201, no. 4914, pp. 68, 1964.

[104] J. A. Beran, *Laboratory manual for principles of general chemistry*, Hoboken, New Jersey, U.S.A: John Wiley & Sons, 2010.

[105] N. J. Tro, T. Fridgen, and L. Shaw, *Chemistry: A Molecular Approach*, 2nd ed ed., Upper Saddle River, New Jersey, U.S.A: Pearson Prentice Hall, 2011.

[106] K. McLaughlin, N. Wyffels, A. Jentz, and M. Keenan, "The gelation of poly (vinyl alcohol) with Na2B4O7 10H2O: killing slime," *Journal of chemical education,* vol. 74, no. 1, pp. 97, 1997.

[107] T. S. Hansen, J. Mielby, and A. Riisager, "Synergy of boric acid and added salts in the catalytic dehydration of hexoses to 5-hydroxymethylfurfural in water," *Green chemistry,* vol. 13, no. 1, pp. 109-114, 2011.

[108] Y. Xiong, L. Kirkes, and T. Westfall, "Experimental determination of solubilities of sodium tetraborate (borax) in NaCl solutions, and a thermodynamic model for the Na-B(OH)3-Cl-SO4 system to high-ionic strengths at 25 °C," *American Mineralogist,* vol. 98, no. 11-12, pp. 2030, 2013.

[109] S. S. Gujral, "UV-Visible Spectral Analysis of Boric Acid in Different Solvents: A Case Study," *International Journal of Pharmaceutical Sciences and Drug Research,* vol. 6, no. 2, pp. 830-834, 2015.

[110] H. Ge, Y. Zhou, H. Liu, Y. Fang, and C. Fang, "Molecular interactions in aqueous solutions of polyborates at different acidity based on the Raman spectroscopy data at 25°C," *Russian Journal of Physical Chemistry A,* vol. 91, no. 10, pp. 1925-1931, 2017.

[111] C. E. Crestani, A. Bernardo, C. B. Costa, and M. Giulietti, "Fructose solubility in mixed (ethanol+ water) solvent: experimental data and comparison among different thermodynamic models," *Journal of Chemical & Engineering Data,* vol. 58, no. 11, pp. 3039-3045, 2013.

[112] T. Barclay, M. Ginic-Markovic, P. Cooper, and N. Petrovsky, "The chemistry and sources of fructose and their effect on its utility and health implications," *Journal of Excipients and Food Chemicals,* vol. 3, no. 2, pp. 67-82, 2012.

[113] T. Barclay, M. Ginic-Markovic, M. R. Johnston, P. Cooper, and N. Petrovsky, "Observation of the keto tautomer of D-fructose in D(2)O using (1)H NMR spectroscopy," *Carbohydrate research,* vol. 347, no. 1, pp. 136-141, 2012.

[114] X. Xia, J. Chang, J. Hunter, and B. Nemzer, "Identification and quantification of fructoborate ester complex using liquid chromatography coupled with Q Exactive Orbitrap mass spectrometry," *Journal of Food Research,* vol. 6, no. 3, pp. 85-92, 2017.

[115] V. Telis, J. Telis-Romero, H. Mazzotti, and A. Gabas, "Viscosity of aqueous carbohydrate solutions at different temperatures and concentrations," *International Journal of food properties,* vol. 10, no. 1, pp. 185-195, 2007.

[116] ThermoFisherScientific, *Safety Data Sheet: D-Fructose, Cat No. A17718, CAS-No. 57-48-7*, Alfa Aesar, Ward Hill, Massachusetts, U.S.A, 2009.

[117] G. A. Hurst, M. Bella, and C. G. Salzmann, "The rheological properties of poly (vinyl alcohol) gels from rotational viscometry," *Journal of Chemical Education,* vol. 92, no. 5, pp. 940-945, 2014.

[118] L. V. Angelova, "Gels from Borate-Crosslinked Partially Hydrolyzed Poly (vinyl acetate)s: Characterization of Physical and Chemical Properties and Applications in Art Conservation," Georgetown University, 2013.

[119] Y. Kazuhiko, "A Solid-State NMR Study of Boric Acid Doped in Poly (vinyl alcohol)," *The Chemical Society of Japan: Chemistry Letters,* vol. 42, no. 10, pp. 1223-1224, 2013.

[120] M. Rietjens, and P. A. Steenbergen, "Crosslinking mechanism of boric acid with diols revisited," *European journal of inorganic chemistry,* vol. 2005, no. 6, pp. 1162-1174, 2005.

[121] M. Karakaplan, S. Tural, M. Sunkür, and H. Hoşgören, "Effect of 1, 3-diol structure on the distribution of boron between CHCl3 and aqueous phase," *Separation science and technology,* vol. 38, no. 8, pp. 1721-1732, 2003.

[122] H. S. Isbell, J. F. Brewster, N. B. Holt, and H. L. Frush, "Behavior of certain sugars and sugar alcohols in the présence of tetraborates-Correlation of optical rotation and compound formation," *J. Res. natn. Bur. Stand,* vol. 40, no. 129, pp. 1, 1948.

[123] N. Vermaas, "Investigations on the equilibria of the boric acid-diol-water-system. I," *Recueil des Travaux Chimiques des Pays-Bas,* vol. 51, no. 1, pp. 67-92, 1932.

[124] J. Böeseken, "La Méthode à L'Acide Borique et la Configuration de Quelques Bisaccharides," *Recueil des Travaux Chimiques des Pays-Bas,* vol. 61, no. 2, pp. 82-87, 1942.

[125] M. Ishibashi, T. Fujinaga, and T. Nagai, "Studies on Boric Acid and Borates.(I): The Effect of Boric acid and of Borates on the Polarographic Wave of Fructose," *Bulletin of the Institute for Chemical Research, Kyoto University* vol. 36, no. 6, pp. 134-138, 1958.

[126] D. S. Viswanath, T. K. Ghosh, D. H. Prasad, N. V. Dutt, and K. Y. Rani, *Viscosity of liquids: theory, estimation, experiment, and data*, Dodrecht, Netherlands: Springer 2007.

[127] T. A. Davidson, S. United, and M. Bureau of, *A simple and accurate method for calculating viscosity of gaseous mixtures*, Washington, DC: U.S. Dept. of the Interior, Bureau of Mines, 1993.
[128] M. Toledo, "Operating Instructions: B-S line of balances ", 2003.
[129] A. Faghri, and Y. Zhang, "1 - Introduction to Transport Phenomena," *Transport Phenomena in Multiphase Systems*, A. Faghri and Y. Zhang, eds., pp. 1-106, Boston: Academic Press, 2006.
[130] E. S. Freeman, and B. Carroll, "The application of thermoanalytical techniques to reaction kinetics: the thermogravimetric evaluation of the kinetics of the decomposition of calcium oxalate monohydrate," *The Journal of Physical Chemistry,* vol. 62, no. 4, pp. 394-397, 1958.
[131] E. Akbay, and M. R. Altıokka, "Kinetics of borax dehydration by thermal analysis," *Anadolu Üniversitesi Bilim Ve Teknoloji Dergisi A-Uygulamalı Bilimler ve Mühendislik,* vol. 18, no. 3, pp. 713-719, 2017.
[132] R. K. Pathria, and P. D. Beale, "15 - Fluctuations and Nonequilibrium Statistical Mechanics," *Statistical Mechanics (Third Edition)*, R. K. Pathria and P. D. Beale, eds., pp. 583-635, Boston: Academic Press, 2011.
[133] V. A. Bershtein, Gun, apos, V. M. ko, L. M. Egorova, Z. Wang, M. Illsley, E. F. Voronin, Prikhod, apos, G. P. ko, P. N. Yakushev, R. Leboda, J. Skubiszewska-Zięba, and S. V. Mikhalovsky, "Dynamics, thermal behaviour and elastic properties of thin films of poly(vinyl alcohol) nanocomposites," *RSC advances,* vol. 2, no. 4, pp. 1424-1431, 2012.
[134] V. V. Kochervinskii, V. A. Glukhov, and B. V. Lokshin, "Structure and properties of commercial fluoroplast films," *Polymer Science U.S.S.R.,* vol. 29, no. 9, pp. 2001-2009, 1987.
[135] S.-P. Li, G. Zhao, and H.-Y. Chen, "The Relationship between Steady Shear Viscosity and Complex Viscosity," *Journal of Dispersion Science and Technology,* vol. 26, no. 4, pp. 415-419, 2005.
[136] Fungilab;, *Fungilab: One Series Rotational Viscometer - Software Version 1.2, Instruction Manual* Grases - Barcelona, Spain
[137] T. G. Mezger, *The Rheology Handbook : 4th Edition*, Hannover: Vincentz Network, 2014.
[138] ISO, "ISO 3219 - Plastics — Polymers/resins in the liquid state or as emulsions or dispersions — Determination of viscosity using a rotational viscometer with defined shear rate."
[139] V. A. Vanoni, "Appendix II: Density and Viscosity of Water 0°C-40°C," *Sedimentation Engineering - ASCE Manuals and Reports on Engineering Practice (MOP) No. 54*, Reston, Virginia, U.S.A: American Society of Civil Engineers (ASCE).
[140] NETZSCH, *Operating Instructions: Simultaneous TG-DTA/DSC Apparatus - STA 449 F1 Jupiter*, 2012.
[141] J. Isac-García, J. A. Dobado, F. G. Calvo-Flores, and H. Martínez-García, "Chapter 13 - Green Chemistry Experiments," *Experimental Organic Chemistry*, J. Isac-García, J. A. Dobado, F. G. Calvo-Flores and H. Martínez-García, eds., pp. 417-484, Cambridge, Massachusetts, U.S.A: Academic Press, 2016.
[142] V. R. N. Telis, J. Telis-Romero, H. B. Mazzotti, and A. L. Gabas, "Viscosity of Aqueous Carbohydrate Solutions at Different Temperatures and Concentrations," *International Journal of Food Properties,* vol. 10, no. 1, pp. 185-195, 2007.
[143] M. Mohsen-Nia, and H. Modarress, "Viscometric study of aqueous poly (vinyl alcohol)(PVA) solutions as a binder in adhesive formulations," *Journal of adhesion science and technology,* vol. 20, no. 12, pp. 1273-1280, 2006.
[144] K. Lewandowska, A. Dąbrowska, and H. Kaczmarek, "Rheological properties of pectin, poly(vinyl alcohol) and their blends in aqueous solutions," *e-Polymers,* vol. 12, no. 1, pp. 160-172, 2012.
[145] N. R. M. Kevin P. Menard, "Dynamic Mechanical Analysis in the Analysis of Polymers and Rubbers," *Encyclopedia of Polymer Science and Technology*, pp. 1-33, Somerset, New Jersey, U.S.A: John Wiley & Sons, 2015.

[146] E. A. Campo, "3 - Thermal Properties of Polymeric Materials," *Selection of Polymeric Materials*, E. A. Campo, ed., pp. 103-140, Norwich, NY: William Andrew Publishing, 2008.
[147] Y. Ōyanagi, and M. Matsumoto, “Viscosity of moderately concentrated aqueous solutions of polyvinyl alcohol,” *Journal of Colloid Science,* vol. 17, no. 5, pp. 426-438, 1962.
[148] J. F. Steffe, "Modelling Rheological Behavior of Fluids," *Rheological methods in food process engineering*, p. 428, East Lansing, MI: Freeman Press, 1996.
[149] S. Pedro Henrique, S. Luiza Helena Meller da, R. Antônio Manoel da Cruz, and S. José Antonio Ribeiro de, “Influence of temperature, concentration and shear rate on the rheological behavior of malay apple (Syzygium malaccense) juice,” *Brazilian Journal of Food Technology,* vol. 19, no. 0.
[150] H. Wang, X. Liu, P. Apostolidis, and T. Scarpas, “Non-Newtonian Behaviors of Crumb Rubber-Modified Bituminous Binders,” *Applied sciences,* vol. 8, no. 10, pp. 1760, 2018.
[151] K. Watanabe, "Chapter 2 - Conservation of Mass and Momentum," *Drag Reduction of Complex Mixtures*, K. Watanabe, ed., pp. 13-34, London, U.K: Academic Press, 2018.
[152] IAEA, "IAEA Safety Standards Series: Application of the concepts of exclusion, exemption and clearance RS-G-1.7," International Atomic Energy Agency, 2004, p. 39.
[153] CSA, "N292.5-11: Guideline for the exemption or clearance from regulatory control of materials that contain, or potentially contain, nuclear substances N292.5-11," Canadian Standards Association Group, 2011, p. 119.
[154] N. Kabay, and M. Bryjak, "Chapter 9 - Boron Removal From Seawater Using Reverse Osmosis Integrated Processes," *Boron Separation Processes*, N. Kabay, M. Bryjak and N. Hilal, eds., pp. 219-235, Amsterdam: Elsevier, 2015.
[155] B. Gu, and D. J. Burgess, "Chapter 20 - Polymeric Materials in Drug Delivery," *Natural and Synthetic Biomedical Polymers*, S. G. Kumbar, C. T. Laurencin and M. Deng, eds., pp. 333-349, Oxford, U.K: Elsevier, 2014.

11 Appendices

11.1 Appendix: Chapter 2

11.1.1 Unconditional Clearance Level

The unconditional clearance level are as follows, with respect to with respect to contamination by a single radioactive nuclear substance that is of artificial origin [36]:

- 1 Bq/g if the atomic number is ≤ 81.
- 1 Bq/g if the atomic number is > 81, and the substance or its progeny does not emit alpha type radiation.
- 0.1 Bq/g if the atomic number is > 81 and the substance or its progeny emits alpha type radiation.

Alternatively, if more than one species of artificial origin is of concern, as is the case in almost all practical cases, then the unconditional clearance level can be calculated via the following summation equation as defined in IAEA Safety Standard RS-G-1.7 as well as N292.5 [152, 153]:

$$\sum_{i=1}^{n} \frac{C_i}{C_{Li}} < 1 \qquad \text{Equation 66}$$

Wherein, c_i $(\frac{Bq}{cm^2})$ is the specific activity of the radionuclide i, within the material of concern, c_{Li} $(\frac{Bq}{cm^2})$ is the specific clearance level of radionuclide i, within the material of concern and n is the number of radionuclides within the material. Clearance levels (C_{Li}) of artificial radioactive substances, can be found in Schedule 2, section 1 of the Nuclear Substances and Radiation Devices Regulations [36].

11.1.2 Fungal Growth Observation of Polysaccharide Gels

Figure 70: 5 w/v% Xanthan, Guar Gum Gel ; Prior to Observation of 1 month [70]

Figure 71: 3 w/v% Xanthan, Guar Gum Gel ; Prior to Observation of 1 month [70]

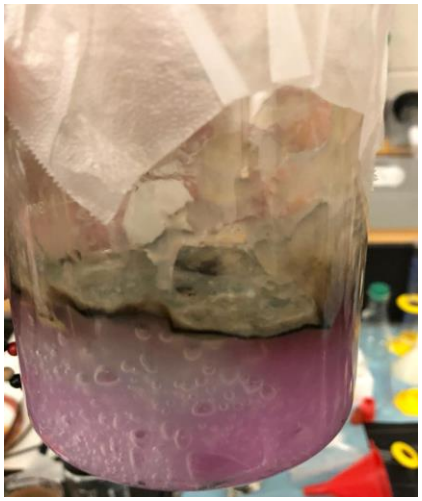

Figure 72: 5 w/v% Xanthan, Guar Gum Gel ; Post Observation of 1 Month – Fungal growth present [70]

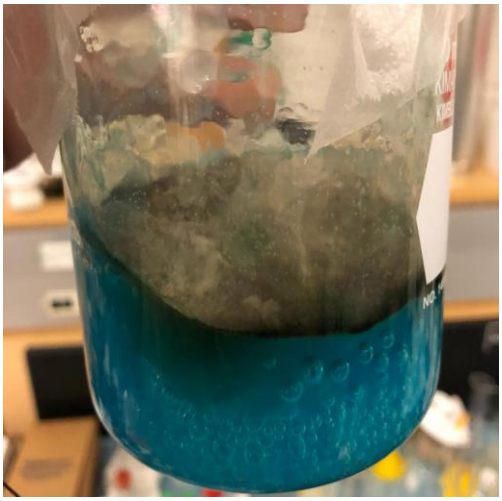

Figure 73: 3 w/v% Xanthan, Guar Gum Gel ; Post Observation of 1 month – Fungal growth present [70]

11.1.3 Sodium Polyacrylate Gel Dependence on Water

Figure 74: 0.5 g Sodium Polyacrylate Gel [70]

Figure 75: Sodium Polyacrylate Gel after 4 days of evaporation [70]

11.2 Appendix: Chapter 3

11.2.1 Multi-equilibria Expressions for the dissolution of Borax

The dissolution of Borax in water that results in the formation of sodium and borate ions is described as per the following expression [104]:

$$Na_2B_4O_5(OH)_4 * 8H_2O\ (s) \underset{\rightleftarrows}{H_2O} 2Na^+(aq) + B_4O_5(OH)_4^{2-}(aq) + 8H_2O\ (l) \qquad \text{Equation 67}$$

Equilibrium Expression for Equation 67:

$$K_{sp} = [Na^+]^2[B_4O_5(OH)_4^{2-}] \qquad \text{Equation 68}$$

Wherein two Na^+ are produced for each $[B_4O_5(OH)_4^{2-}]$, hence $[Na^+] = 2[B_4O_5(OH)_4^{2-}]$, therefore K_{sp} can be expressed as follows:

$$K_{sp} = [(2[B_4O_5(OH)_4^{2-}])]^2[B_4O_5(OH)_4^{2-}] = 4[B_4O_5(OH)_4^{2-}]^3 \qquad \text{Equation 69}$$

Wherein, the borate-1 ion (expressed $B_4O_5(OH)_4^{2-}$); the product of the dissociation of borax in water, as detailed in Equation 67), is a weak base and reacts with water to produce hydroxide ions (a strong base) and boric acid (a weak acid), as expressed in Equation 70:

$$B_4O_5(OH)_4^{2-}\ (aq) + 5H_2O\ \rightleftarrows 4H_3BO_3(aq) + 2OH^-(aq) \qquad \text{Equation 70}$$

Equilibrium Expression for Equation 70:

$$K = \frac{[H_3BO_3]^4[OH^-]^2}{[B_4O_5(OH)_4^{2-}]} \qquad \text{Equation 71}$$

Boric acid (expressed H_3BO_3); the product of the weak base borate ion reacting with water) is a weak acid (behaves like a Lewis acid [105], with a pK_a = 9.3 [106]. At a pH lower than 7, it exists as Boric acid, and at a pH greater than 10.5 it exists as the tetrahydroxyborate ion or the borate monovalent anion, $B(OH)_4^-$ [154]; Due to the weak acid behaviour of Boric acid, typically, H_3BO_3, through ionization via accepting OH- instead of giving up H+ [14], exists with $B(OH)_4^-$ in equilibrium [106]) as expressed in Equation 7 of section 4.1.1.1.

Equilibrium Expression for Equation 7:

$$K_a = \frac{[B(OH_4)]^-[H_3O^+]}{[H_3BO_3]} \qquad \text{Equation 72}$$

Under certain circumstances, particularly in the pH range of 6 – 11 and at concentrations > 0.025 mol/L, polyborate ions including, $B_3O_3(OH)_4^-$, $B_4O_5(OH)_4^-$, and $B_5O_6(OH)_4^-$ also exist in equilibrium with Boric acid and $B(OH)_4^-$ [154]. According to literature, it is either the Boric acid or the tetrahydroxyborate ion species from the equilibria reaction in Equation 7 that is responsible for crosslinking with PVA.

11.3 Appendix: Chapter 4

11.3.1 PVA-Borax-fructose Gels: Table of relative concentrations

Relative Concentration of PVA Solution: Gel Type I –

$$Concentration = \frac{50}{52} * 100 = 96.15 \frac{w}{w}\% \qquad \text{Equation 73}$$

Relative Concentration of PVA Solution: Gel Type II –

$$Concentration = \frac{46}{52} * 100 = 88.46 \frac{w}{w}\% \qquad \text{Equation 74}$$

Table 36 specifies concentration equivalents for gel manufacturing, assuming a 52 g sample size:

Table 36: Concentration Equivalents of PVA Solution and Borax-fructose Solution for Gel Manufacturing: Equivalents Assuming 52 g sample size

Concentration of PVA Solution Used: Refer to Table 5 (w/w %)	Mass Equivalent of PVA Solution: Gel Type I (g):	Relative Concentration of Borax - Fructose (10w/v%-13.6 w/v%) Solution Used: Gel Type I	Mass Equivalent of Borax-fructose Solution: Gel Type II (g)	Mass Equivalent of PVA Solution: Gel Type II (g):	Relative Concentration of Borax - Fructose (10w/v%-13.6 w/v%) Solution Used: Gel Type II	Mass Equivalent of Borax-fructose Solution: Gel Type II (g)
16	50	$= \frac{2}{52} * 100$ $= 3.85 \frac{w}{w}\%$	2	46	$= \frac{6}{52} * 100$ $= 11.54 \frac{w}{w}\%$	6
24	50	$= \frac{2}{52} * 100$ $= 3.85 \frac{w}{w}\%$	2	46	$= \frac{6}{52} * 100$ $= 11.54 \frac{w}{w}\%$	6
28	50	$= \frac{2}{52} * 100$ $= 3.85 \frac{w}{w}\%$	2	46	$= \frac{6}{52} * 100$ $= 11.54 \frac{w}{w}\%$	6
34	50	$= \frac{2}{52} * 100$ $= 3.85 \frac{w}{w}\%$	2	46	$= \frac{6}{52} * 100$ $= 11.54 \frac{w}{w}\%$	6
44	50	$= \frac{2}{52} * 100$ $= 3.85 \frac{w}{w}\%$	2	46	$= \frac{6}{52} * 100$ $= 11.54 \frac{w}{w}\%$	6

11.3.2 Rheology – Low Sample Container

Large gaps between the spindle and the sample container (spindle to container ratios greater than 1.087, according to ISO 3219 [137, 138]) could result in secondary flow effects and inhomogeneous deformations. In contrary, viscometer manual recommends a minimum container radius of 83 mm (a spindle to container radius ratio is $\frac{32.5}{14} = 2.32$). When performing baseline measurements using water as the fluid, the viscometer measures a reasonable value for the viscosity of water.

When obtaining viscosity measurements using the low sample container, according to literature, influences due to secondary flow effects and inhomogeneous deformations should be small, however, measurements were found to be higher. This is due to wall effects. It was initially expected that the viscometer would mathematically correct for any wall effects and the resulting increased shear rate; however, this was not the case. A correction factor correlation was developed such that the low sample container and the thermostatic bath (which directly connects to the low sample container thermal jacket) can be used to perform thermal rheology experiments. The correlation compared the viscosity of the same fluid measured using a beaker of diameter greater than or equal to 83 mm versus the viscosity of the same fluid measured using the low sample container.

Rheological properties of fluids of varied viscosities, including various concentrations of borax, fructose, and borax-fructose solutions, as well as concentrations of PVA solutions were obtained using both a beaker with a diameter of 83 mm and using the low sample container (the container used in conjunction with the thermal jacket). These datasets will be referred to as the correction factor dataset (CrrFctrData). Viscosities obtained using the beaker and the low sample container (LSC) were plotted against one another, and curve fitting was performed using a python code to obtain a correction factor function. The python code is attached in section 11.3.3.

As per the python code, a 3rd degree polynomial was found to best correlate the beaker and the low sample container viscosity values (within the 0 – 40 mPa·s LSC range), with a coefficient of determination (R^2) of 0.99 (Figure 76). Substituting the coefficients, the polynomial that best correlates low sample container viscosity to beaker viscosity is in Equation 75:

$$y = 0.000039x^3 - 0.004x^2 + 0.31x + 0.63$$ Equation 75

Substituting LSC viscosity values into x will provide for the beaker equivalent. Furthermore, correlations were also used to convert other LSC rheological parameters such as shear stress, shear rate, as well as RPM, as these parameters are used to calculate uncertainty of viscosity converted from LSC to beaker equivalent. It must be noted that the correction factor curve can only be used under instances where viscosity data conversion is performed through interpolation, especially since the behaviour of the curve fit function is unknown outside the range of the datapoints used to for curve fitting.

The python code plots the LSC viscosities converted into beaker equivalent using the correction factor function along with the compounded uncertainty. A plot of a sample dataset including the associated uncertainty of both, the LSC viscosity, as well as the beaker equivalent is output using the python code. This demonstrates the code can convert LSC viscosity to beaker equivalent, seen in Figure 77. The sample dataset in this case is a dataset obtained by measuring the viscosity of 2.37 g/dL concentration PVA solution. The averaged rheological properties of this dataset was used as part of the correction factor dataset, from which the correction factor correlation was developed. By comparing the LSC viscosity dataset to the converted dataset, the python code was validated. The averaged viscosity of the LSC was calculated to be 7.98 cP; the averaged viscosity of the correction factor correlation converted beaker equivalent was calculated to be 2.89 cP. As can be seen in Figure 77, the converted dataset has an approximate average of 2.89 cP. The validated python code is used to correct the viscosity measurements whenever the low sample container is used.

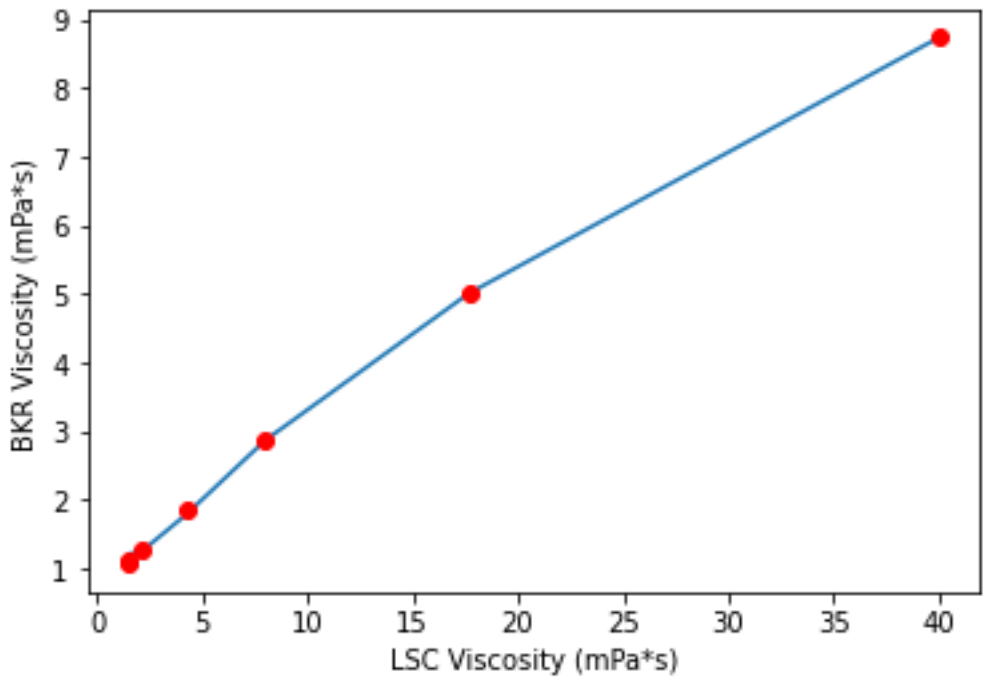

Figure 76: 3rd Degree Polynomial Curve Fit - Relates correction factor dataset low sample viscosity to beaker viscosity.

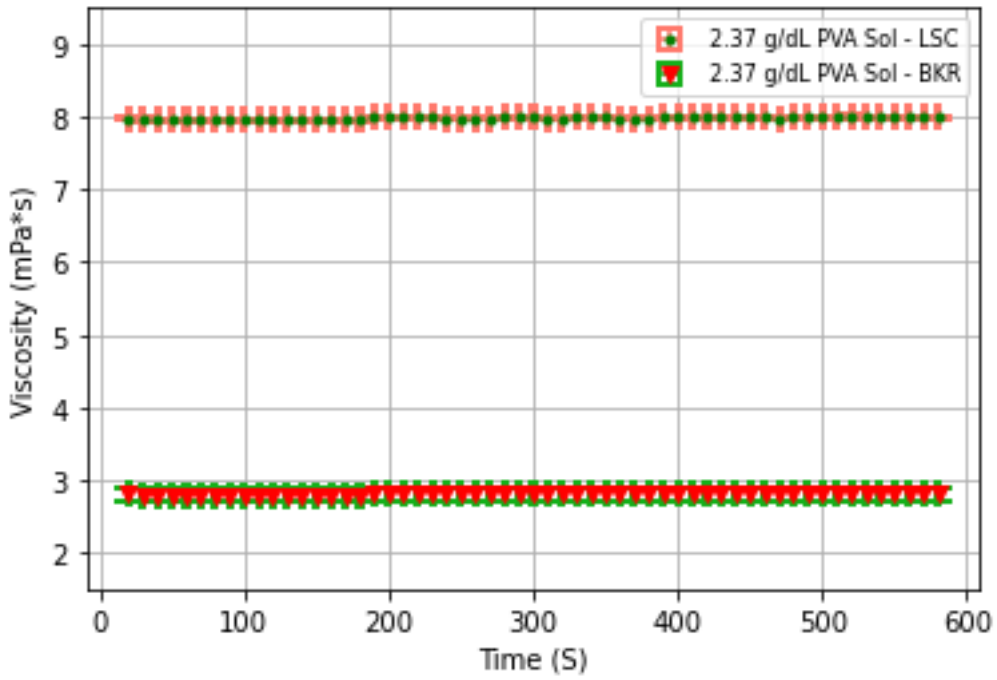

Figure 77: Plot allowing for comparison between LSC and converted beaker equivalent viscosities; Dataset of the 2.37 g/dL PVA solution with a beaker viscosity average of 2.86 cP and LSC viscosity of 7.98 cP was used.

11.3.3 Python Code – Low Sample Container

Snippets of the python code function that converts low sample container into beaker equivalent are depicted in the figures below. Wherein the function plots beaker relative to low sample container datapoints and curve fits based on various functions, including 2nd Degree polynomial, 3rd degree polynomial, exponential, and logarithmic. The function also calculates the R^2 value of the various curve fits. The function with the highest R^2 was found to be the 3rd degree polynomial, and as such is the one used for conversion of low sample container values into beaker equivalent.

```
###### Import relevant libraries #####
import pandas as pd
from matplotlib import pyplot as plt
import numpy as np
from pylab import *
from scipy import optimize
from scipy.optimize import curve_fit
from uncertainties import ufloat
from uncertainties.umath import*


#OPENPYXL#
import openpyxl
from openpyxl import Workbook
from openpyxl.styles import Font, Color, colors
from openpyxl.utils import get_column_letter


##### Define equations for non linear least squares curve fitting #####

# 2nd Degree Polynomial
def CorrFctr_1(x,c0,c1,c2):
    return c0+c1*x+c2*x**2

# 3rd Degree Polynomial
def CorrFctr_2(x,c0,c1,c2,c3):
    return c0+c1*x+c2*x**2+c3*x**3

# Exponential Function
def CorrFctr_3(x,c0,c1,c2):
    return c0*np.exp(x**c1+c2)

# Logarithmic Function
def CorrFctr_4(x,c0,c1,c2,c3):
    return c0+c1*np.log(c2*x+c3)
```

Figure 78: Python Code Snippet for the conversion of low sample container into beaker equivalent values; Part 1 of 3

```
def CFit (COL_INP_LSC,COL_INP_BKR,g1,g2,g3,g4):
    
    c1_ci,cov1_ci = curve_fit(CorrFctr_1,COL_INP_LSC,COL_INP_BKR,g1,sigma=None,absolute_sigma=False,check_finite=True, method='lm')

    #For Loop that converts LSC Shear Stress values into BKR values using the 2nd Degree Polynomial
    n_ci = len(COL_INP_LSC)
    y1_ci= np.empty(n_ci)
    for i in range(len(COL_INP_LSC)):
        y1_ci[i]=CorrFctr_1(COL_INP_LSC[i],c1_ci[0],c1_ci[1],c1_ci[2])

    
    figci_1, ax1 = plt.subplots()
    ax1.plot(COL_INP_LSC, COL_INP_BKR, color='green', marker='o', linestyle='dashed')
    ax1.plot(COL_INP_LSC,y1_ci,'ro')
    plt.title("CorrFctr_1 Polynomial 2nd")

    #r2_score function is used to calculate the R^2 value of the 2nd Degree Polynomial Curve Fit
    from sklearn.metrics import r2_score
    print('R^2_1: ', r2_score(COL_INP_BKR,y1_ci))


    c2_ci,cov2_ci = curve_fit(CorrFctr_2,COL_INP_LSC,COL_INP_BKR,g2,sigma=None,absolute_sigma=False,check_finite=True, method='lm')
    
    #For Loop that converts LSC Shear Stress values into BKR values using the 3rd Degree Polynomial
    y2_ci= np.empty(n_ci)
    for i in range(len(COL_INP_LSC)):
        y2_ci[i]=CorrFctr_2(COL_INP_LSC[i],c2_ci[0],c2_ci[1],c2_ci[2],c2_ci[3])
    
    figci_2, ax1 = plt.subplots()
    ax1.plot(COL_INP_LSC, COL_INP_BKR, color='green', marker='o', linestyle='dashed')
    ax1.plot(COL_INP_LSC,y2_ci,'ro')
    plt.title("CorrFctr_2 = Polynomial 3rd")
    #r2_score function is used to calculate the R^2 value of the 3rd Degree Polynomial Curve Fit
    print('R^2_1: ', r2_score(COL_INP_BKR,y2_ci))


    c3_ci,cov3_ci = curve_fit(CorrFctr_3,COL_INP_LSC,COL_INP_BKR,g3,sigma=None,absolute_sigma=False,check_finite=True, method='lm',
    
    #For Loop that converts LSC Shear Stress values into BKR values using exponential function
    y3_ci= np.empty(n_ci)
    for i in range(len(COL_INP_LSC)):
```

Figure 79: Python Code Snippet for the conversion of low sample container into beaker equivalent values; Part 2 of 3

```
        y3_ci[i]=CorrFctr_3(COL_INP_LSC[i],c3_ci[0],c3_ci[1],c3_ci[2])

    
    figci_3, ax1 = plt.subplots()
    ax1.plot(COL_INP_LSC, COL_INP_BKR, color='green', marker='+', linestyle='dashed')
    ax1.plot(COL_INP_LSC,y3_ci,'ro')
    plt.title("CorrFctr_3 = Exponential")
    #r2_score function is used to calculate the R^2 value of the Exponential Function Curve Fit
    print('R^2_1: ', r2_score(COL_INP_BKR,y3_ci))

    c4_ci,cov4_ci = curve_fit(CorrFctr_4,COL_INP_LSC,COL_INP_BKR,g4,sigma=None,absolute_sigma=False,check_finite=True, method='lm',
    
    #For Loop that converts LSC Shear Stress values into BKR values using logarithmic function
    y4_ci= np.empty(n_ci)
    for i in range(len(COL_INP_LSC)):
        y4_ci[i]=CorrFctr_4(COL_INP_LSC[i],c4_ci[0],c4_ci[1],c4_ci[2],c4_ci[3])

    figci_4, ax1 = plt.subplots()
    ax1.plot(COL_INP_LSC, COL_INP_BKR,color='green', marker='.', linestyle='dashed')
    ax1.plot(COL_INP_LSC,y4_ci,'ro')
    plt.title("CorrFctr_4 = Logarithmic")
    #r2_score function is used to calculate the R^2 value of the logarithmic function Curve Fit
    print('R^2_1: ', r2_score(COL_INP_BKR,y4_ci))

    return c1_ci, cov1_ci, y1_ci, c2_ci, cov2_ci, y2_ci, c3_ci, cov3_ci, y3_ci, c4_ci, cov4_ci, y4_ci;
```

Figure 80: Python Code Snippet for the conversion of low sample container into beaker equivalent values; Part 3 of 3

11.3.4 Viscometer Procedure

1. Depending on the temperature at which viscosity will be measured, prepare the thermostatic bath (according to the thermostatic bath manual) using deionized water or silicone oil. *Refer to Note 1

2. Place the 14 mm wide container with the sample into the thermal jacket and use the end cap to seal the bottom of the container.

3. Place manufactured samples into the 14 mm wide container. * Refer to Note 2. Alternatively, place the manufactured samples into a 500 mL beaker (with an inner radius of 83 mm or greater).

4. Based on the approximate viscosity and using the viscosity tables (in the appendix of the viscometer manual [136]), select the appropriate spindle.

5. Attach the spindle to the viscometer. If the LCP spindle is to be used, use the spindle hook to hook the spindle and then attach the other end of the spindle hook to the viscometer, as depicted in Figure 81, Figure 82 and Figure 83.

6. If using the thermal jacket and the small sample container: secure the thermal jacket holding the sample container to the viscometer. The spindle should sit fully submerged, in the fluid post securing the thermal jacket. (Refer to viscometer manual for details and figures)

   If using the thermostatic bath, use the thermostatic bath controls to reach the desired temperature prior to starting the viscometer (Refer to thermostatic bath manual).

   Post equilibrium of desired temperature, turn on the viscometer, via flicking the power input switch, located on the back of the viscometer, as depicted in Figure 84.

   Remove any spindles attached to the viscometer and allow the viscometer to perform a self-test, as depicted in Figure 85.

Set the desired sampling time via navigating to "Options" using the arrow buttons and then selecting the "Output" command, as depicted in Figure 86 and Figure 87.

Figure 81: Depiction of the spindle hook that is used to attach the LCP spindle to the viscometer.

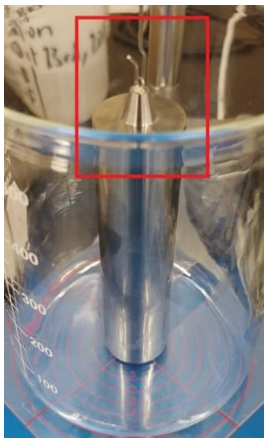

Figure 82: Depiction of LCP spindle hooked onto the LCP spindle hook.

Figure 83: Depiction of the spindle hook threaded onto the viscometer counterclockwise.

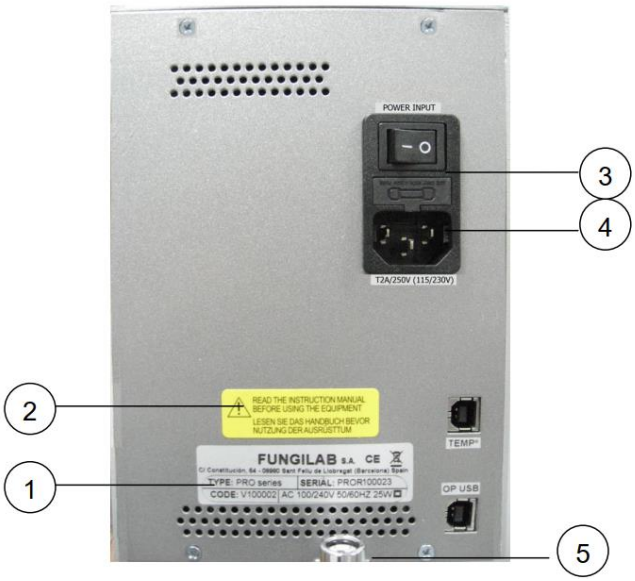

Figure 84: Viscometer on/off switch; located on the reverse plating of the viscometer.

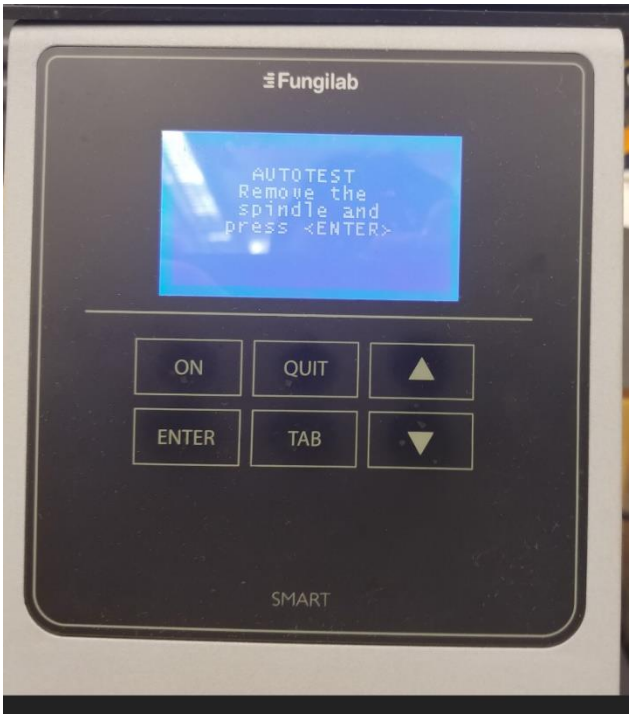

Figure 85: Auto Test Prompt, Post turning on the viscometer.

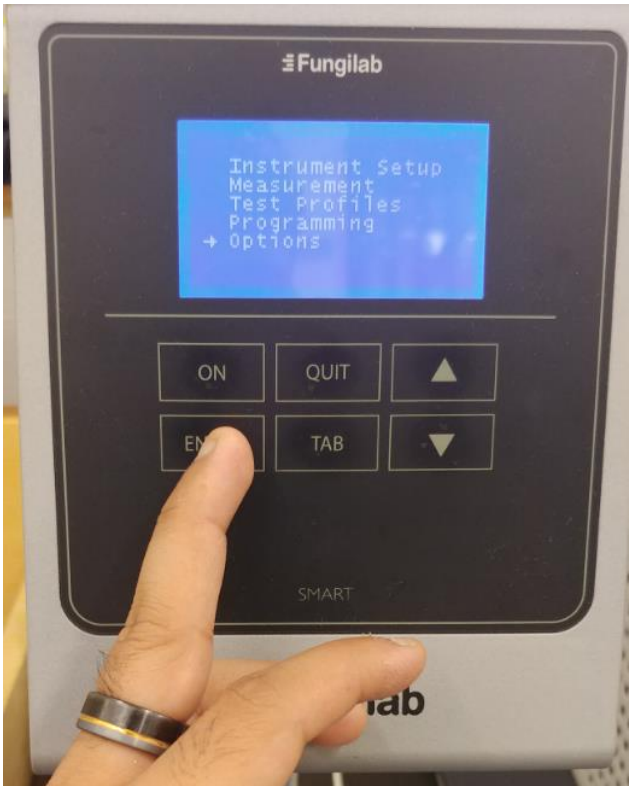

Figure 86: Depiction of the main menu window of the viscometer

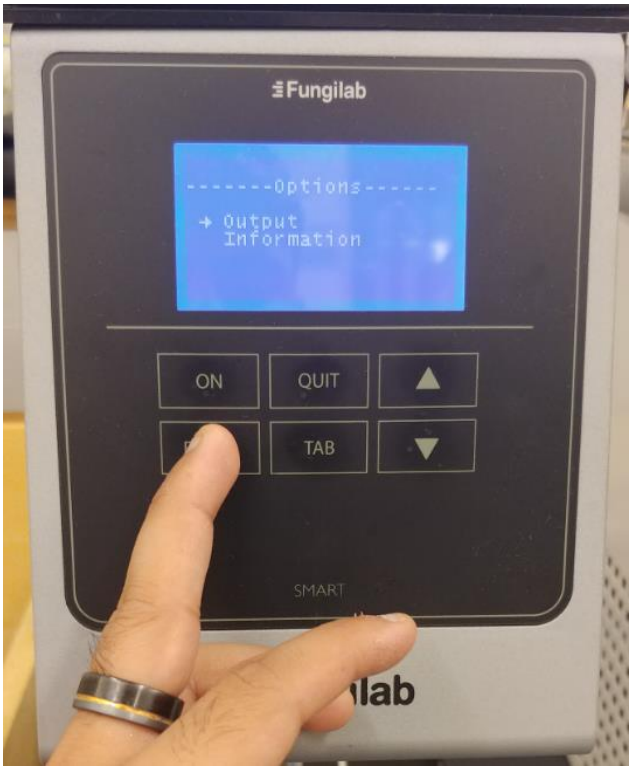

Figure 87: Depiction of the "Options" window of the viscometer

7. The Enter and Arrow buttons are used to then navigate between the Status, Initialization, End, and Increment commands. Ensure the "Status" command is set to ON by navigating to it, pressing the Enter button and then the Tab button to toggle the setting from OFF to ON. This command prompts the viscometer to store data to the internal memory for retrieval using the viscometer software on the computer via USB cable.

8. For sampling of ten minutes with 10 second increments (as indicated in Figure 88), navigate to the "End" command, use the Enter button and then the tab button to navigate to the option that allows for input of minutes, and use the arrow buttons to toggle between digits 0-9; set the "End" command to ten minutes. Next navigate to the Increment command, indicated by "Inc" in the UI using the tab button. Use the enter button and then the arrow buttons to adjust the increments to 10 seconds.

9. After inputting the sampling time, use the QUIT button to navigate back to the main menu and enter the "measurement" window, as depicted in Figure 89.

10. Use the TAB and ENTER buttons to input the type of spindle being used, as well as the density of the fluid for being measured, using the viscometer controls. Use a usb cable to connect the viscometer to the data logging computer.

11. Ensure the viscometer is level. Place a centering gauge (as depicted in Figure 90) onto a laboratory scissor jack and use the centering gauge to centre the beaker relative to the spindle. Once centered, start the sampling using the viscometer by pressing the ON button. The equipment can take up to a minute to produce an accurate result as it requires time for the % EOS to stabilize; however, it typically stabilizes in 30 s.

Figure 88: Depiction of the "Output" window of the viscometer

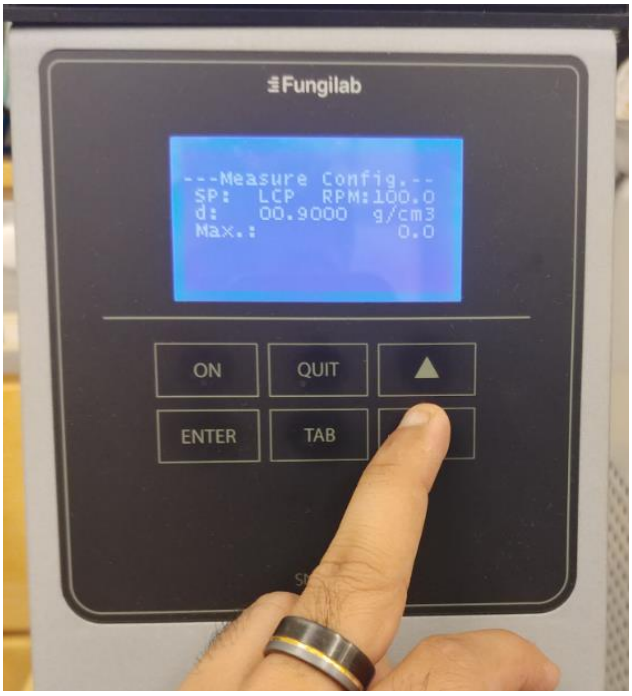

Figure 89: Depiction of the "measurement" window of the viscometer

Figure 90: Centering Gauge used to center the beaker holding the liquid sample relative to the spindle

12. Collect data by plugging in the viscometer to a computer and use the Fungilab viscometer software to extract the data.

Note 1: If temperature control is not necessary then ignore this step.

Note 2: Because the small sample container has a much smaller diameter in comparison to containers greater than 83 mm, (as per section 9 of the viscometer manual) a correction factor to account for wall effects is required.

11.4 Appendix: Nomenclature

11.4.1 Nomenclature – Generic

w/w%	Concentration: weight per weight
w/v%	Concentration: weight per volume
min; mins	minute; minutes
hr; hrs	hour; hours
gram/ grams	g
mL	millilitre; millilitres

11.4.2 Nomenclature – TGA

Symbol	Definition	Units
α	Fraction of A decomposed @ time t	$\frac{Mass_{@\ Time\ T}}{Original\ Mass}$
k	Reaction rate constant	$\frac{1}{s}$
k_0	Frequency Factor	
β	Linear Heating Rate	$\frac{kelvin}{min}$
E_a	Activation Energy	$kJmol^{-1}$
R	Gas Constant	8.314E-3 $Jmol^{-1}K^{-1}$
T	Temperature	Kelvin
x	Amount of Water Evaporated;	$1-\frac{Mass_{@\ Time\ T}}{Original\ Mass}$
Υ	Initial state of dehydration	Unitless
n	Order of the reaction	Unitless

11.4.3 Nomenclature – Viscometer

Symbol	Definition	Units
μ	Dynamic viscosity	$\frac{Na \cdot s}{m^2} = Pa \cdot s = mPa \cdot s = cP$
ρ	Density	$\frac{kg}{m^3}$
τ	Shear Stress	$\frac{g}{cm \cdot s^2}$
γ	Shear Rate	$\frac{1}{s}$
x	Radial location @ which shear rate is being calculated	cm
ω	Rotational speed	$\frac{rad}{s}$
ω_f	Frequency of the sinusoidal stress applied by DMA equipment [155]	Hertz (Hz)
L	Effective Spindle Length	cm
T	Torque	$\frac{g \cdot cm}{s^2} \cdot cm$
v	Volume	cm^3
R_c	Inner radius of the outer cylinder	cm
R_b	Radius of the rotating shaft	cm

11.4.4 Nomenclature – Grunberg-Nissan and Tamura-Kurata Correlations

Symbol	Definition	Units
n_m	Mixture Viscosity	cP
$x_1; x_2$	Mole fraction of Component 1; Component 2	Unitless; $\frac{n_{solute}}{n_{solvent}}$
$\varphi_1;\ \varphi_2$	Volume fraction of Component 1; Component 2	w/v%
d	Interaction coefficient; solution composition independent	Unitless
η_{12}	Interaction coefficient; solution composition dependent	Unitless

11.4.5 Nomenclature – Multi Parametric Model

Symbol	Definition	Units	Value
η	Apparent Viscosity	cP	N/A
A_o	Pre-Exponential Factor	Unitless	N/A
$\dot{\gamma}$	Shear Rate	s^{-1}	122.3
n	Flow Behaviour Index	Unitless	N/A
B	Concentration Factor	Unitless	N/A
C	Constituent Concentration	$\frac{g}{100g}; \frac{w}{w}\%$	N/A
E_a	Activation Energy	$\frac{kJ}{mol}$	N/A
R	Universal Gas Constant	$\frac{kJ}{mol * K}$	0.0083
T	Temperature	$°K$	273.15